Ultrafast Laser Spectroscopy of Novel Fluorescent Nanocrystals

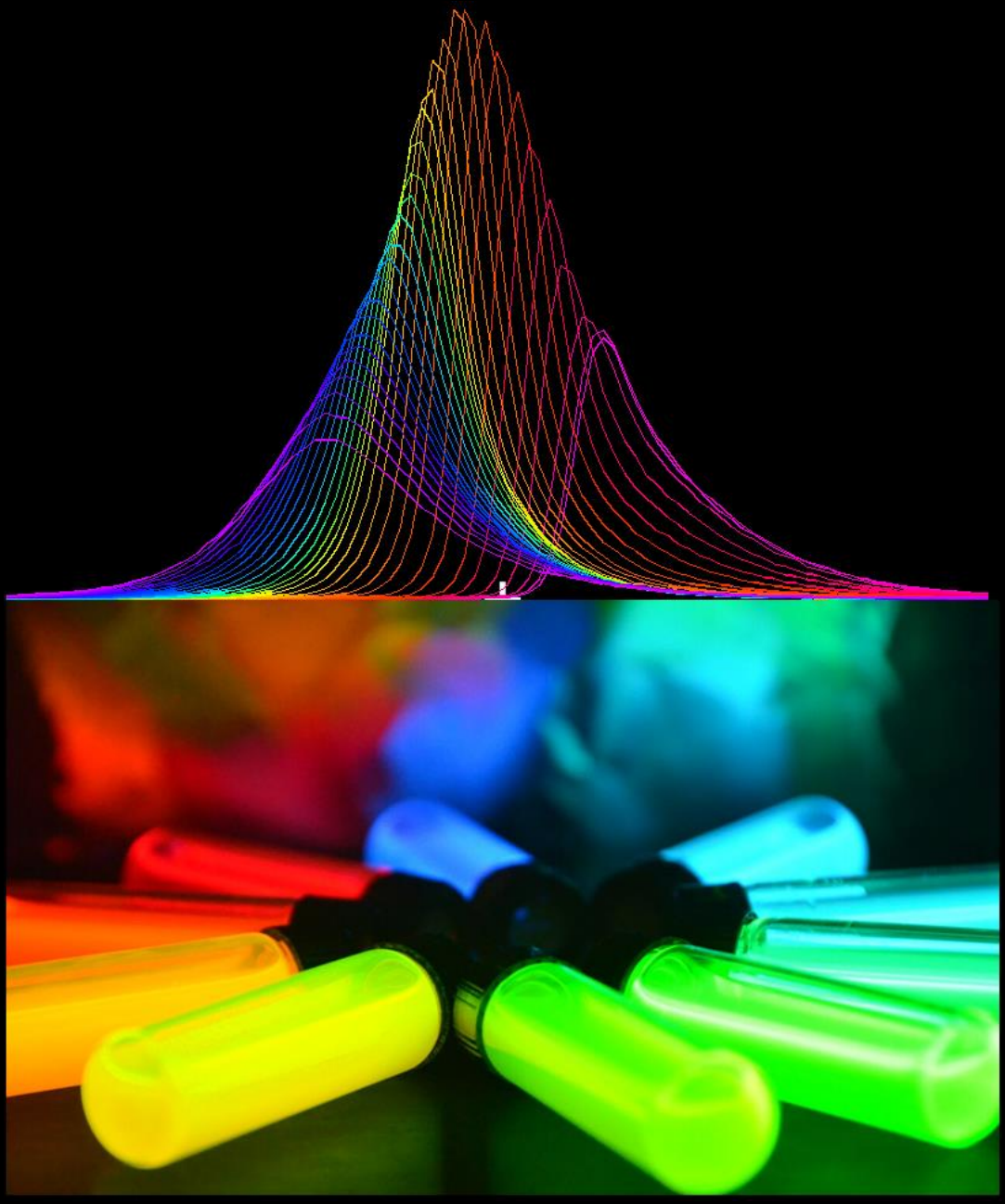

Palvasha Ijaz

ISTITUTO ITALIANO
DI TECNOLOGIA

Università degli Studi di Genova

Istituto Italiano di Tecnologia

Sciences and Technologies of Chemistry and Materials

Doctoral Curriculum: Nanochemistry

Cycle: XXXI

Ultrafast laser spectroscopy of novel fluorescent nanocrystals

Doctoral dissertation presented by

Palvasha Ijaz

Advisors:

Prof. Liberato Manna (Istituto Italiano di Tecnologia)

Prof. Maurizio Canepa (Università degli Studi di Genova)

Dedicated to my son Muhammad Ahmad Imran who passed away during this journey,

Acknowledgement:

First of all, I am deeply grateful to ALLAH S.W.T. for his countless blessings.

I would like to extend my sincere gratitude to Prof. Liberato Manna and Dr. Iwan Moreels for giving me the opportunity to work in a multidisciplinary environment of Nanochemistry department. I deeply admire their tremendous support in my educational and personal affairs during this complex journey.

I am thankful to my farmer scientific advisor Dr. Iwan Moreels for helping me to build my understanding in the field ultra-fast laser spectroscopy. I am thankful to my current scientific advisors Prof. Liberato Manna from iit and Prof. Maurizio Canepa from university of Genova for their continued support and encouragement to complete this journey. I admired the way they trusted me and gave me freedom to explore on my own. I am sincerely thankful to Dr. Joel Q. Grim and Dr. Ilaria Angeloni for training on spectroscopy related equipments. I would like to thank Prof. Roman Krahne and Dr. Beatriz Martín-García all other group members for their productive discussions and help on various projects.

I would like to thank Dr. Guillaume H.V. Bertrand for the synthesis of CdSe/CdS/CdTe core/barrier/crown NCs and Dr. Muhammad Imran for lead halide perovskite NCs. I would like to thank all the technician of ultra-fast laser spectroscopy lab for always being available and supportive.

I am thankful to Prof. Renata Riva and Iulia Manolache Orlatan for their support in all administrative matters.

I would like to offer my sincere thanks to the referees and examination committee for their efforts and time.

I will always be grateful to my husband Dr. Muhammad Imran for his love, care and continuous support to complete this journey. I am thankful to my family especially parents Saeeda bano and Muhammad Ijaz Khan for their endless love and support.

Last but not the least, special thanks to my daughter Minal Fatima and my son Muhammad Musa Imran for tremendous compromise throughout this journey.

Palvasha Ijaz

Summary:

Optical properties of colloidal semiconductor nanocrystals (NCs) have been widely investigated using optical spectroscopy techniques since their birth. In particular, low-temperature spectroscopy minimizes the additional complexity induced by thermal effects, and therefore has been extensively used to investigate the temperature dependent excitonic behavior of various semiconductor materials. It has been well established that the composition, structure and the nature of the NCs surface strongly influence their optical properties. Present PhD dissertation focuses on two main generations of semiconductor colloidal NCs, i.e. 2D metal chalcogenide nanoplatelets (NPLs) and lead halide perovskite NCs. The former generation of material demonstrate remarkable optoelectronic properties, with a narrow and homogeneously broadened emission linewidth (at room temperature), fast exciton recombination and high fluorescence quantum efficiency. These advantageous properties can be further tuned in heterostructures by coating them with another semiconductor materials for instance CdSe/CdS/CdTe core/crown/barrier NPLs. Due to the staggered band offset between CdSe and CdTe, we observed emission from an indirect transition around 650 nm. As CdS forms a barrier for hole relaxation between crown and core regions, the CdSe/CdS/CdTe yielded an additional emission peak from the CdSe core, in contrast with CdSe/CdTe core/crown nanoplatelets without a barrier. The resulting dual emission was investigated as a function of temperature. The different nature of both emission peaks (direct in CdSe vs. indirect across the CdSe/CdTe interface) yielded a spectrally and temporally stable indirect transition as a function of temperature, while the emission rate of the CdSe emission increased at lower temperatures, and the spectral position shifted to shorter wavelengths. The second generation of material studied here i.e “lead halide perovskite” NCs is one of the most investigated semiconductor material in the last decade due to their ease of preparation, broadly

tunable band gap, near unity fluorescence quantum efficiency and excellent color purity. We carried out a comprehensive study of size, composition and surface functionalization dependent optical properties of lead halide perovskite NCs. Contrary to most of the previous findings, we observe a single, narrow emission peak at low temperature for NCs with various sizes, compositions and surface coatings. Temperature-dependent photoluminescence (PL) and PL-lifetime data for different compositions ($APbBr_3$, A=Cs, MA, FA) reveal that MA-based NCs were the most sensitive to temperature variations with least preservation of PL, featuring the highest thermal broadening of PL and longest lifetimes, whereas FA based NCs were the most resilient. Furthermore, a comparison of the photophysical properties of NCs having different surface coatings shows that their optical properties are strongly influenced by surface chemistry, with quaternary bromide capped NCs being the most stable samples at elevated temperature, as they retained the highest PL intensity. Considering all these results together, we provide unequivocal evidence that lead halide perovskite NCs exhibit no inhomogeneity in their PL and additionally their optical properties are strongly surface functionalization dependent. These fundamental insight into the optical properties of both generation of materials would be key for the development of future photonic devices.

Table of content

List of Figures

Chapter 1.

Chapter 2.

Chapter 3.

Chapter 1

1.1. Semiconductors materials

Advancement in the development of semiconductors materials and their successful integration in wide range of applications such as solar cells, LEDs, lasers and electronics significantly improves our daily lives. Semiconductors are at the core of every electronics device in various forms including diodes, transistors, LED and processor etc. These materials revolutionized the operational capabilities of many devices including mobile phones, computers, credit cards and several other devices of our daily use.[1, 2] Nevertheless the demand of more powerful but yet smaller devices motivated the scientific community to find more efficient materials which eventually lead to several discoveries during last three decades. One out of several exciting discoveries was the breakthrough of colloidal nanocrystals (NCs) or often referred to as quantum dots (QDs) which is deeply rooted on scaling laws. Briefly, varying the size of NCs allows their optical properties to be conveniently tuned across entire visible or infrared spectrum. Furthermore, these NCs can be handled in the form of stable colloidal dispersion in various solvents which allows them to be deposited using simple deposition techniques like inkjet printing or spray painting for device fabrication at room temperature. Such semiconductors NCs have enormous potential for converting light into electricity and vice versa, makes them excellent materials for use in display related technologies and photovoltaic devices. Additionally, semiconductors NCs also exhibit temperature/radiation dependent optical properties which allows them to be used in heat sensors or radiation detectors.

1.2. A brief history of semiconductor Nanocrystals

The realization of size dependent properties of materials can be traced back to the middle ages, however first scientific study was reported in 1857 by Michael Faraday.[3] He was investigating the relationship between various thickness of gold (other meatls) and light but accidently observed different coloured solutions while attempting to mount gold leafs onto microscope slide. Based on these experiments he concluded that “known phenomena appeared to indicate that a mere variation in the size of its particles gave rise to a variety of resultant colours” and furthermore the absorption, reflection and refraction properties of the corresponding materials would change significantly by the substitution of different sized particles. Another major breakthrough came nearly a century later when electronic structure dependence on the size of NCs was demonstrated by embedding nanometre size silver iodide and copper chloride into sodium chloride matrices.[3-6] Thereafter, the field kept evolving through theoretical and experiential studies (synthesis of colloidal PbS and CdSe

QDs) along with technological advancement of characterization techniques (especially the transmission electron microscope for morphological -analysis) until 1992.[7-12] In 1993, a major invention in the field of NCs was achieved by Bawendi's group.[13] They developed a synthesis procedure which enable them to produce nearly monodisperse colloidal CdSe NCs and demonstrated the quantum-size effects in the optical spectra of these NCs (figure 1.1 a to c).

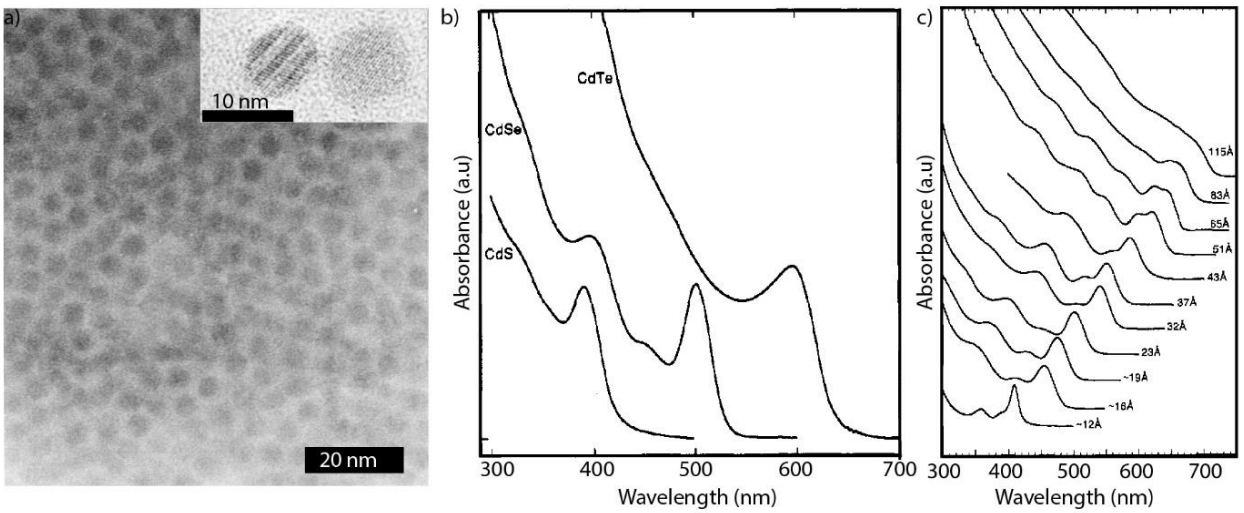

Figure 1.1. TEM image of a near monolayer of 5.1 nm CdSe NCs showing short-range hexagonal close packing and inset showing high resolution TEM image of CdSe NCs (a), Room temperature optical absorption spectra of -2 to 3nm CdS, CdSe, and CdTe NCs (b) Room temperature optical absorption spectra of CdSe NCs with size ranging from 1.2 to 11.5 nm dispersed in hexane.

Afterwards the field spread for wide range of materials with the precision to tune their size, shape, composition and even complex (binary, ternary or quaternary) NCs consisting of multiple semiconductor domains with tuneable optical properties.[14-17] Beside the development on syntheses frontier, the field of nanoscience has been moved from fundamental research towards applications, with NCs being used in a wide range of applications such as LEDs, lasers, solar cells, bio imaging and cancer treatments.

1.3. Optical properties of semiconductors

Materials are classified on the bases of energy band such as insulator, conductor and semiconductor. The properties of a semiconductor lie somewhere between those of a conductor (like metals) and those of an insulator (glass, wood, most plastics, ceramics). Similarly the electric conductivity of a

semiconductor material lies somewhere in-between that of conductors and insulators, therefore it is referred to as “semi-conductor”. Since these materials are composed of multiple atoms, these atoms combined into a molecule as well the wave functions of individual atomic orbitals (AOs) hybridized. The shape of the orbitals in the newly formed molecule can be determined using the “linear combination of atomic orbitals” (LCAO) approach, which combines the wave functions of individual AOs, forming so-called molecular orbitals. The accumulation of these molecular orbitals leads to the formation of a “band”. Valence band (VB) is formed by the coupling of highest occupied molecular orbitals (HOMO) whereas the conduction band (CB) is formed by the coupling of lowest unoccupied molecular orbitals (LUMO) and the separation between valence band and conduction band is known as band gap (Eg). In bulk semiconductor solids atoms are packed tightly, leading to the stronger interaction of outer AOs and form broad energy bands. The electron wave function and energy are not influenced by the edges of the solid, and the density of states (DOS) is quasi-continuous, following the square-root of energy. However the electronic structure changes drastically when the dimensions of the crystal are reduced i.e there are more discrete energy levels at the band edges upon decreasing the size from bulk to NC (see figure 1.2). In other words, increasing the size from a cluster that is composed of few tens of atoms to a small NC (few hundred atoms),

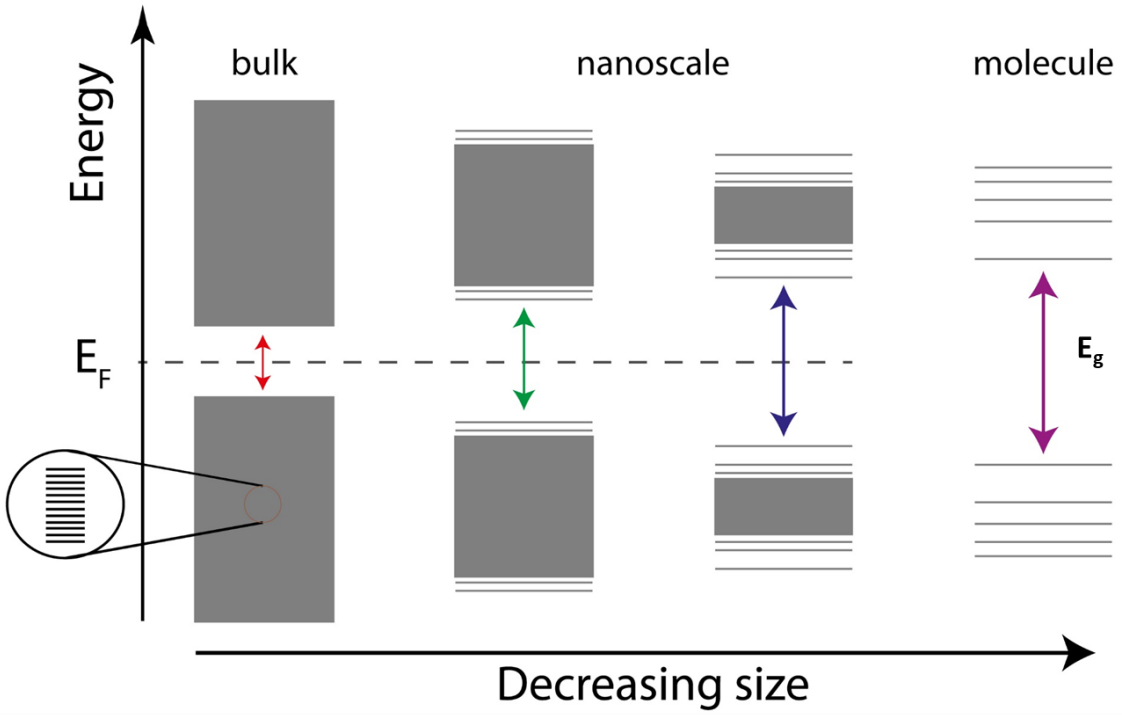

Figure 1.2. Comparison of bulk, NCs and molecules, indicating the size dependent bandgap of NCs and the formation of discrete states near the band edge.

more and more AO combined and the resulting multitude of MOs lead to the formation of a quasi-continuous bands (figure 1.2, from the rightmost to the left). The increase in the size of NCs not only decrease the energy of separation between individual MOs but also decrease the separation between the VB and CB (bandgap decreases).

1.4. Dimensionality dependent optical properties of semiconductors

Limiting the dimensionality of semiconductor at nanoscale in 1D, 2D or 3D significantly influence the carrier motion. A more physical way to look at how the carrier motion is influenced in one or more dimensions, we can use particle in a box model. By solving the Schrödinger equation in one dimension under the assumption of infinitely high potential at the edges, we obtain the following equation,

$$E_n = \frac{\hbar^2 \pi^2}{2ma^2} n^2 \qquad (1.1)$$

Where a is the size of the box, m is the mass of the particle and n=1, 2, 3. Similarly, by solving the 3D Schrödinger equation in a system with reduced dimensionality it is possible to compute its DOS. When the electron is confined in one dimension (2D material), the DOS becomes a quasi-continuous step function enveloped by the original square root energy dependence.[18]

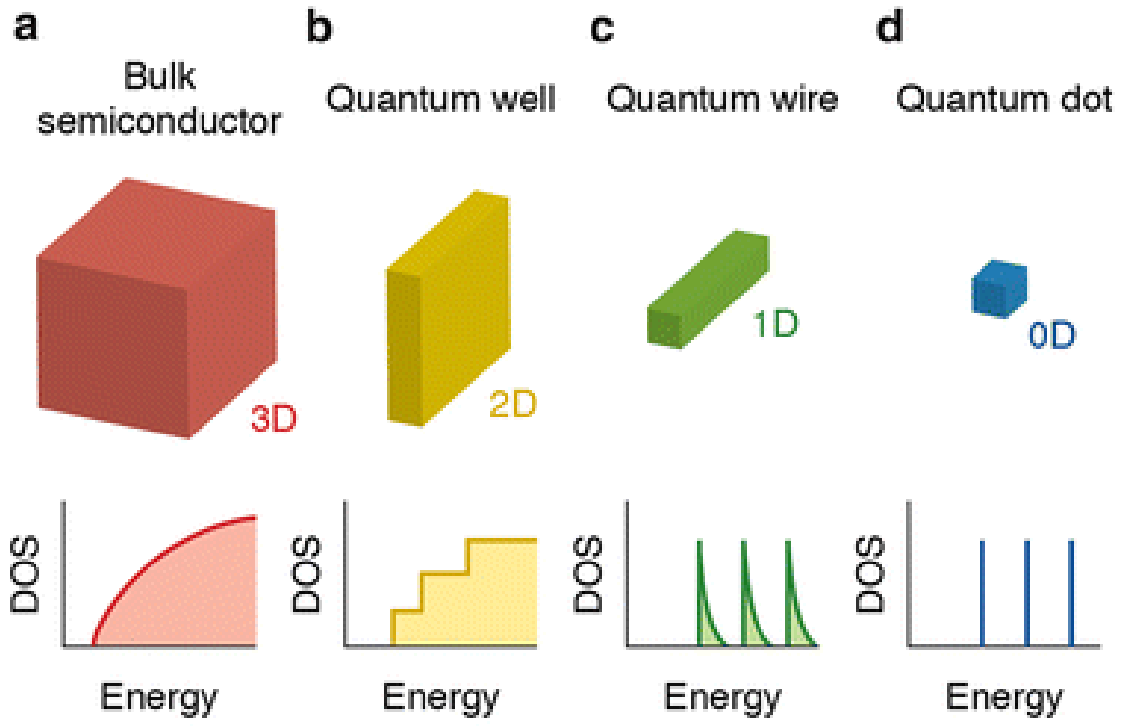

Figure 1.3. Effect of dimensional confinement on the DOS: (a) bulk (3D) with continues DOS, (b) quantum wells with a step-like DOS, (c) quantum wire (1D) with a saw-tooth dependent DOS and (d) Quantum dots (0D) with only discrete sates available.

When two spatial dimensions are restricted (1D material), the DOS assumes a saw-tooh profile, which collapses into a series of discrete energy levels in the case the motion of the carrier is restricted in all the three dimensions (0D system). In this case, the DOS resembles the one of electrons in an atom, leading to the widespread definition of quantum dots (QDs) as artificial atoms. A scheme of the DOS in the different cases can be found in Figure 1.3. Notably, equation (1.1) shows that the energy for the first level is inversely proportional to the size of the box a (dimension of the box). This implies that the energy gap in a semiconductor NC is higher than the bulk counterpart and increases significantly by reducing the dimension, also known as quantum confinement effect in semiconductor NCs. Due to the quantum confinement effect, the optoelectronic properties of the semiconductor NCs become strongly size and shape dependent and further making it possible to tune the photoluminescence by precisely varying the size of NCs. These features have turned colloidal semiconductor NCs as a versatile photonic source with emission broadly tunable across the entire visible spectrum and makes them highly desirable for display related technologies, see figure 1.4.

1.5. Scope of the Thesis

The present PhD thesis can be subdivided into two main sections, as it focuses on two main classes of colloidal semiconductor NCs, i.e. metal chalcogenide heterostructure and lead halide perovskite NCs. The former generation of material demonstrate remarkable optoelectronic properties, with a narrow and homogeneously broadened emission linewidth (at room temperature), fast exciton recombination and high fluorescence quantum efficiency. These properties can be further tuned by coating them with multiple semiconductor materials for instance CdSe/CdS/CdTe core/crown/barrier. The present thesis gives a contribution to identify the optical behavior of this CBC NCs at room and low temperature as function of their barrier size. The second generation of material studied here i.e “lead halide perovskite” NCs is one of the most investigated semiconductor material in the last years due to their ease of preparation, broadly tunable band gap, near unity fluorescence quantum efficiency and excellent color purity. We carried out a comprehensive study on the temperature dependent photoluminescence (PL) and PL decay dynamics of LHP NCs varying their A site cation, the surface ligands, and the NC sizes.

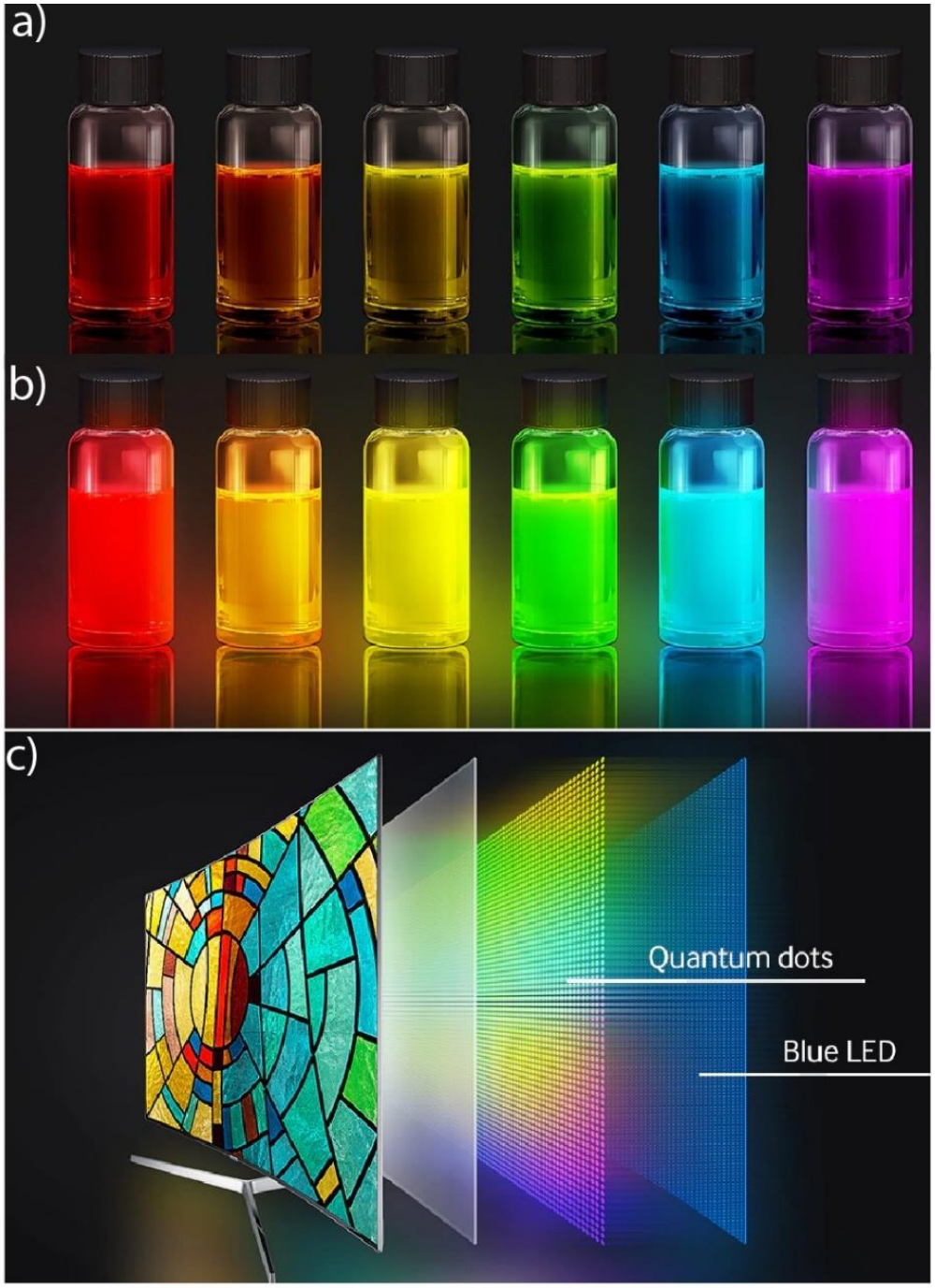

Figure 1.4. Colloidal dispersions of semiconductor NCs with different sizes resulting in a range of different colors under normal light (a) and under UV lamp (b), an example of their use in Samsung Ultra High Definition TVs (c).[4]

1.6. Optical properties of Metal Chalcogenide NCs

Advances in colloidal synthesis approaches provided an additional degree of freedom to tune the optical properties of NCs through compositional engineering. For instance, using seeded growth method it is possible to grow several semiconductor materials in the form of core/shell, Janus type NC or gradient alloys. The resulting hetero-NC are composed of two or more than two

semiconductors with different band gaps. Depending on the way the conduction and valence bands of the core and shell materials are aligned, we can obtain three band profiles, shown in Figure 1.5. In a Type I alignment, the band gap of the core is fully contained within the gap of the shell material. In this case, both the electron and hole wave functions reside in the same spatial region. CdSe/ZnS core/shell hNCs, among others, belong to this category. However, for a significantly different electron affinity for core and shell materials, these bands can shift, leading to a staggered band alignment (Type II), as in ZnSe/CdS, CdTe/CdSe, or CdSe/ZnTe NCs.[19-22] In this case, electrons and holes reside in different parts of the NC heterostructure, creating a spatially indirect exciton which is characterized by recombination lifetimes longer with respect to the direct exciton of Type I materials. An intermediate situation can happen, in which the conduction band has nearly no offset between the two materials. In this case the hole is confined by the potential well, while the electron is delocalized. Such a band profile is defined quasi-type II.[23]

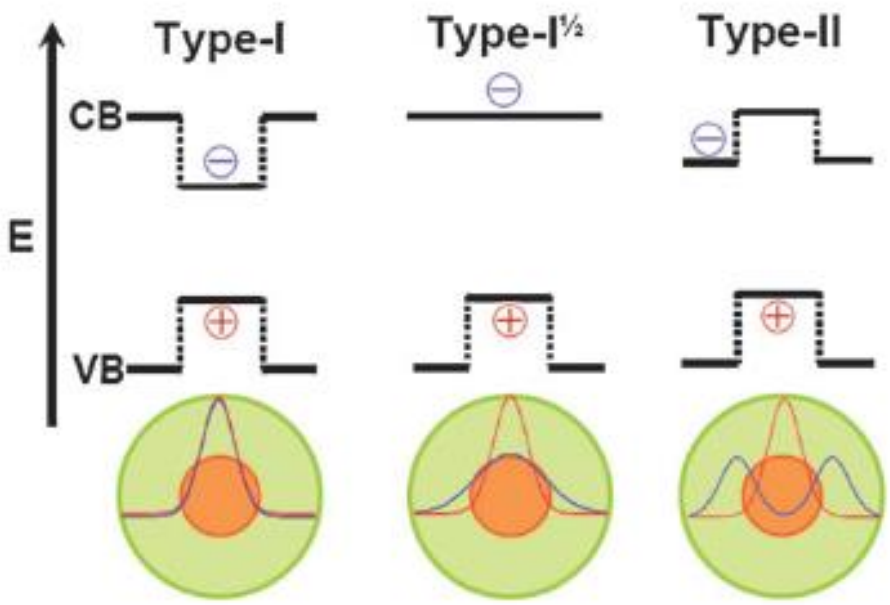

Figure 1.5. Schematic representation of the three limiting charge carrier localization regimes in core/shell semiconductor HNCs. The conduction and valence band edges (i.e., the LUMO and HOMO energy levels) are indicated by CB and VB, respectively. The plus and minus signs represent the charge carriers (hole and electron, respectively). The electron and hole ground-state wave functions are schematically depicted in the lower panel.[23]

Nano-platelets heterostructure are particularly appealing as they combine the strong anisotropic confinement of 2D materials and the wide range of properties of semiconductor junction. In the past few years nano-platelets (NPLs) took a prominent place in this field and demonstrate remarkable opto-electronics properties. Synthesis of such NPLs recently took a step forward giving access to different cadmium chalcogenide zinc-blende materials. In particular CdSe NPLs are the center of many studies concerning the control of their synthesis, relationship between shape and exciton dynamics and auto assembly properties. This properties can be combined with all the material design existing for spheres particle, especially binary architecture. Indeed spherical core-shell structure can be transpose in 2D affording brick in brick (core-shell) structure or the more peculiar core-crown architecture. In this last family a secondary materials is grown on the facets perpendicular to the core NPL main plane, extending the 2D structure. The core and crown material can be chosen to design band alignment of interest such as type I or type II interface. This offer unique property such as antenna effect and exciton concentration of the CdSe/CdS Type I core crown sytem, or a long lifetime type II transition in CdSe/CdTe core-crown NPLs.[24-33] This last example is very interesting as it only present type II emission, even though intrinsic CdSe and CdTe emission are much faster. Exciton wave function can be further manipulate by inserting a barrier in between the type II junction. Such ternary architecture are also known to favor and stabilized charge separated excited state, leading to interesting development in the field of up-conversion. Shape is a very important parameter in semiconductor nanostructures because it can strongly affect the opto-electronic properties. 2D semiconductor nanoplatelets (NPLs) are also known as quantum wells (QWs). These NPLs are atomically flat quasi two-dimensional (2D) quantum-confined nanocrystals and typically composed of wide bandgap II-VI materials. High quality single crystal nanoplatelets samples are synthesized by colloidal chemistry. In CdSe/CdS/CdTe heterostructures, the core and crown material is chosen such that the CdS forms a tunneling barrier for holes in the valence band, while electrons can relax from the CdTe crown to the CdSe core via the cascaded band offset in the conduction band. This yield simultaneous type I and type II emission. The uniform 1D quantum confinement in the core crown NPLs leads to sharp peaks in the absorption and photoluminescence spectra of the NPLs at the room temperature. This thesis provides detailed insight into optical properties of a ternary architecture consisting of a core of CdSe surrounded by a barrier of CdS and crowned by CdTe, henceforth referred to as Core/Barrier/Crown (CBC). The optical behavior of this CBC nanocrystal were investigate at room and low temperature in order to identify dependence of optical property according to barrier size.

1.7. Optical properties of lead halide perovskite NCs

Optical properties of colloidal semiconductor nanocrystals have been widely investigated since three decades. It has been well established that the composition as well as nature of the nanocrystal surface have strong impact on their optical properties.[34-37] Recently, lead halide perovskite nanocrystals (LHP-NCs) emerged as a promising material in colloidal quantum dot semiconductor family due to their ease of preparation, broadly tunable band gap, high photoluminescence quantum yield (PLQY) and excellent color purity.[38-40] This remarkable set of properties makes them ideal candidates for light emission related technologies such as light emitting diodes, lasers and single photon emitters.[41-43] Low-temperature spectroscopy minimizes the additional complexity induced by thermal effects, and therefore has been widely used to investigate the temperature dependent excitonic behavior of traditional semiconductors and recently of LHP-NCs.[44-47] Significant progress has been made in the syntheses of LHP-NCs, especially with regard to size, shape, composition control, and by tailoring the surface passivation through direct synthesis or post synthesis ligand exchange.[38] The advancements on synthesis of LHP not only paved the way to investigate shape and composition dependent optical properties, but also offer a great opportunity to investigate their surface functionalization dependent optical properties. In the LHP-NCs family, the optical properties of fully inorganic cesium (Cs^+) based perovskites have been studied the most, whereas their methylammonium (MA^+) and formamidinium (FA^+) counterparts are less investigated. For $CsPbX_3$ (X=Cl,Br,I) NCs, there is a lack of consensus about the origin of multiple PL peaks appearing at low temperatures. For instance, Li et al. studied temperature dependent optical properties of $CsPbBr_3$ NCs with different sizes.[46] and found that $CsPbBr_3$ NCs with intermediate size manifest a blue shifted dual emission around 80K while further smaller or bigger NCs show a single blue shifted emission peak at this temperature. Contrary to this, Lee et al. reported dual emission for 11nm size $CsPbBr_3$ NCs for the same range of temperature.[48] Later on Shinde et al. carried out temperature dependent optical spectroscopy of 3 different sizes (5.5, 7.3 and 10.1 nm) of $CsPbBr_3$ NCs.[49] They observed size dependent emission peaks (smaller the size of the NCs leads to larger number of emissions) at 10 K and this was attributed to the degree of quantum confinement in $CsPbBr_3$ NCs.

Figure 1. 6. Luminescent lead halide perovskite NCs: Colloidal dispersion of $CsPbX_3$ NCs under UV lamp prepared by using Benzoyl halide synthesis method.[54]

Similarly Laru et. al. reported that the distortion in the orthorhombic phase of $CsPbBr_3$ NCs at low temperature leads to distinct carrier-phonon coupling which consequently results in multiple emissions.[50] Recently, Drioll et al. investigated the low temperature absorption, PL and lifetimes dynamics of 15nm size $CsPbBr_3$ NCs and observed single narrow red shifted emission at 3K.[51] From the surface chemistry perspective, first generation of LHP NCs were typically prepared by using primary alkyl amine (e.g. RNH_3^+) and alkyl carboxylates as a surfactant and it has been well established that both ligands constitute the final ligand shell composition (henceforth referred to as mixed ligands capped NCs). Substantial advances in colloidal syntheses over past few years provided the opportunity to prepare LHPs NCs with diverse surface coatings leading to unique photophysical properties.[52, 53] However, optical spectroscopy based investigations were mainly limited to the first generation of NCs (mixed ligands capped). In particular, the temperature dependent optical spectroscopy of trap free (near unity PLQY emitter) would be appealing to understand their excitonic properties. Therefore, a comprehensive investigation is highly needed to elucidate the influence of composition (monovalent cation), disparity of size related multiple emissions, and more importantly the impact of surface functionalization on the optical properties of LHP-NCs.

1.8. References

1. Semiconductors Shaping Society. The Electrochemical Society, https://www.electrochem.org/semiconductors-shaping-society.
2. Enabling the Hyperconnected Age: The Role of Semiconductors. Oxfor Economics, https://www.oxfordeconomics.com/recent-releases/enabling-the-hyperconnected-age-the-role-of-semiconductors.
3. Faraday, M., Experimental Relations of Gold (and Other Metals) to Light. Philos. Trans. Royal Soc. 1857, 147, 145-181
4. What Do Medieval Stained Glass and Suhd Tv's Quantum Dot Technology Have in Common? https://www.samsung.com/global/tv/blog/stained-glass-and-quantum-dot-technology/ 2016.
5. Odom, T. W., Printable Stained Glass. Nat. Nanotechnol. 2012, 7, 550.
6. Freestone, I., et al., The Lycurgus Cup — a Roman Nanotechnology. Gold Bull. 2007, 40, 270-277.
7. Evans, B. L.; Young, P. A., Exciton Spectra in Thin Crystals: The Diamagnetic Effect. Proc. Phys. Soc. 1967, 91, 475.
8. kimov, A. I.; Onushchenko, A. A., Quantum Size Effects in 3-Dimensional Microscopic Semiconductor Crystals. Jetp Lett. 1981, 34, 345-349.
9. Efros, A. L., Interband Absorption of Light in a Semiconductor Sphere. Sov. Phys. Semicond. 1982, 16, 772-775
10. Brus, L., Electronic Wave Functions in Semiconductor Clusters: Experiment and Theory. J. Phys. Chem. 1986, 90, 2555-2560.
11. Brennan, J. G., et al., Bulk and Nanostructure Group II-VI Compounds from Molecular Organometallic Precursors. Chem. Mater. 1990, 2, 403-409.
12. Steigerwald, M. L., et al., Surface Derivatization and Isolation of Semiconductor Cluster Molecules. J. Am. Chem. Soc. 1988, 110, 3046-3050.

13. Murray, C. B., et al., Synthesis and Characterization of Nearly Monodisperse CdE (E = Sulfur, Selenium, Tellurium) Semiconductor Nanocrystallites. J. Am. Chem. Soc. 1993, 115, 8706-8715.

14. Donega, C. d. M., Synthesis and Properties of Colloidal Heteronanocrystals. Chemical Society Reviews 2011, 40, 1512-1546.

15. Burda, C., et al., Chemistry and Properties of Nanocrystals of Different Shapes. Chem. Rev. 2005, 105, 1025-1102.

16. Talapin, D. V., et al., Prospects of Colloidal Nanocrystals for Electronic and Optoelectronic Applications. Chem. Rev. 2010, 110, 389-458.

17. Brus, L. E., Electron–Electron and Electron-Hole Interactions in Small Semiconductor Crystallites: The Size Dependence of the Lowest Excited Electronic State. J. Chem. Phys. 1984, 80, 4403-4409.

18. M. Fox, Quantum Optics: An Introduction, OUP Oxford 2006, ISBN 978-0-19-152425-7.

19. M. A. Hines and P. Guyot-Sionnest, Synthesis and Characterization of Strongly Luminescing ZnS-Capped CdSe Nanocrystals, The Journal of Physical Chemistry 1996, 100 , 468{471, ISSN 0022-3654.

20. A. Nemchinov et al., Synthesis and Characterization of Type II ZnSe/CdS Core/Shell Nanocrystals, The Journal of Physical Chemistry C 2008, 112 , 9301{9307, ISSN 1932-7447.

21. D. Oron, M. Kazes and U. Banin, Multiexcitons in type-II colloidal semiconductor quantum dots, Physical Review B 2007, 75, 035330.

22. S. Kim et al., Type-II Quantum Dots: CdTe/CdSe(Core/Shell) and CdSe/ZnTe(Core/Shell) Heterostructures, Journal of the American Chemical Society 2003, 125 , 11466{11467, ISSN0002-7863.

23. de Mello Donegá C. Synthesis and properties of colloidal heteronanocrystals. Chemical Society Reviews. 2011;40(3):1512-46.

24. B. Guzelturk, Y. Kelestemur, M. Olutas, S. Delikanli and H. V. Demir, ACS Nano, 2014, 8, 6599.

25. Z. Chen, B. Nadal, B. Mahler, H. Aubin and B. Dubertret, Adv. Funct. Mater., 2014, 24, 295–302.

26. S. Ithurria, M. D. Tessier, B. Mahler, R. P. Lobo, B. Dubertret and A. L. Efros, Nat. Mater., 2011, 10, 936.
27. Tessier, Mickaël D., Piernicola Spinicelli, Dorian Dupont, Gilles Patriarche, Sandrine Ithurria, and Benoit Dubertret., 2013 Nano letters 14, 207-213.
28. Pedetti, S., Ithurria, S., Heuclin, H., Patriarche, G., & Dubertret, B. J. Am. Chem. Soc., . (2014) 136(46), 16430-16438.
29. Achtstein, Alexander W., Anatol V. Prudnikau, Maxim V. Ermolenko, Leonid I. Gurinovich, Sergey V. Gaponenko, Ulrike Woggon, Alexander V. Baranov et al. ACS nano 8, no. 8 (2014): 7678-7686.
30. Achtstein, Alexander W., Andrei Schliwa, Anatol Prudnikau, Marya Hardzei, Mikhail V. Artemyev, Christian Thomsen, and Ulrike Woggon. Nano letters 12, no. 6 (2012): 3151-3157.
31. Boles, M. A., Ling, D., Hyeon, T. & Talapin, D. V. The surface science of nanocrystals. Nature materials 15, 141 (2016).
32. Chen, O. et al. Surface-functionalization-dependent optical properties of II–VI semiconductor nanocrystals. Journal of the American Chemical Society 133, 17504-17512 (2011).
33. Talapin, D. V., Lee, J.-S., Kovalenko, M. V. & Shevchenko, E. V. Prospects of colloidal nanocrystals for electronic and optoelectronic applications. Chemical reviews 110, 389-458 (2009).
34. Shamsi, J., Urban, A. S., Imran, M., De Trizio, L. & Manna, L. Metal Halide Perovskite Nanocrystals: Synthesis, Post-Synthesis Modifications, and Their Optical Properties. Chemical reviews 119, 3296-3348 (2019).
35. Protesescu, L. et al. Nanocrystals of cesium lead halide perovskites (CsPbX3, X= Cl, Br, and I): novel optoelectronic materials showing bright emission with wide color gamut. Nano letters 15, 3692-3696 (2015).
36. Schmidt, L. C. et al. Nontemplate synthesis of CH3NH3PbBr3 perovskite nanoparticles. Journal of the American Chemical Society 136, 850-853 (2014).
37. Sutherland, B. R. & Sargent, E. H. Perovskite photonic sources. Nature Photonics 10, 295 (2016).

38. Kovalenko, M. V., Protesescu, L. & Bodnarchuk, M. I. Properties and potential optoelectronic applications of lead halide perovskite nanocrystals. Science 358, 745-750 (2017).

39. Quan, L. N. et al. Perovskites for Next-Generation Optical Sources. Chemical reviews 119, 7444-7477 (2019).

40. Jing, P. et al. Temperature-dependent photoluminescence of CdSe-core CdS/CdZnS/ZnS-multishell quantum dots. The Journal of Physical Chemistry C 113, 13545-13550 (2009).

41. Zhao, Y. et al. High-temperature luminescence quenching of colloidal quantum dots. ACS nano 6, 9058-9067 (2012).

42. Li, J. et al. Temperature-dependent photoluminescence of inorganic perovskite nanocrystal films. Rsc Advances 6, 78311-78316 (2016).

43. Diroll, B. T., Nedelcu, G., Kovalenko, M. V. & Schaller, R. D. High-Temperature Photoluminescence of CsPbX3 (X= Cl, Br, I) Nanocrystals. Advanced Functional Materials 27, 1606750 (2017).

44. Lee, S. M. et al. Temperature-dependent photoluminescence of cesium lead halide perovskite quantum dots: splitting of the photoluminescence peaks of CsPbBr3 and CsPb (Br/I) 3 quantum dots at low temperature. The Journal of Physical Chemistry C 121, 26054-26062 (2017).

45. Shinde, A., Gahlaut, R. & Mahamuni, S. Low-temperature photoluminescence studies of CsPbBr3 quantum dots. The Journal of Physical Chemistry C 121, 14872-14878 (2017).

46. Iaru, C. M., Geuchies, J. J., Koenraad, P. M., Vanmaekelbergh, D. l. & Silov, A. Y. Strong carrier–phonon coupling in lead halide perovskite nanocrystals. ACS nano 11, 11024-11030 (2017).

47. Diroll, B. T., Zhou, H. & Schaller, R. D. Low-Temperature Absorption, Photoluminescence, and Lifetime of CsPbX3 (X= Cl, Br, I) Nanocrystals. Advanced Functional Materials 28, 1800945 (2018).

48. De Roo, J. et al. Highly dynamic ligand binding and light absorption coefficient of cesium lead bromide perovskite nanocrystals. ACS nano 10, 2071-2081 (2016).

49. Smock, S. R., Williams, T. J. & Brutchey, R. L. Quantifying the Thermodynamics of Ligand Binding to CsPbBr3 Quantum Dots. Angewandte Chemie 130, 11885-11889 (2018).

50. Ravi, V. K. et al. Origin of the substitution mechanism for the binding of organic ligands on the surface of CsPbBr3 perovskite nanocubes. The journal of physical chemistry letters 8, 4988-4994 (2017).

51. Pan, A. et al. Insight into the ligand-mediated synthesis of colloidal CsPbBr3 perovskite nanocrystals: the role of organic acid, base, and cesium precursors. ACS nano 10, 7943-7954 (2016).

52. Koscher, B. A., Swabeck, J. K., Bronstein, N. D. & Alivisatos, A. P. Essentially trap-free CsPbBr3 colloidal nanocrystals by postsynthetic thiocyanate surface treatment. Journal of the American Chemical Society 139, 6566-6569 (2017).

53. Wheeler, L. M. et al. Targeted Ligand-Exchange Chemistry on Cesium Lead Halide Perovskite Quantum Dots for High-Efficiency Photovoltaics. Journal of the American Chemical Society 140, 10504-10513 (2018).

54. Imran, Muhammad, et al. "Benzoyl halides as alternative precursors for the colloidal synthesis of lead-based halide perovskite nanocrystals." *Journal of the American Chemical Society* 140.7 2656-2664, (2018).

Chapter 2. Methods and Techniques

All the characterization tool used to investigate the materials including Experimental determination of the optical properties are reported in the thesis are listed here.

2.1. Absorbance

Absorbance spectra of the samples studied in this work were collected with a Varian Cary 300 UV-vis spectrophotometer or a Cary 5000 UV-vis-NIR spectrophotometer, using quartz cuvettes with an optical path length of 1 cm. An absorbance measurement quantifies the attenuation of light while it passes through the material as:

$$A = -\log_{10}T$$

Where T is the transmittance, depend as the ratio between the intensities of incident and transmitted light. However, the only source of light attenuation by a material: also reflection and scattering can reduce the intensity of transmitted light. Reflectance losses are usually corrected for by measuring the transmission of the same cuvette filled with pure solvent, and using this measurement as a baseline for the measurement of the composite material. The contribution of absorption and scattering are instead not separable in the measured attenuation. The absorption and scattering coefficients add up to the extinction coefficient, that is the quantity represented in an absorbance spectrum. In case particles are small compared to the wavelength of light, as for our NCs, scattering can be treated according to Rayleigh's law, and the scattering cross section is proportional to $1/\lambda^4$. For the CdSe/CdS, CdSe/CdS/CdTe and the lead halide perovskite NCs studied in chapters III and the IV, the small dimension of the NCs and their good dispersibility (i.e., lack of aggregates) ensured a negligible scattering, as also demonstrated by the at absorbance spectrum for energies below the band gap. The negligible scattering component allowed us to use absorbance data do quantitatively estimate the intrinsic absorption coefficient.

2.2. Photoluminescence

Photoluminescence (PL) measurements on NC ensembles were performed with an Edinburgh Instruments FLS920 spectrouorometer, using a xenon lamp coupled with a monochromator as excitation source. In a PL measurement, the sample is excited at a fixed wavelength λex, and emission is collected for $\lambda > \lambda ex$.

2.3. Photoluminescence excitation

In a PL excitation (PLE) measurement, a range of excitation wavelengths is scanned while monitoring emission at a fixed wavelength λem. In this way, the PLE spectrum shows which transitions contribute to the emission at λem, and a comparison of the PLE spectrum with the absorption spectrum provides a measure of the emission efficiency of the different transitions.

2.4. Time-Correlated Single Photon Counting

PL spectroscopy provides valuable information about the steady state fluorescence properties of an emitter. If we want to estimate how fluorescence evolves with time, we have to resort to time-resolved (TR) PL. Basically, a TR PL experiment provides a PL decay trace. If we excite an emitter promoting N carriers to their excited state, and then we allow them to relax to the ground state generating photons, the number of carriers in the excited state will drop exponentially over time. The easiest way to collect this decay would be to record over time the intensity of the emitted light by a fast photodetector. Unfortunately, this is not feasible, mainly due to the time resolution required. Time-correlated single photon counting (TCSPC) allows to overcome this hurdle. A TCSPC measurement can be schematized as follows: the sample is excited by a pulsed laser, and its response is observed over a properly selected time window; the time window is divided in a given number of time bins; the laser pulse starts a timer; when a photon is collected by the detector, the delay time is computed by fast electronics, and the counter associated to the proper time bin is incremented. A measurement like the one described would be possible if the detector and the electronics had no dead time after the processing of an event. In practice, this is not the case: a dead time exists, of at least some ns, in which the detection of emitted photons is not possible. If, on average, more than one photon is emitted in one excitation cycle, only the first photon is detected, while others arrive during the dead time and are lost. This yields a misrepresentation of the decay rate, since early photons are over-estimated in the histogram. This issue can be solved by tuning the excitation power so that the count rate at the detector does not exceed, typically, 5% of the laser repetition rate. By doing so, on average we will only have a photon event in 20 excitation cycles. The histogram is then created by repeated measurements over several laser pulses. Thanks to the ergodicity of the process, the histogram generated by the sparse photon events over multiple laser cycles contains the same information as if the decay of the carriers promoted with a single excitation event would have been collected over time. The TR PL measurements on NC ensembles reported in this work have been performed in TCSPC mode with an Edinburgh Instruments FLS920 spectrouorometer. A 405 nm or a

510 nm pulsed laser was used as excitation source, and the PL decay was measured in a region of typically 10 nm around the emission maximum. The pulse period was chosen to be at least 10 times larger than the longest decay component, to ensure a complete decay of the PL before the arrival of the successive pulse. Collected traces were then plotted with a sum of exponential functions, and an area-weighted average lifetime was calculated.

2.5. Low temperature PL spectroscopy

Steady-state PL spectra and time resolved PL (TRPL) lifetime were recorded with an Edinburgh Instruments fluorescence spectrometer (FLS920) coupled to an optical fiber. The schematic illustration of the measurement setup is depicted in Figure 2.1. The nanocrystal films deposited on a sapphire substrate (TedPella®) were placed inside a closed-cycle helium cryostat (Advanced Research Systems, Inc.). The steady-state PL were collected by exciting the sample with a 405 nm laser diode at 50 ns repetition period. The PL decay traces were recorded at the PL peak position by exciting the sample at 405 nm using a 50 ps laser diode at a repetition rate of 0.5-200 MHz and an emission bandwidth of 1-5 nm (see Figure 2.1).

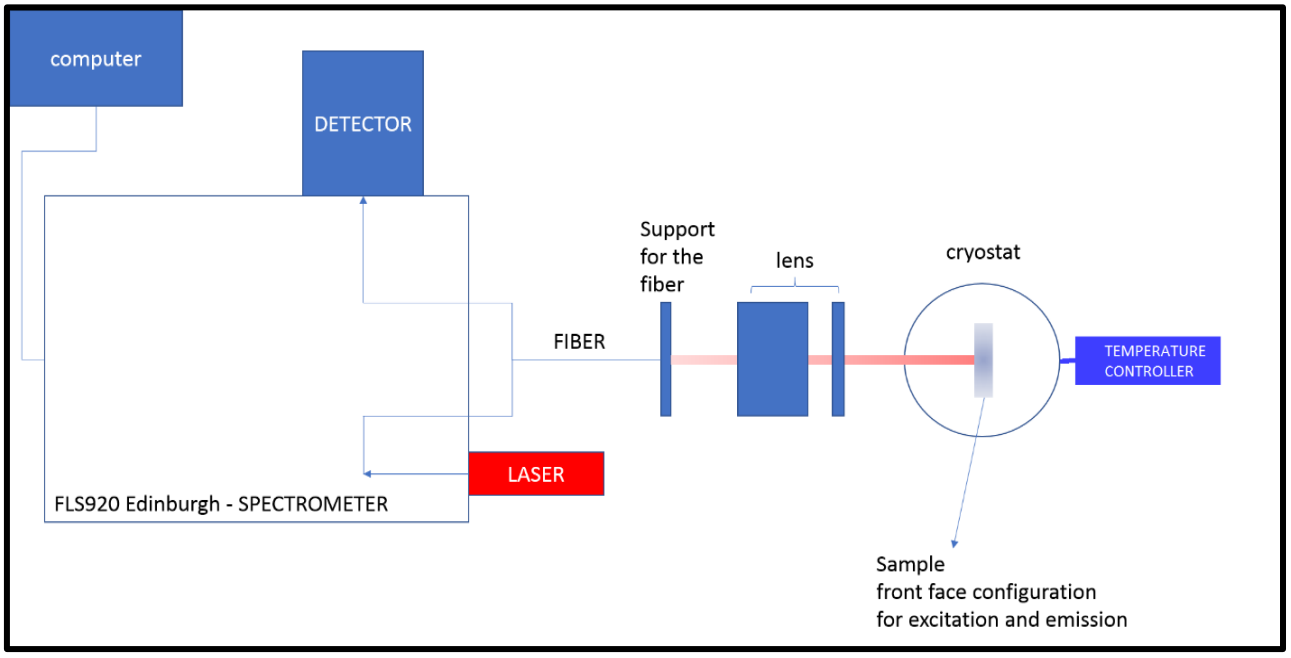

Figure 2.1. Schematics of the setup used for low temperature measurements.

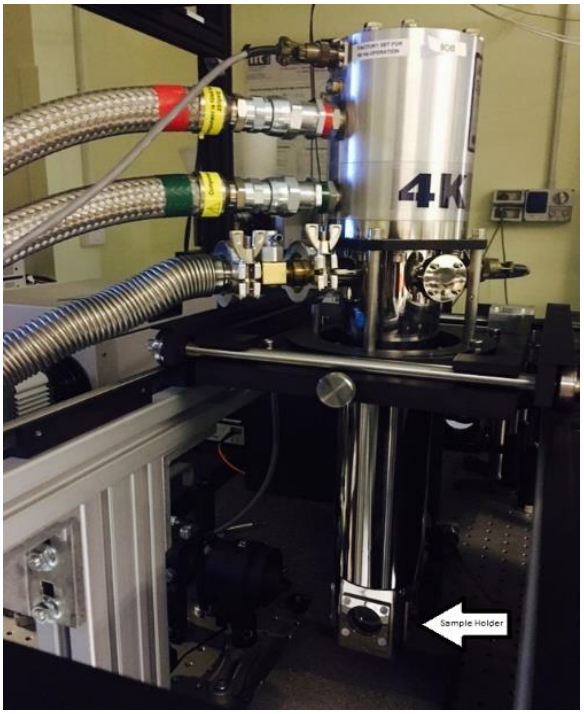

Figure 2. 2. Photograph of close-cycle helium cryostat system used for cooling down the samples to 4 K (Advanced Research Systems).

2.6. PL Quantum Yields measurements

The samples were measured with an Edinburgh FLS900 fluorescence spectrometer equipped with a Xenon lamp, a monochromator for steady-state PL excitation, and a time-correlated single photon counting unit coupled with a pulsed laser diode (λ_{ex} = 375 & 405 nm, pulse width = 50 ps) for time-resolved PL. The PLQY was measured using a calibrated integrating sphere (λ_{ex} = 350nm for all LHP NCs samples and λ_{ex} = 405nm). All solutions were diluted to an optical density of 0.1 or lower (at the corresponding excitation wavelength) in order to minimize the re-absorbance of the fluorophore.

2.7. Sample preparation

Colloidal dispersion of NCs sample was drop casted on sapphire substrate, sample was loaded into the cryostat and cooled down to 4K. The temperature was then slowly raised and fluorescence spectra and time-resolved fluorescence decay traces were collected with an Edinburgh Instruments FLS920 spectrofluorometer at selected temperatures while exciting the sample with a 405 nm pulsed laser. PL decay measurements were performed in time-correlated single photon mode, selecting a region of typically 10 nm around the peak maximum.

2.8. Synthesis and characterization of colloidal semiconductor NCs

Note: Synthesis of CdSe/CdS/CdTe core/barrier/crown NCs was done by Dr. Guillaume H.V. Bertrand and lead halide perovskite NCs by Dr. Muhammad Imran

2.8.1. Materials

Lead acetate trihydrate (($PbAc_2 \cdot 3H_2O$), 99.99%), caesium carbonate (Cs_2CO_3, reagent Plus, 99%), Formamedinium acetate (benzoyl bromide (C_6H_5COBr, 97%), acetone (99.5%), ethyl acetate (98.8%), toluene (anhydrous, 99.5%), didodecyldimethylammonium bromide (DDDMAB), Oleylamine (70%), octadecene (ODE, technical grade, 90%), toluene-d8 (99 atom. % D), dodecyldimethyl ammine, hydrobromic acid (HBr, 48% aqueous solution) and oleic acid (OA, 90%), were purchased from Sigma-Aldrich. Didodecylamine (DDDAm, 97%), was purchased from TCI. All chemicals were used without any further purification. $Cd(NO_3)_2.4H_2O$, $Cd(OAc)_2$, $Cd(OAc)_2.2H_2O$, sodium myristate, methanol, hexane, octadecene (ODE), trioctylphosphine (TOP) and oleic acid (OA) were purchased from sigma-Aldrich. elemental sulfur, selenium and tellurium powder were purchased from Strem chemicals. $Cd(OAc)_2$ and Se were stored in a glovebox.

2.8.2. Synthesis of CdSe/CdS/CdTe core/barrier/crown NPLs

CdSe/CdS/CdTe core/barrier/crown NPLs were prepared following or previously reported procedure.[1]

Cadmium myristate, $Cd(Myr)_2$ synthesis: In a 1000-mL round bottom flask 5 g of sodium myristate (20 mmol) was dissolved in 250 mL of methanol using sonication and vigorous stirring. In a second 500 mL round bottom flask 3 g of $Cd(NO_3)_2.4H_2O$ (10 mmol) was dissolved in methanol. The latter cadmium solution was then added dropwise to the first, and subsequently stirred for 2 h at room temperature. A white precipitate formed, which was filtered and washed with 20 mL of methanol three times. The remaining white solid was vacuum dried at 40 °C overnight affording 4.5g of $Cd(Myr)_2$ (7.9 mmol, 79% reaction yield). The $Cd(Myr)_2$ water content was measured with thermo-gravimetric analysis (TGA), and it was stored in the dark at 4°C. Synthesis of CdSe NPLs (Core): In a 50 mL three neck round bottom flask 150 mg of $Cd(Myr)_2$ (0.26 mmol), 24 mg of Se powder (0.30 mmol) and 15 mL of ODE were degassed under vacuum at 110°C for 20 min. The mixture was placed under argon atmosphere and heated to 140 °C for 10 to 20 min to achieve total dissolution of the Se powder. The temperature was then set to 240 °C with a ramp of 50 °C.min^{-1}. When the solution start to transform from yellow to orange (between 205 and 215

°C), the reaction vessel was opened and 80 mg of $Cd(OAc)_2$ (0.35 mmol) was swiftly added. After 8 min the heating mantle was withdrawn, the reaction mixture slowly cooled to 160 °C, at which point 2 mLmL of OA was added. When reaching room temperature, the mixture was transferred to a 50 mL vial with 20 mL of hexane and centrifuged for 10 min at 3000 rpm. The supernatant was discarded and the remaining precipitate was dispersed in 40 mL of hexane. The resulting solution was centrifuged again at 5000 rpm. The desired platelets remain in the supernatant; the precipitate was discarded.

CdS growth solution: A 0.1M solution of ODE.S in ODE was prepared by heating 32 mg of elemental sulfur in 10 ml of ODE. The CdS growth solution was then prepared by mixing 2 ml of the 0.1 M ODE.S solution, 3 ml of ODE, 350 µl of OA and 400mg of $Cd(OAc)_2.2H_2O$. the resulting mix is the sonicated for 2 to 3h resulting in a white gel.

CdTe growth solution: The growth solution was prepared by mixing 75µl of the 1M TOP.Te with 1ml of ODE right before injection.

CdSe/CdS (Core/Crown): In a 50 mL three neck round bottom flask, a batch of CdSe in hexane was placed under argon flow to evaporated most of the hexane, the remaining slurry was then dissolved in 12 ml of ODE and 100 mg of $Cd(propionate)_2$ were added to the reaction mixture. It was then stirred under vacuum at 110°C for 20 min. After this degassing step, the mixture was placed under argon and heat to reach 235°C. Using a syringe drive, the CdS growth solution was added dropwise (3ml/h) in time varying from 2 to 12 min. The addition was stopped when desired and the solution was let stirring at 235°C for another 5 min, and then allowed to reach room temperature. At 160°C 2 ml of OA where added. The solution was diluted in 20 ml of Hexane and then centrifuged at 6000 rpm for 10 min. The supernatant was discarded as the desired NPLs formed the precipitate.

CdSe/CdTe (Core/Crown): In a 50 mL three neck round bottom flask, a batch of CdSe in hexane was placed under argon flow to evaporated most of the hexane, the remaining slurry was then dissolved in 12 ml of ODE and 100 mg of $Cd(propionate)_2$ were added to the reaction mixture. It was then stirred under vacuum at 110°C for 20 min. After this degassing step, the mixture was placed under argon and heat to reach 235°C. Using a syringe drive, the Te growth solution was added dropwise (3ml/h) in 8 min. The addition was then stopped when desired and the solution was let stirring at 235°C for another 5 min, and then allowed to reach room temperature. At 160°C 2 ml of OA where

added. The solution was diluted in 20 ml of Hexane and then centrifuged at 4000 rpm for 5 min. The supernatant was discarded as the desired NPLs formed the precipitate.

CdSe/CdS/CdTe (Core/Barrier/Crown): In a 50 mL three neck round bottom flask, a batch of CdSe in hexane was placed under argon flow to evaporated most of the hexane, the remaining slurry was then dissolved in 12 ml of ODE and 100 mg of Cd(propionate)$_2$ were added to the reaction mixture. It was then stirred under vacuum at 110°C for 20 min. After this degassing step, the mixture was placed under argon and heat to reach 235°C. Using a syringe drive, the CdS growth solution was added dropwise (3ml/h) in time varying from 1 to 12 min. The addition was stopped when desired and the solution was let stirring at 235°C for another 5 min, Using a syringe drive, the Te growth solution was added dropwise (3ml/h) in time varying from 2 to 16 min The addition was then stopped when desired and the solution was let stirring at 235°C for another 5 min, and then allowed to reach room temperature. At 160°C 2 ml of OA where added. The solution was diluted in 20 ml of Hexane and then centrifuged at 4000 rpm for 5 min. The supernatant was discarded as the desired NPLs formed the precipitate.

2.8.3. Synthesis of lead halide perovskite NCs

APbBr$_3$ (A=Cs, MA, FA) NCs: First generation of APbBr$_3$ NCs were prepared using typical ligands such as oleic acid and oleylamine following a previously reported procedure.[2] Briefly, 76 mg of lead (II) acetate trihydrate, 16 mg of cesium carbonate, 0.3 mL of oleic acid, 1.0 mL of oleylamine and 10 ml of ODE were combined in a 25 ml 3-neck flask equipped with a thermocouple and a magnetic stirrer. The reaction mixture was degassed for 5 minutes at room temperature and then for one hour at 120 °C. Next, the temperature was increased to 175 ^{o}C and a solution of benzoyl bromide (70 µL) in ODE (500 µL, which had previously been degassed for an hour at 120 °C and stored in glove box) was swiftly injected. The reaction mixture was immediately cooled down using an ice-water bath. Thereafter, 5 mL of toluene was added to the crude solution, then it was centrifuged at 5000 rpm for 10 minutes. The supernatant was discarded, and the precipitate was redispersed in 5 mL of toluene.

2.8.4. Synthesis of Cs-Oleate capped CsPbBr$_3$ NCs

Cs-oleate capped CsPbBr$_3$ NCs were synthesized following our previously reported procedure using standard Schlenk line techniques.[3] 1st step, Degassing: 76 mg of lead (II) acetate trihydrate, 16 mg of cesium carbonate and 10 ml of octadecene (measured with a 5 ml mechanical pipette) were combined in air in a 25 ml 3-neck flask (one of the side necks is used as a glass finger for a

thermocouple, and is filled with 0.5 ml of octadecene as a heat transfer medium). The flask with the mixture was equipped with a magnetic stirrer, and the open side neck was capped with a silicone septum and connected to a Schlenk line via a condenser that was inserted into the central neck. It was then placed into the heating mantle on top of a stirring plate. The vacuum was applied first at room temperature for ~5 minutes as a pre-degassing step. Within a few minutes, the contents of the flask were heated to 115 ^{o}C under stirring and were kept at that temperature, under vacuum, for approximately one 1 hr. The vacuum was ~50-70 mbar, as was measured with a digital vacuum gauge.

2nd step, Ligands: In the glovebox, 1 ml of anhydrous toluene was added to 443 mg of DiDDAm in a 4 ml glass vial, which was then placed on a preheated hot plate (set at 150 ^{o}C) until all the DiDDAm dissolved (m.p.= 45-47 ^{o}C). Next, 1.5 ml of the degassed oleic acid was added to the DiDDAm solution using a 5 ml mechanical pipette. The resulting mixture of ligands was shaken by hand, yielding a clear and colorless solution. The ligand solution was transferred into a 5 ml disposable syringe equipped with a 21G needle, which was then removed from the glovebox.

After the metal salts had degassed (1st step above), the flask with metal salts in ODE was switched from being under vacuum to being under nitrogen flow, and the ligand mixture in toluene was injected. After adding the ligands, the reaction mixture was kept at 115 ^{o}C under stirring until all of the metal salts dissolved (~15-20 minutes), yielding a clear, colorless solution without any visible solids inside. Next, the temperature controller was set to 80 ^{o}C (the injection temperature), and the reaction mixture was allowed to cool and stabilize at 80 ^{o}C.

3rd step, Injection of benzoyl bromide: In the glovebox, 50 uL of benzoyl bromide (measured with a 100 uL mechanical pipette) was mixed with 500 uL of degassed ODE (measured with a 1000 uL mechanical pipette) in a 4 ml glass vial; the mixture was shaken by hand and filled into a 3 ml disposable syringe equipped with a 21G needle. The benzoyl bromide solution was taken outside the glovebox, and injected into the mixture of metal salts and ligands at 80 ^{o}C under stirring. Upon the injection of the benzoyl bromide precursor, the reaction mixture immediately turned from being clear and colorless to being clear and yellow (which is characteristic of $CsPbBr_3$ NCs). After the injection, ~15 seconds were counted with a timer, and the reaction was quenched by replacing the heating mantle with a water bath (at ~20 ^{o}C). The reaction was left to cool until it reached ~40 ^{o}C, after which the water bath was removed. During both injection and cooling, the reaction was kept under a nitrogen atmosphere.

4th step, Isolation of nanocubes: Once the reaction had cooled down to near room temperature, the flask was opened in air and the contents were transferred into a 40 ml vial. 3 ml of anhydrous toluene was then added to the vial, followed by anhydrous ethyl acetate until the mixture turned turbid. Note that the total volume of ethyl acetate needed for nanocrystal precipitation depends on the size of the nanocubes. For the injection temperature and growth time described here (80 ^{o}C and ~15 seconds, respectively), it took ~20-30 ml of ethyl acetate to initiate nanocrystal agglomeration (mixture turns turbid). When agglomeration started, the mixture was centrifuged at 5000 rpm for 10 minutes, yielding yellow precipitate on the walls of the vial and a yellow supernatant. The supernatant was discarded and the precipitate was dispersed in a few ml of toluene for characterization and further experiments (such as self-assembly).

2.8.4. Synthesis of QAB capped $CsPbBr_3$ NCs

QAB capped $CsPbBr_3$ NCs were prepared following a previously reported ligand exchange strategy.[4] Briefly, Cs-oleate capped NCs were prepared following above mentioned procedure[2] and the crude reaction mixture containing the $CsPbBr_3$ NCs (3 mL) were treated with an anhydrous toluene solution containing the ammonium bromide salt (2 mL, 0.025M) and the mixture was vigorously stirred for 1 minute. Thereafter, the NCs were washed by addition of 15 mL of ethyl acetate followed by centrifugation at 6000 rpm for 10 minutes and re-dispersion in toluene.

2.9. Transmission Electron Microscopy (TEM) characterization

The samples were prepared by dropping dilute solutions of NCs onto carbon coated copper grids. Low-resolution bright-field TEM (BF-TEM analyses were performed on a JEOL JEM-1011 TEM (thermionic source: W filament) operating at an acceleration voltage of 100 kV."

2.10. References

1. Bertrand G.H.V, Teitelboim A, Angeloni I, **Ijaz P**, Polovitsyn A, Oron D, Moreels I. CdSe/CdS/CdTe Core/Barrier/Crown Nanoplatelets, Synthesis, Optoelectronic Properties and Evidence of Three Photons up-conversion (in preparation).
2. Imran M, Caligiuri V, Wang M, Goldoni L, Prato M, Krahne R, De Trizio L, Manna L. Benzoyl halides as alternative precursors for the colloidal synthesis of lead-based halide perovskite nanocrystals. Journal of the American Chemical Society. 2018 Jan 29;140(7):2656-64.
3. Imran M, **Ijaz P**, Goldoni L, Maggioni D, Petralanda U, Prato M, Almeida G, Infante I, Manna L. Simultaneous Cationic and Anionic Ligand Exchange For Colloidally Stable CsPbBr3 Nanocrystals. **ACS Energy Letters**. **2019**, 4; 4(4):819-24.
4. Imran M, **Ijaz P**, Baranov D, Goldoni L, Petralanda U, Akkerman Q, Abdelhady AL, Prato M, Bianchini P, Infante I, Manna L. Shape-Pure, Nearly Monodispersed CsPbBr3 Nanocubes Prepared Using Secondary Aliphatic Amines. **Nano letters**. **2018**, 1; 18(12):7822-31.

Chapter 3. Temperature dependent optical properties of CdSe/CdS/CdTe core/barrier/crown nanoplateles

ABSTRACT: Nano-platelets heterostructure are particularly interesting as they combine the strong anisotropic confinement of 2D materials with the wide range of properties of semiconductor junction. We present here the detailed spectroscopy study of ternary architecture consisting of a core of CdSe surrounded by a barrier of CdS and crowned by CdTe. The optical behavior of this Core/Barrier/Crown (CBC) nanocrystal were investigate in temperature range from T = 4–300 K in order to identify temperature dependence of exciton−phonon coupling, bandgap energies and excitonic linewidths as a function their barrier size. CBC nanoplatelets present a large optical absorption cross-section and band alignment that can promote multiple excitonic behavior. We uncovered several interesting properties of this novel ternary structure including nearly almost temperature-independent PL decays.

3.1. Introduction

Among quantum confined nanostructures, 2D materials can give access to strong and weak confinements at the same time. In the past few years nano-platelets (NPLs) took a prominent place in this field and demonstrate remarkable opto-electronics properties. Synthesis of NPLs recently took a step forward giving access to different cadmium chalcogenide zinc-blende materials. In particular CdSe NPLs are the center of many studies concerning the control of their synthesis, relationship between shape and exciton dynamics and auto assembly properties. This properties can be combined with all the material design existing for spheres particle, especially binary architecture. Shape is a very important parameter in semiconductor nanostructures because it can strongly affect the opto-electronic properties. 2D semiconductor nanoplatelets (NPLs) are also known as quantum wells (QWs). These NPLs are atomically flat quasi two-dimensional (2D) quantum-confined nanocrystals and typically composed of wide bandgap II-VI materials. High quality single crystal nanoplatelets samples are synthesized by colloidal chemistry. [1-8]

Indeed spherical core-shell structure can be transpose in 2D affording brick in brick (core-shell) structure or the more peculiar core-crown architecture. In this last family a secondary materials is grown on the facets perpendicular to the core NPL main plane, extending the 2D structure. The core and crown material can be chosen to design band alignment of interest such as type I or type II interface. This offer unique property such as antenna effect and exciton concentration of the CdSe/CdS Type I core crown sytem, or a long lifetime type II transition in CdSe/CdTe core-crown NPLs. This last example is very interesting as it only present type II emission, even though intrinsic CdSe and CdTe emission are much faster.[9-14] Exciton wave function can be further manipulate by inserting a barrier in between the type II junction. In CdSe/CdS/CdTe heterostructures, the core and crown material is chosen such that the CdS forms a tunneling barrier for holes in the valence band, while electrons can relax from the CdTe crown to the CdSe core via the cascaded band offset in the conduction band. This yield simultaneous type I and type II emission. The uniform 1D quantum confinement in the core crown NPLs leads to sharp peaks in the absorption and photoluminescence spectra of the NPLs at the room temperature. In this chapter we investigated in detail the photophysical properties of CdSe/CdS/CdTe core/barrier/crown system associated with its band structure and its applications.

3.2. Results and discussion

Following previous reports, different CdSe NPLs with control size and aspect ratio were synthesized. These CdSe NPLs were used as a core of our desired 2D ternary architecture and will be referred to as core NPLs (C-NPLs). It is worth mentioning here that the initial attempt to grow CdTe shell directly on the CdSe/CdS NPLs was unsuccessful. This was most likely due to lattice higher lattice mismatch between CdS and CdTe (5.832 Å and 6.482 Å respectively) which consequently prevented the nucleation of CdTe over CdS. To overcome this problem, single pot synthesis method was adopted by adding CdS and CdTe growth solution consecutively without isolation and purification of the CdS. Simultaneous addition of both precursors create a zone of transition between the CdS and the CdTe, that allowed lattice constant to relax and paved the way to grow CdSe/CdS/CdTe hetro-NPLs. Nevertheless, this growth might be due to the formation of the gradient in composition Cd(SxTe1-x) which subsequently help the growth of ternary structure but would need further in-depth structural analysis.

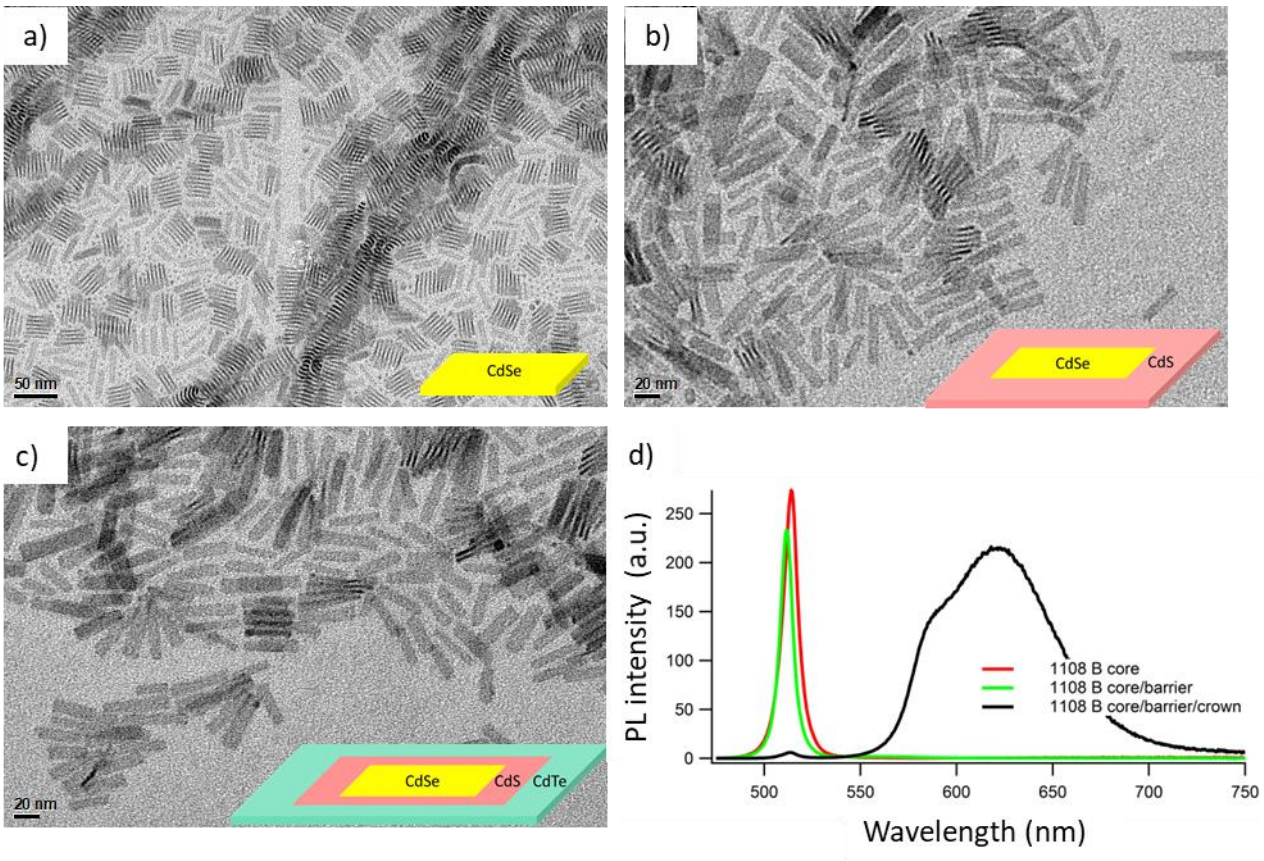

Figure 3. 1. TEM images of the nanoplatelets: a) TEM image of CdSe core used as a seed materials for CBC synthesis. b) TEM image of an aliquot taken between the slow addition of CdS growth solution and CdTe growth solution. c) TEM image of CdSe/CdS/CdTe-NPLs. d) Emission spectra

measured in colloidal dispersion of CdSe, CdSe/CdS, and CdSe/CdS/CdTe core crown barrier nanoplatelets.

Synthesis details of CdSe/CdS and CdSe/CdS/CdTe NPLs are reported in chapter 2. Figure 3.1. Shows the bight field transmission electron microscope images (BE-TEM) of CdSe NPLs used as a seed (a), intermediate stage after injection of CdS growth solution and CdTe growth solution (b) and finally the TEM image of CdSe/CdS/CdTe-NPLs (c). Emission spectra measured in colloidal dispersion of CdSe, CdSe/CdS, and CdSe/CdS/CdTe NPLs are reported in Figure 3.1-d. The lateral dimensions of CBC NPLs are much larger than their thickness and brief summary about the lateral dimension of all the sample is reported in table 3.1. We carried out the measurements on pristine CdSe/CdS and CdSe/CdS/CdTe core crown barrier of various aspect ratios. Thin films of densely packed NCs were prepared by drop casting colloidal dispersion on a sapphire substrate. The samples were loaded in a close-cycle helium cryostat (Advanced Research Systems) and cooled down to 4 K. The temperature was then slowly raised and fluorescence spectra and time-resolved fluorescence decay traces were collected with an Edinburgh Instruments FLS920 spectrofluorometer at selected temperatures while exciting the sample with a 405 nm pulsed laser. PL decay measurements were performed in time-correlated single photon mode, selecting a region of typically 10 nm around the peak maximum.

Table 3.1: Overall dimensions of the samples investigated in this chapter, size of CdSe core, CdS barrier and CdTe crown

Sample Name	**Core**			**Barrier**			**Barrier Thickness**	**Crown**		
	Length	Width	AR	Length	Width	AR		Length	Width	AR
99	24.5	8.5	2.9	28	10	2.8	1.5			
1108A	30.8	5.8	5.3	33.6	6.7	4.9	0.9	35.4	8.8	4.0
1108B	27.4	7.8	3.5	34.5	9.9	3.5	2.1	47.4	12.4	3.8
1108C	27.4	7.8	3.5	36.7	9.5	3.8	1.7	43.0	12.5	3.4
1116	20.3	6.6	3.1	20.6	6.7	3.1	0.1	38.2	11.7	3.3

3.3. Temperature dependence of photoluminescence

For CdSe/CdS (Type I) and CdSe/CdS/CdTe (Type I + Type II) NPLs samples, the photoluminescence were recorded in the temperature range from 4K to 300K. Figure 3.2 shows typical PL spectra (after background correction) and their evolution as a function of temperature of 4–300 K for Sample 99 (CdSe/CdS). It can be observed that as the temperature increases, the PL intensity decreases. There

is also a red shift in the emission wavelength as the temperature increases from 4 to 300 K. In addition, the spectrum broadens at higher temperatures due to electron-phonon coupling.

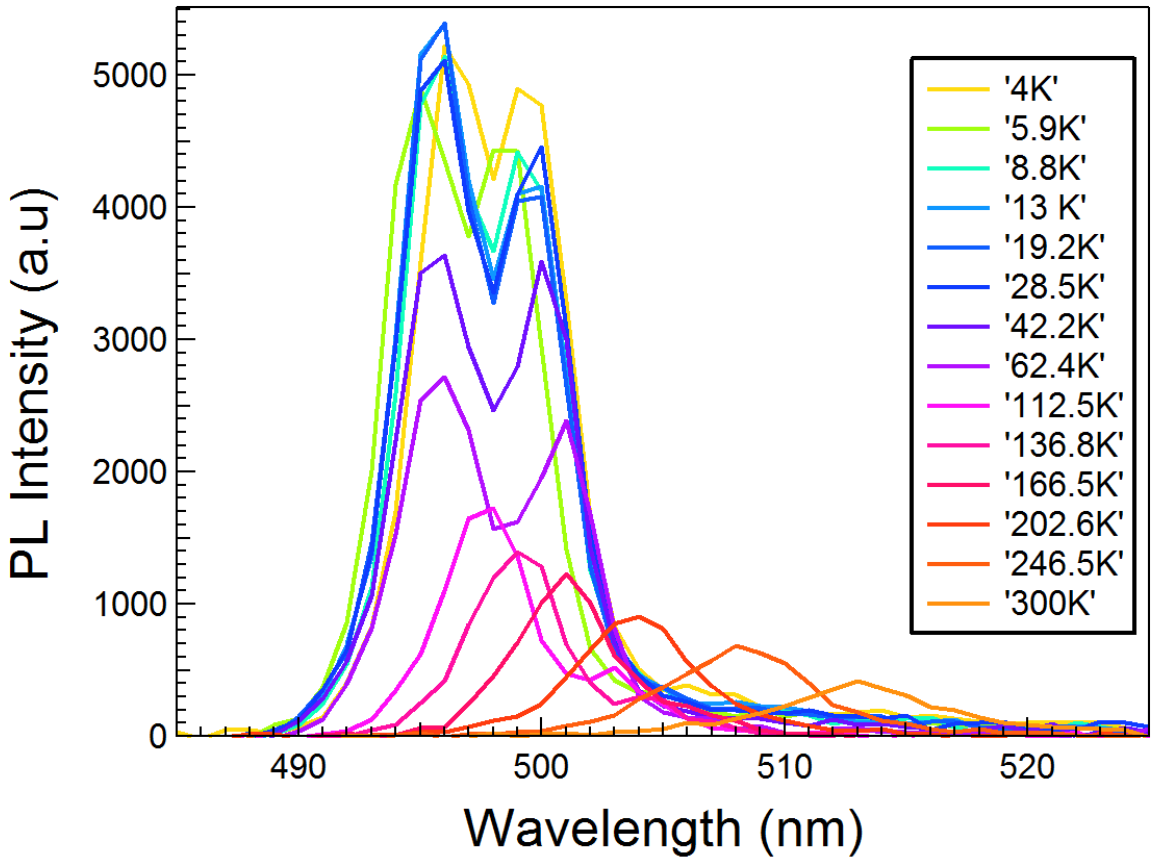

Figure 3. 2. PL spectra of CdSe/CdS NPLs measured from 4 to 300 K.

Similarly, we carried out the measurements on CdSe/CdS/CdTe (Type I + Type II) CBC NPLs of various aspect ratios (shown in table 3.1), PL spectra recorded from 4K to 300K are reported in figure 3.3. We observed dual emission from CdSe core and single emission from CdSe/CdTe interface in all 4 samples of CBC. The trends of PL quenching in core at elevated temperatures were similar to CdSe/CdS NPLs. Assuming a temperature independent exciton binding energy, the excitonic redshift is a result of electron–phonon interaction and the thermal expansion of the lattice. The most fundamental properties is the energy band gap, Eg, which is affected by temperature as already demonstrated above. After background correction, emission maxima of Type I and Type II transitions

for all samples are plotted as a function of temperature in figure 3.4 and figure 3.5. Figures shows that the Band gap decrease as temperature increases.

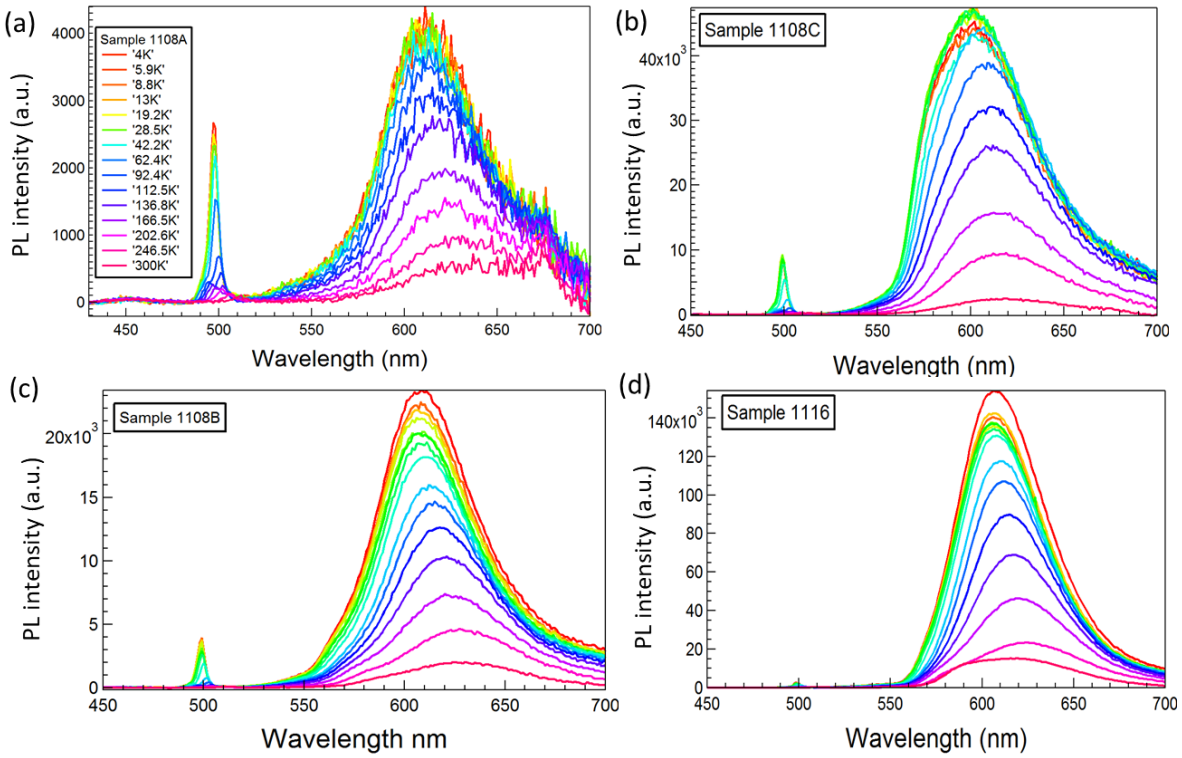

Figure 3. 3. PL spectra of CdSe/CdS/CdTe NPLs measured from 4 to 300 K exhibiting dual emission from CdSe core and CdSe/CdTe interface.

Different models are used to link the bandgap renormalization to the phonon coupling. Earlier studies revealed that the bandgap shrinkage can be described in a Bose model with a exciton–phonon coupling constant a_{ep}. [15-17] Accordingly, we employed the same expression.

$$E_{exc}(T) = E_{exc}(0) - \frac{2a_{ep}}{e^{\frac{\theta}{T}} - 1} \qquad (1)$$

Here *Eexc(0)* accounts for the exciton energy at *T = 0 K*, and $\theta = \langle EPhonon \rangle / K_B$ is an average phonon temperature. By using eq. (1), we tried to fit temperature dependent PL emissions of all the samples by using Igor Pro software. The obtained fits for Type I transitions (CdSe/CdS) for sample 99

and other CBC samples are displayed in Fig. 3.4 and Fig. 3.5. For the electron−phonon couplings, we obtained the values listed in Table 3.2. The obtained average phonon temperatures θ seem to be similar within the fitting errors for both Gauss 1 and Gauss 2 in Type I transitions.

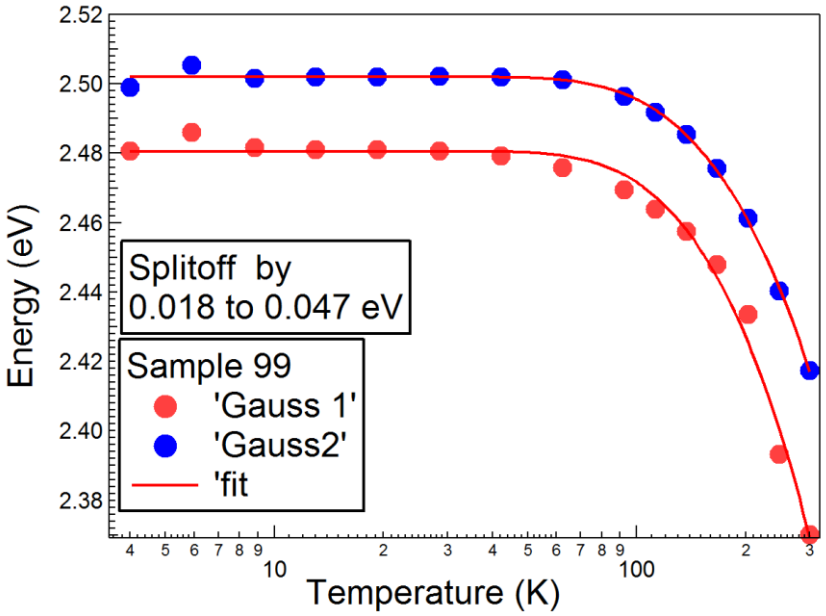

Figure 3. 4. Type-I transitions .Energy gap as a function of temperature for sample 99, dotted line are the results of experimental data and solid lines are results of fits derived from equation (1).

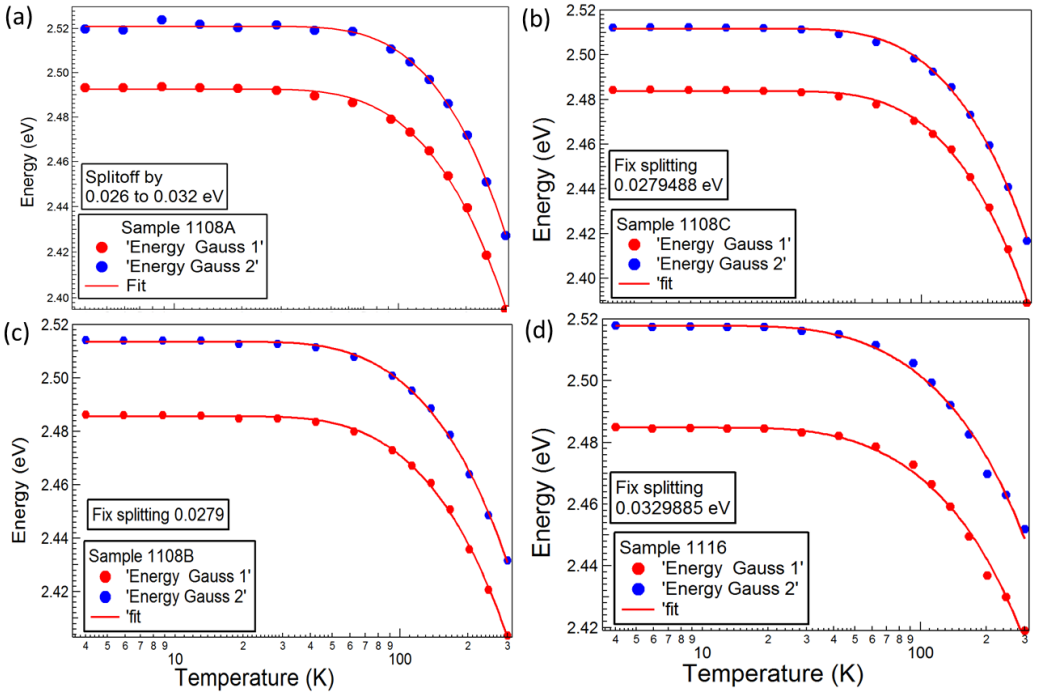

Figure 3. 5. Type-I transitions, Energy gap as a function of temperature for CdSe/CdS/CdTe samples of various aspect ratios, blue and red dotted line are the results of experimental data of PL maxima's w.r.t temperatures and solid lines are results of fits derived their equation (1).

Compared our data with bulk like zinc blend (ZB) epilayers by Chia et. al [18] who reported Eexc (0) = 1.739 eV, aep = 21 meV, and θ = 203 K. In our results the elevated exciton energy Eexc (0) up to 2.4925 eV and the reduced values of the average exciton-phonon coupling constant a_{ep} = 1.28 meV and average phonon temperature θ = 94.7 K may be due to increased quantum confinement effects in the NPLs.

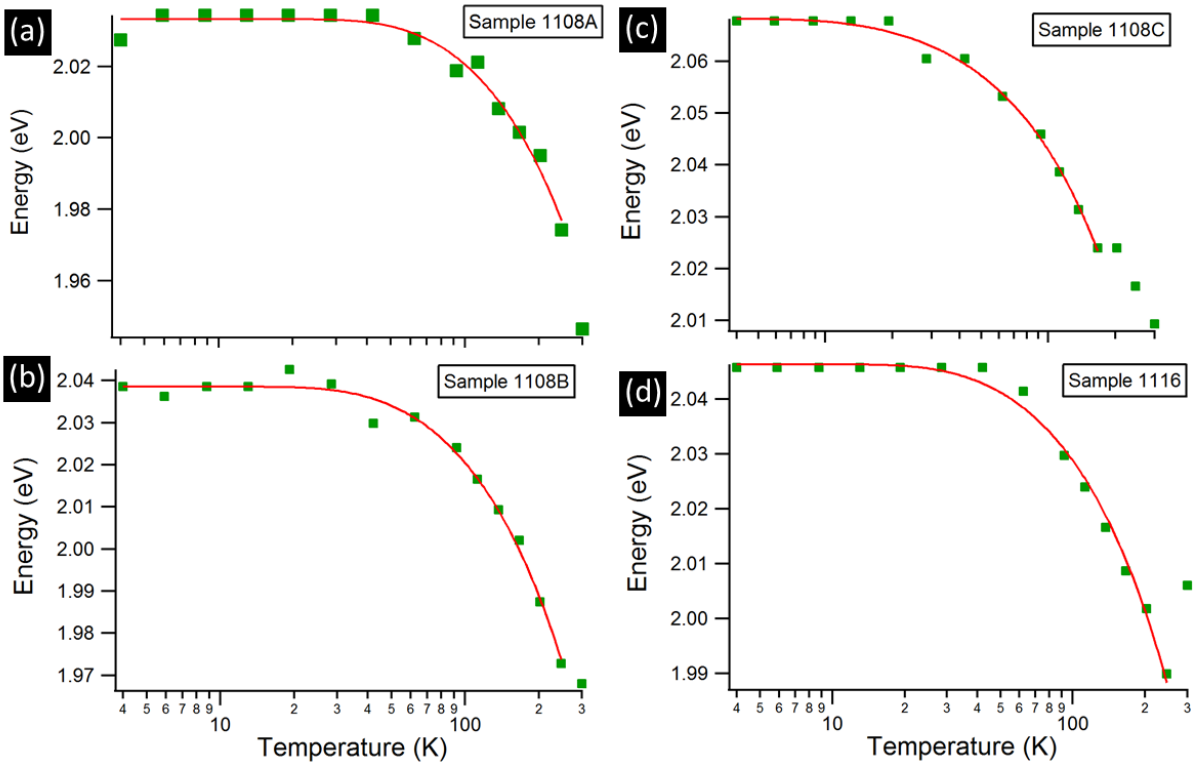

Figure 3. 6. Type-II transitions, Energy gap as a function of temperature for CdSe/CdS/CdTe samples of various aspect ratios, green dotted line are the results of experimental data of PL maxima's w.r.t temperatures and solid lines are results of fits derived their equation (1). All samples shows a similar red shift with increasing temperature.

Table 3.2: Results of Bose fits model for Type-I transition

	Gauss 1				Gauss 2			
Samples	$E_{exc}(0)$ (eV)	a_{ep} (eV)	Θ (K)	$\langle E\ Phonon\rangle$ (meV)	$E_{exc}(0)$ (eV)	a_{ep} (eV)	Θ (K)	$\langle E\ Phonon\rangle$ (meV)
99	2.48	0.11	321.04	27.67	2.50	0.086	332.01	28.61
1108A	2.49	0.04	192.53	16.59	2.52	0.057	238.15	20.52
1108C	2.48	0.04	190.97	16.46	2.51	0.042	190.96	16.46
1108B	2.49	0.03	162.24	13.98	2.51	0.029	162.24	13.98
1116	2.48	0.01	94.758	8.17	2.52	0.013	94.748	8.17

Our values are in good agreement results of Achtstein et al.[11] who reported Eexc (0) = 2.440 eV. Average phonon energy also reduced with respect to average phonon temperature as we can noticed from the Table 3.2. From above figures, we can see that Band gap decrease as temperature increases

because increase in lattice constant can cause increase in the electron-phonon interaction and which decrease the band gap. The interaction of excitons with phonons does not only cause a shift of the bandgap energies, but phonon scattering also leads to significant broadening of the emission lines. The obtained average phonon temperatures θ seem to be similar within the fitting errors for both Gauss 1 and Gauss 2 in Type I transitions. Whereas the increased confinement in the NPLs has reduced the average exciton-phonon coupling constant a_{ep}, also evident from the significant reduction in average phonon temperature θ. Similarly, Type II transitions are fitted with Bose model as displayed in Fig. 3.6. The best-fit parameters obtained for the electron-phonon couplings are listed in Table 3.3.

Table 3.3: Results of Bose fits model for Type-II transition

Samples	$E_{exc}(0)$ (eV)	a_{ep} (eV)	Θ (K)	$\langle E\ Phonon\rangle$ (meV)
1108A	2.0332	0.027	167.06	14.39
1108B	2.0385	0.018	111.48	9.60
1116	2.0463	0.013	89.799	7.73
1108C	2.0682	0.004	28.53	2.45

3.4. Temperature dependence of Line Width (FWHM)

The interaction of excitons with phonons does not only cause a shift of the bandgap energies, but phonon scattering also leads to significant broadening of the emission lines. Both acoustic and optical phonons contribute to this process. On the basis of a model proposed by Logothetidis, Cardona and co-workers [19] and also applied for CdSe NPLs[12, 13] the temperature dependence of the linewidth of excitonic peaks is given by,

$$\boldsymbol{\Gamma(T) = \Gamma_0 + \Gamma_{AC} T + \Gamma_{LO} \exp\left(-E_{LO}/K_B T\right) - 1)\text{^}1} \qquad (3.2)$$

Where Γ_0 corresponds to the inhomogeneous contribution to the line width, Γ_{AC} is the acoustical phonon-coupling constant. Γ_{LO} yields the contribution of optical phonons of energy E_{LO}. The last term comes from exciton-longitudinal optical (LO) phonon Fröhlich interaction and it is proportional to the Bose occupation function for LO phonons. Γ_{LO}The *T* dependence of $\Gamma(T)$ is shown in Fig. 3.7 and Fig. 3.8 for Type I transitions in sample 99 and in other CBC samples. Similarly, temperature

dependence of PL line width for Type II transitions in CBC samples are shown in Fig. 3.9. All figures clearly show that the FWHM increases with the temperature. This is because of thermal effects induces exciton-phonon coupling. The line-width parameter FWHM is also analyzed to obtain information on the exciton–phonon coupling in the temperature range 4–300 K. The solid red lines are a three parameters (Γ_0, Γ_{AC} and Γ_{LO}) least square fit of the experimental data (red and blue circles to the eq. 3.2 for Type I and Type II transitions, respectively for all the samples.).

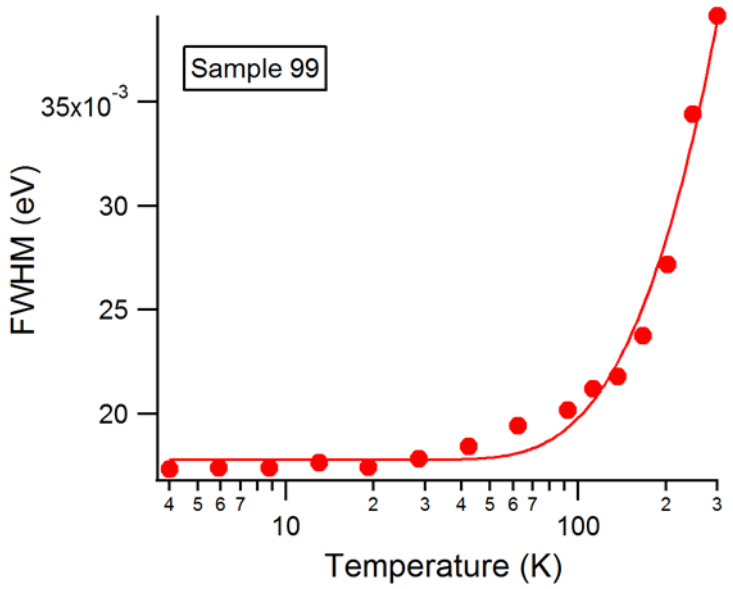

Figure 3. 7. Evolution of PL line width as a function of temperature for sample 99.

We have used E_{LO} = 25.0 meV for our CBC NPLs from Achtstein et al.[12] and fixed it to fit the other parameters of eq. 2. For practical reasons, we omitted the contribution of Γ_{AC} as compared to Γ_{LO} it is negligible. [12,13] Table 3.4 shows the results for the temperature dependent line width for both Type I and Type II transitions of all samples. It is clearly observe from figures (3.7 & 3.8) that the change in FWHM is quite linear until 92.4 K, beyond which it increases at a relatively faster rate. This rise in homogeneous broadening above 92.4 K is attributed (partially) to the exciton–LO-phonon scattering. As can be seen from Table 3.4, Γ_{LO} values obtained for Type I transitions are smaller (12.6 –34.5 meV) than the values for Type II transitions (159.5 –569.1 meV). Furthermore, the additional broadening is attributed to the exciton scattering with defect/surface states.[14]

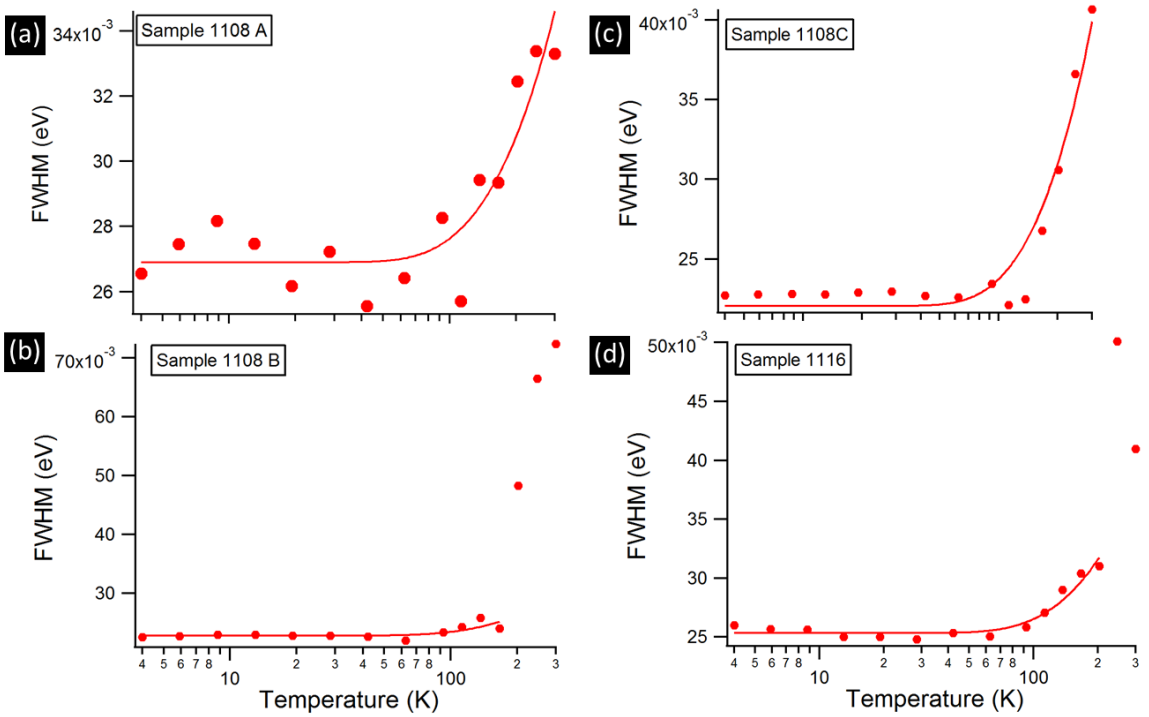

Figure 3. 8. PL line width as a function of temperature for CdSe core in various aspect ratios of CdSe/CdS/CdTe CBC NPLs.

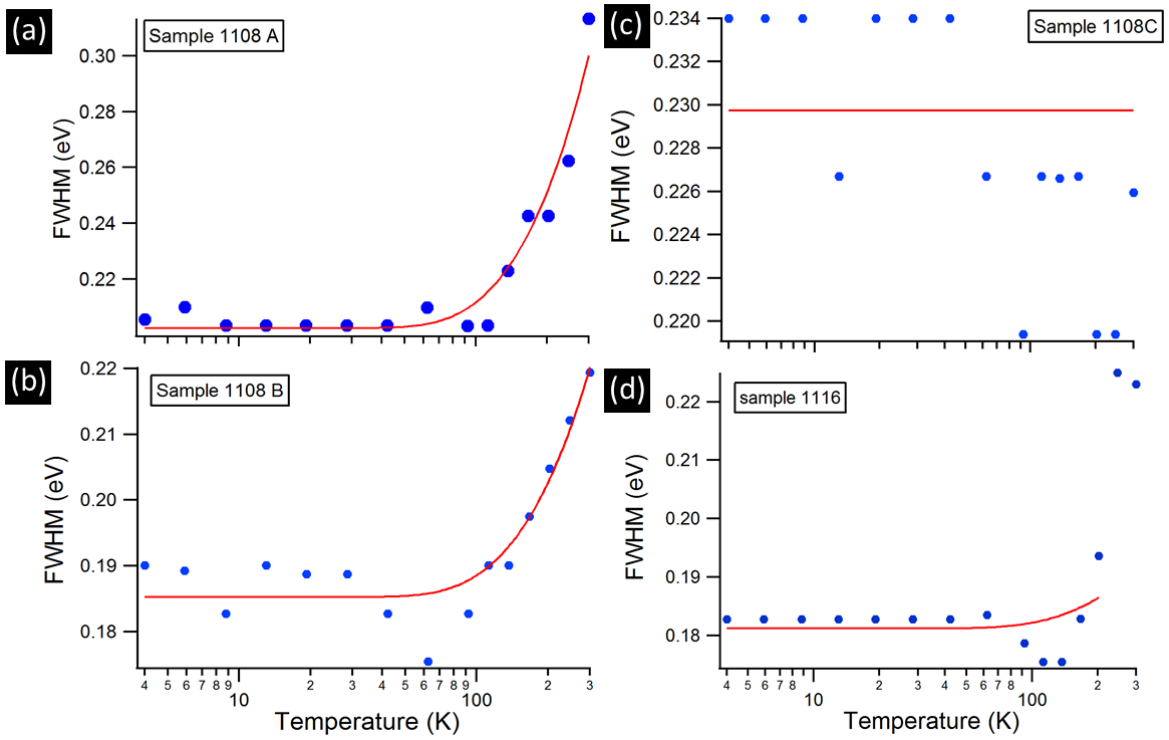

Figure 3. 9. PL line width as a function of temperature for CdSe/CdS/CdTe CBC NPLs of various aspect ratios.

Table 3.4 Results of Line width fits of eq. 2 for Type I and Type II transitions

Type I Line width				Type II Line width			
Samples	Γ_0 (meV)	Γ_{LO} (meV)	Barrier Thickness	**Samples**	Γ_0 (meV)	Γ_{LO} (meV)	Crown Thickness
99	17.8 ± 0.267	34.47 ± 1.2	1.5	**1108A**	202.35 ± 2.32	159.47 ± 10.4	4
1116	25.3 ± 0.182	20.50 ± 1.59	0.1	**1116**	181.22 ± 1.41	169.98 ± 12.3	3.3
1108A	26.9 ± 0.351	12.57 ± 1.57	0.9	**1108B**	185.28 ± 1.35	569.13 ± 6.07	3.8
1108B	22.8 ± 0.236	11.22 ± 3.04	2.1				
1108C	22.1 ± 0.453	29.11 ± 2.03	1.7				

In colloidal semiconductor NCs, the intrinsic emission FWHM is dominated at room temperature by thermal effect via exciton–phonon coupling. It is interesting to compare our results with conventional hexagonal CdSe nanodots, CdSe films, CdSe/ZnS quantum dots, cubic CdSe thin films, colloidal CdSe nanoplatelets and CdS quantum dots as arranged in Table 3.5. Valerini et al.[20] have shown the presence of multiple temperature dependent non-radiative processes in PL relaxation dynamics. At higher temperature, the contribution of LO phonons becomes predominant, eventually dominating the excitonic linewidth.

Table 3.5: Previous findings about line width coefficients of Type I transitions for different NCs

Coefficients of eq. (3.2)		Perna et al.[Error! Reference source not found.] (Hexagonal **CdSe films** deposited on both Si(111)&Si(100)substrates)	Velerini et al.[Error! Reference source not found.] CdSe/ZnS core/shell QDs	Salman et al.[Error! Reference source not found.] Hexagonal CdSe nanodots	Chia.et al.[Error! Reference source not found.] Cubic CdSe thin film	Pengtao Jing et al.[Error! Reference source not found.] CdSe-core CdS/CdZnS/ ZnS-Multi shell QDs	Raino et al. [Error! Reference source not found.] CdSe/CdS Dot-in-Rod	Achtstein et al.[Error! Reference source not found.] Colloidal CdSe nanoshe ets	Ghosh et al.[Error! Reference source not found.] Silver coated CdS QDs	Sumanta et al. [Error! Reference source not found.] Colloidal CdSe Nanoplatelets
		(1997)	(2005)	(2007)	(2007)	(2009)	(2011)	(2012)	(2016)	(2017)
Γ_0	*meV*	10 & 16.5	85.5	79.0	5.5		40	30.4 – 32.5	464	32.5
Γ_{AC}	*μeV /K*	17.6 & 87.8	71	20	84	78.9	5	2.4 - 9.8	48	0.38
Γ_{LO}	*meV*	84.4 & 43.04	21	30	20	48.7	18	13.6 – 17.0	15	236.3
E_{LO}	*meV*	26	24.5	25	49	25	30	25	37.2	25

From Table 3.5., we can see the LO phonon coupling is slightly higher than the results of theoretical calculations by Rudin et al. **Error! Reference source not found.** reporting Γ_{LO} = 18.3 meV for bulk. C hia and co-workers **Error! Reference source not found.** also measured a Γ_{LO} = 20 meV in a bulklike cubic CdSe epilayer. Perna and co-workers**Error! Reference source not found.** report for hexagonal CdSe epilayers on ⟨111⟩ s ilicon a much higher LO phonon coupling of 84 meV and much stronger emission broadening. Achtstein et al.**Error! Reference source not found.** reported Γ_{LO} = 15 meV for 5ML CdSe nanosheet. Recently S umanta Bose et al. **Error! Reference source not found.** reported Γ_{LO} = 236.3 meV and Γ_{AC} = 0.38 meV for CdSe NPLs.

Line width calculations of CdTe nanoplatelets are hardly reported yet but it is interesting to compare our results of Type II transitions with experimental line width calculations of CdTe/(Cd, Zn)Te single quantum wells, colloidal CdTe QDs, hydrothermally synthesized CdTe QDs and CdTe QD monolyers as mentioned in Table 3.6.

Within our measurements we have not only observed a temperature-induced emission shift and broadening, but also a significant reduction of PL emission with increasing temperature. This indicates a thermally activated process being involved in the carrier relaxation.

Table 3.6: Previous findings about line width coefficients of Type II transitions for CdTe NCs

Coefficients of eq. (2)		Rudin et al. **Error! Reference source not found.** Theoretical calculations CdTe	Mayer et al. **Error! Reference source not found.** CdTe/(Cd, Zn)Te single quantum wells	G. Morello et al.**Error! Reference source not found.** Colloidal CdTe QD	Amardeep et al.**Error! Reference source not found.** Hydrothermally synthesized CdTe QDs	Graham .et al. **Error! Reference source not found.** CdTe QD Monolayers
		(1990)	(1995)	(2007)	(2015)	(2016)
Γ_0	*meV*		0.1 – 0.4			
Γ_{AC}	*μeV/K*	0.72	2 – 3.5	14 - 33	4.7 - 51.1	60 - 90
Γ_{LO}	*meV*	24.5	30	14 - 21	8.9 – 20.3	18 - 20
E_{LO}	*meV*	21.1	21	20 - 21	21.1	18 - 20

3.5: Temperature dependence Area

To understand the effect of temperature on the nonradiative process, which affects the relaxation of excited carriers, we investigate the evolution of the PL intensity as a function of temperature in the range of 4–300 K for all the samples.

The Arrhenius Plots (fig. 3.10, 3.11 & 3.12) displays the integrated emission intensities of Type I and Type II transitions (i.e. area). We have a substantial reduction in the PL intensity with increasing temperature. This indicates a thermally activated process being involved in nonradiative carrier recombination. Since nonradiative recombination rates are generally thermally activated, no matter if they are due to excited state depopulation or due to activation of a nonradiative recombination center (e.g., defects).

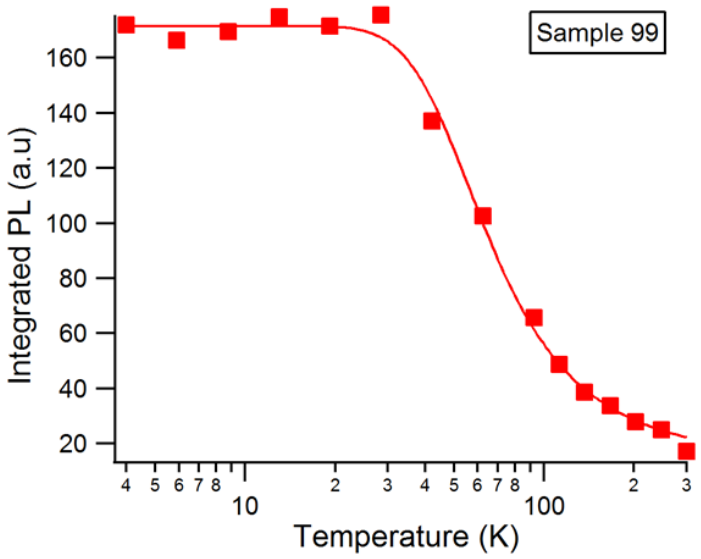

Figure 3. 10. The Arrhenius Plot displays the integrated emission intensity of sample 99

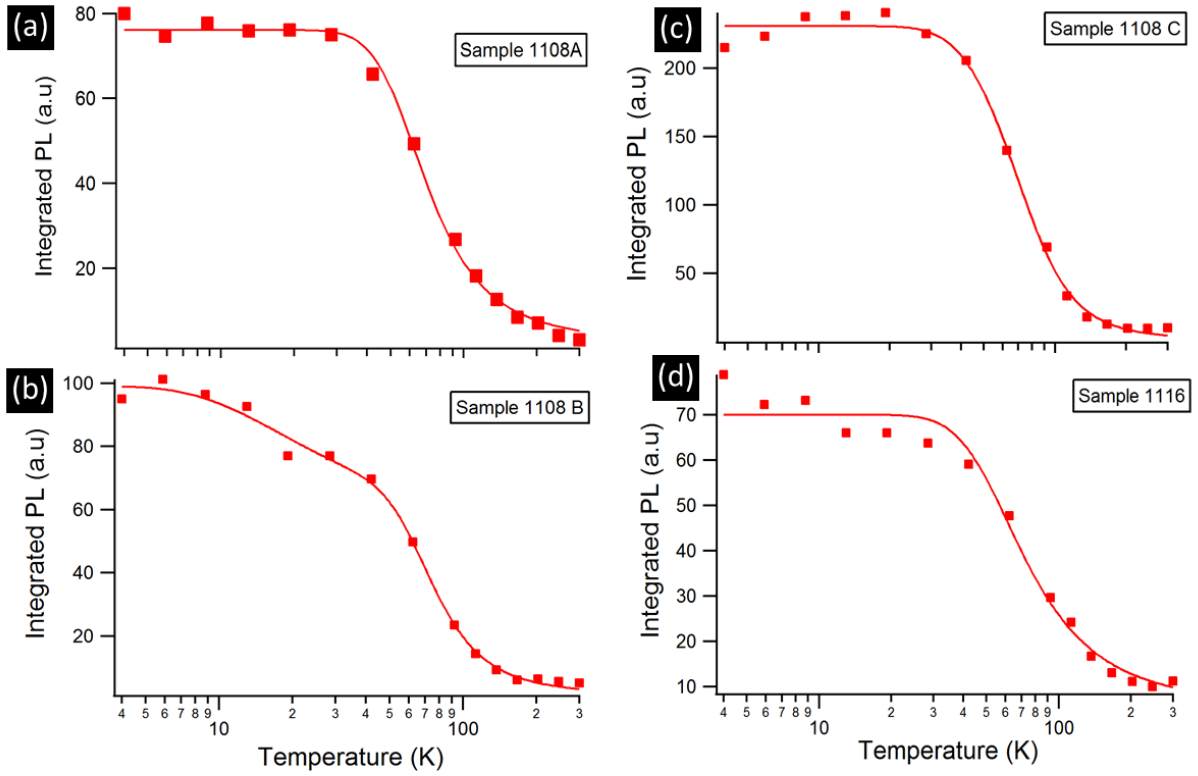

Figure 3. 11. The Arrhenius Plot displays the integrated emission intensities for CdSe core in various aspect ratios of CdSe/CdS/CdTe CBC NPLs.

The PL intensity remain constant until ~ 50 K. In the temperature range 50-100 K, the PL quenching is relatively modest, beyond, which it decreases at a faster rate up to 300 K. This behaviour is same for all samples. To determine the thermal activated energies $\boldsymbol{E_a}$, the integrated PL intensity as a function of temperature is fitted by the following equation.[30]

$$\boldsymbol{I(T) = I_0/\left[1 + Ce^{-E_a/K_BT}\right]} \qquad (3.3)$$

Where *I* (0) and *I* (*T*) are the integrated PL intensities at 0 K and T K, respectively. Here *C* is the ratio of radiative lifetime to the nonradiative lifetimes. $\boldsymbol{E_a}$ is the activation energy of the nonradiative channel. The fitted curves with eq. 3.3 for all the sample are shown in Fig. 3.10, 3.11 & 3.12 for both Type I and Type II transitions.

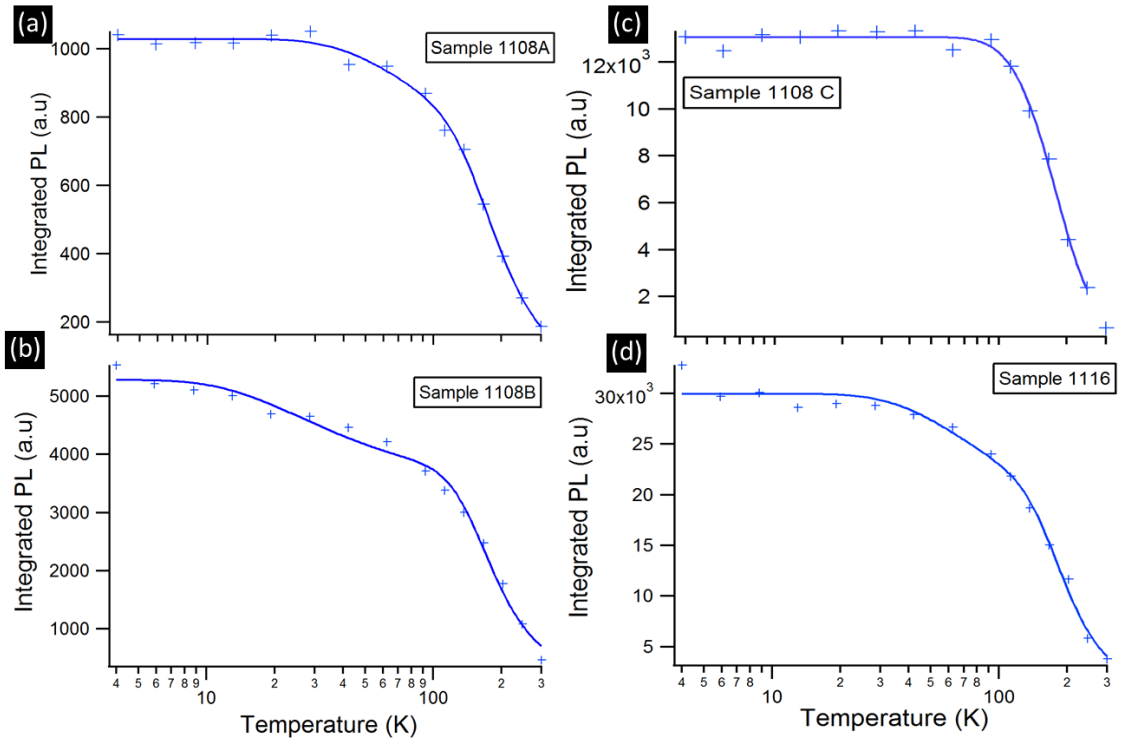

Figure 3. 12. Integrated PL intensity as a function of temperature for CdSe/CdS/CdTe CBC NPLs of various aspect ratios.

We used mostly two-component fit of eq. 3.3, while some samples are fitted with a single component fit. The best-fitted parameters for all samples are shown in Table. 3.7. Thermal activation energies obtained in our samples for type II transitions are approximately between 64–77 meV which are quite large compared to type I transitions i.e. between 15–33 meV as mentioned in Table 3.7.

Table 3.7 Results of the fits from the data of Figure 3.10-12 by using eq 3.3.

Type I			Type II		
I (0) (eV)	C (eV)	Ea (meV)	I (0) (eV)	C (eV)	Ea (meV)
171.58 ± 1.79	12.01 ± 1.26	15.17	29968 ± 53	116.28 ± 98.1	77.58 ± 16.9
87.31 ± 14.4	18.716 ± 3.52	20.091 ± 1.38		0.87 ± 0.47	9.52 ± 3.9
	0.4411 ± 0.2	0.4663 ± 0.36	1028.8 ± 9.46	49.84 ± 19	64.75 ± 8.3
76.85 ± 0.621	64.45 ± 22.8	33.606 ± 6.09		0.7 ± 0.332	10.4 ± 3.3
	3.85 ± 3.1	11.584 ± 2.97	13005 ± 12	105.9 ± 36.8	70.35 ± 5.3
229.08 ±3.3	67.24 ± 20.6	25.007 ± 2.07	5277.3 ± 11	0.54 ± 0.11	3.0512 ± 0.9
98.969 ± 2.31	0.75 ± 0.19	22.313 ± 0.64		77.1 ± 41.8	65.86 ± 9.67
	85.2 ± 32.5	27.65 ± 3.31			

This confirms that the initial slow decrease in PL intensity with an increase in temperature up to 100 K is due to the trapping of carriers in the surface/interface defect states of CdTe. A deeper understanding of the chemical origin of these trap states and their effects on carrier dynamics is an ongoing intense research and debate topic.[33, 34]. Above 100 K, PL quenching is relatively fast, which limits the quantum efficiency of these CBC NPLs at high temperature. In conclusion, we can say that PL intensity in Type I decreases rapidly while in Type-II is more stable. It is interesting to compare our results with early reported values. Table. 3.8 shows the previously reported activation energies E_a fitted with eq. 3.3 for different nanocrystals.

Table 3.8 Results of previously reported activation energies E_a for different nanocrystals.

Author	Year	Material	Coefficient of eq. (3) E_a (meV)
Velerini et al.[20]	2005	CdSe/ZnS core/shell QDs	15
G. Morello et al.[28]	2007	CdTe QDs	13.6 – 23.5
Chia.et al.[18]	2007	Cubic CdSe thin film	16
D.KIM et al.[32]	2008	CdS QDs	100
Pengtao Jin et al.[25]	2009	CdSe/CdS/CdZnS/ZnS-Multi shell QDs	26.5
Achtstein et al.[12]	2012	Colloidal CdSe nanosheets	3.8 – 4.7
Amardeep et al.[29]	2015	Hydrothermally synthesized CdTe QDs	18.6-45.4
Ghosh et al.[26]	2016	Silver coated CdS QDs	20
Graham .et al. [31]	2016	CdTe QD Monolayers	37-52
Riccardo Scott et al.[34]	2016	CdSe-CdTe and CdTe-CdSe type II hetero NPs	16 CdSe core, 50 CdSe/CdTe, 31 CdTe/CdSe
Sumanta et al.[13]	2017	Colloidal CdSe Nanoplatelets	494

3.6: TCSPC measurements

To gain more insight into underlying decay process, we performed time-resolved PL experiments as a function of temperature ranging from 4K to 300K using an Edinburgh Instruments FLS920 spectrofluorometer. Figure 3.13 to fig. 3.17 shows the 3D plots of CdSe/CdS and CdSe/CdS/CdTe photoluminescence and their corresponding PL decays. These traces are fitted by multi exponential decay functions with the average lifetimes of 8.8 ns for CdSe/CdS NPLs (Type-I transition) and 250 ns for CdSe/CdS/CdTe NPLs (type-II transition). In the former case PL lifetimes are changing continuously at elevated temperature while in the later case PL lifetimes are satble, see table 3.9 and 3.10 for further details. So in general, the PL decay of CdSe/CdS is strongly temperature dependent while the PL decay of CdSe/CdS/CdTe is almost temperature-independent.

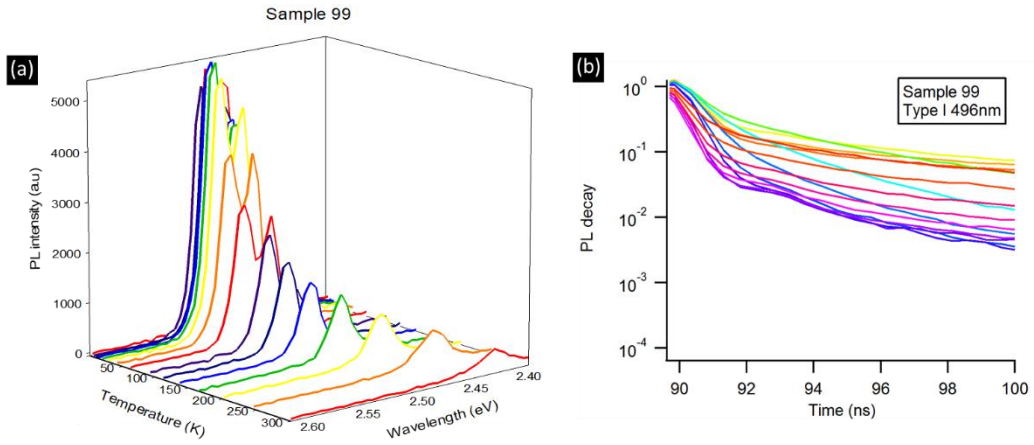

Figure 3. 13. PL and PL decays of CdSe/CdS NPLs as a function of temperature in (a) and (b) respectively.

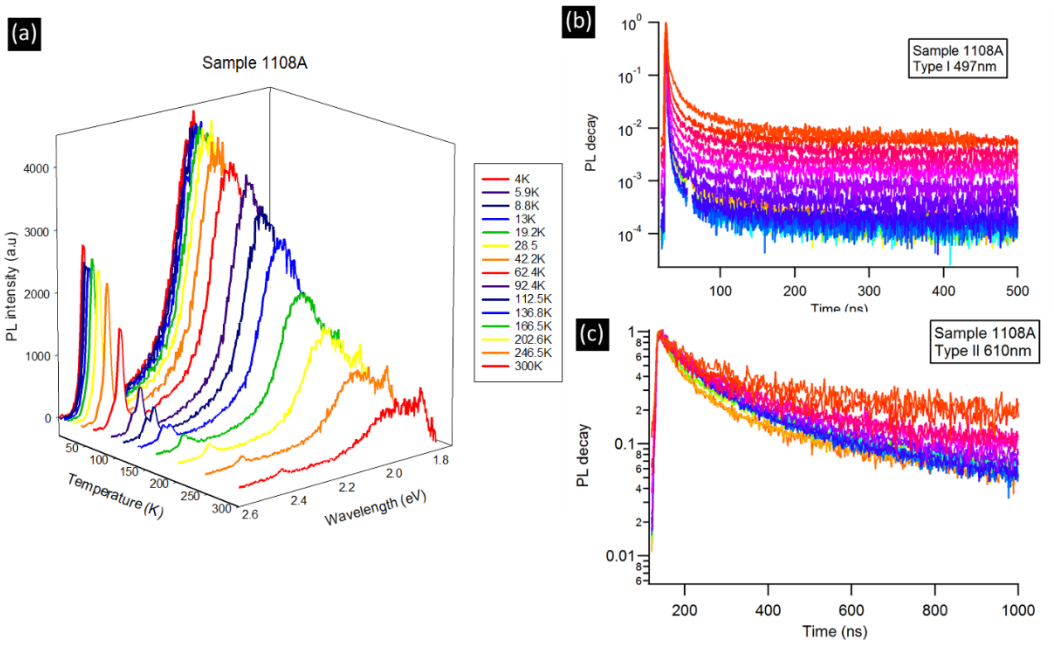

Figure 3. 14. PL and PL decays of CdSe/CdS/CdTe CBC NPLs with aspect ratio of 4 as a function of temperature in (a) and (b) respectively.

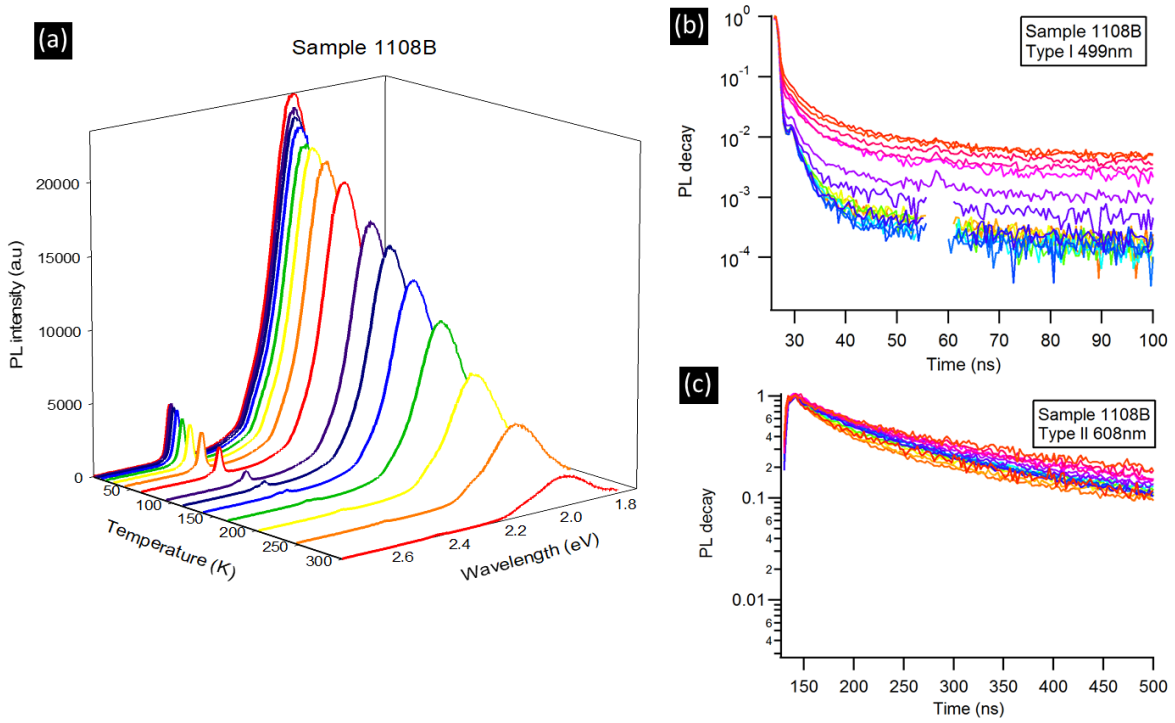

Figure 3. 15. PL and PL decays of CdSe/CdS/CdTe CBC NPLs with aspect ratio of 3.8 as a function of temperature in (a) and (b) respectively.

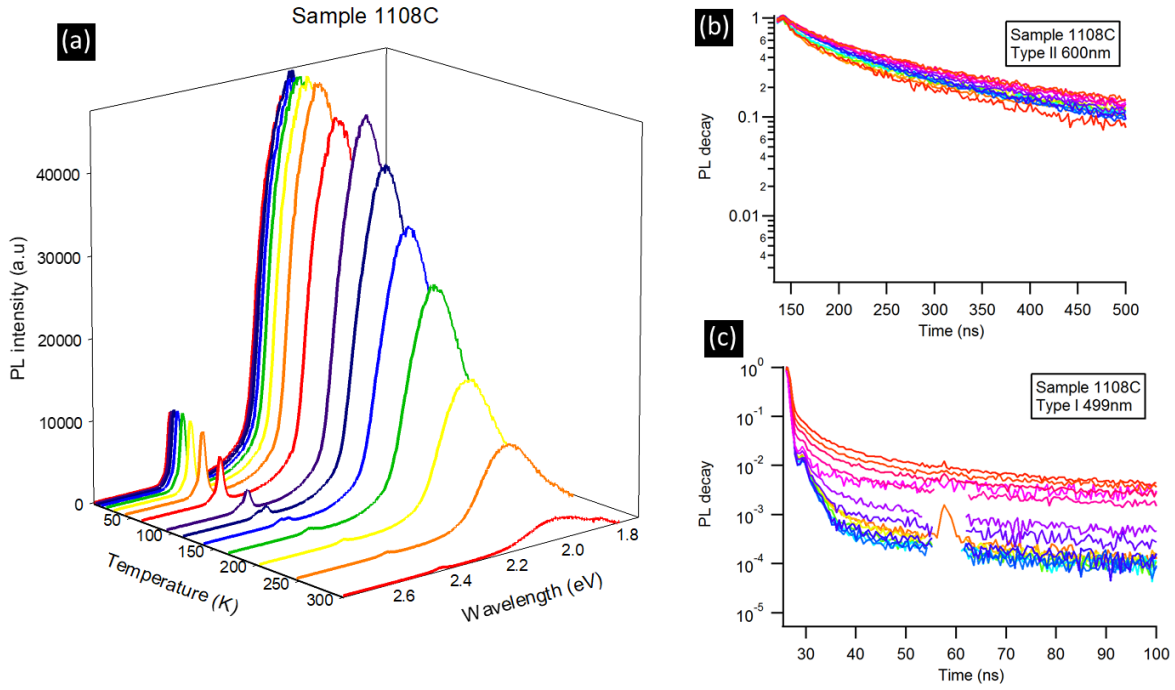

Figure 3. 16. PL and PL decays of CdSe/CdS/CdTe CBC NPLs with aspect ratio of 3.4 as a function of temperature in (a) and (b) respectively.

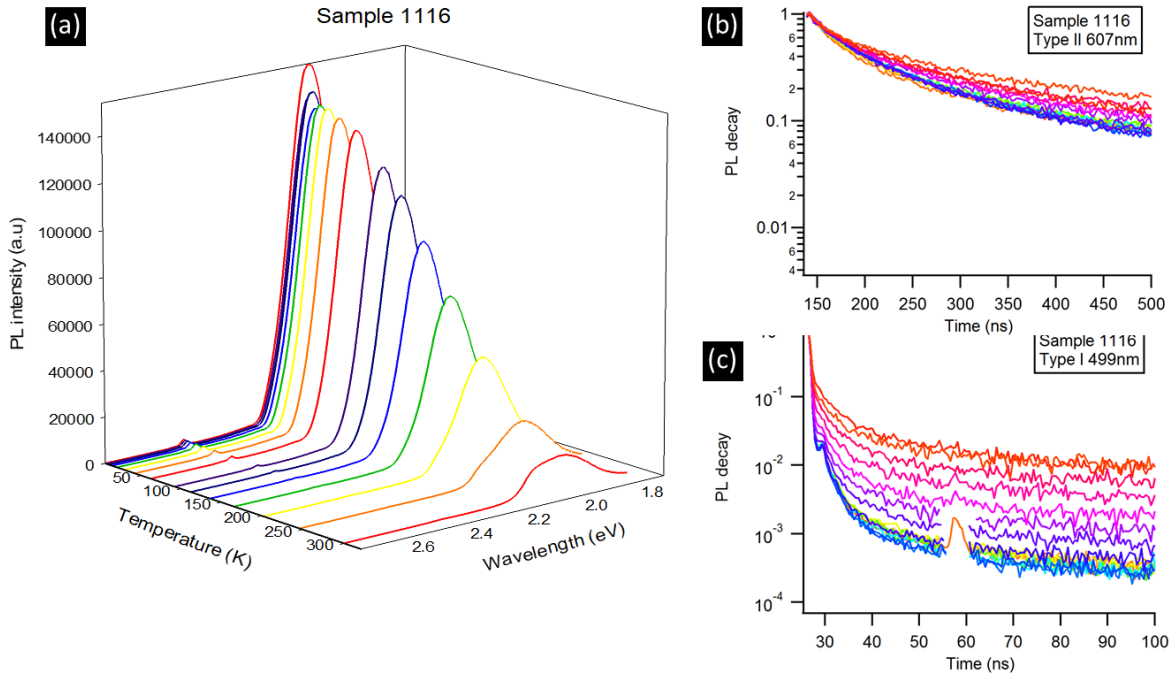

Figure 3. 17. PL and PL decays of CdSe/CdS/CdTe CBC NPLs with aspect ratio of 3.3 as a function of te mperature in (a) and (b) respectively.

Table 3.9 PL decays of Type-I transition measured for CdSe/CdS NPLs.

Temperature (K)	Sample 1108A (at λ = 610nm)	Sample1108B (at λ = 608nm)	Sample 1108C (at λ = 600nm)	Sample 1116 (at λ = 607nm)
4	416.2	94.1	264.9	227.3
6	365.8	99.8	239.3	273.9
9	437.9	108.8	275.4	262.2
13	434.3	103.6	210.9	242.6
19	400.3	112.1	216.9	184.2
29	336.6	108.2	264.9	205.9
42	319.2	104.3	241.7	223.7
62	346.9	104.4	244.5	199.7
92	435.0	126.9	218.7	216.2
113	417.9	133.1	249.3	228.1
137	504.2	128.8	276.4	262.7
167	470.6	132.4	288.5	311.7
203	394.0	134.4	266.3	325.5
247	421.0	160.1	273.2	346.4
300	416.2	97.4	153.4	242.7

Table 3.10. PL decays of Type-II transition measured for CdSe/CdS/CdTe NPLs.

Temperature (K)	Sample 99 (at λ = 496nm)	Sample 1108A (at λ = 497nm)	Sample1108B (at λ = 499nm)	Sample 1108C (at λ = 499nm)	Sample 1116 (at λ = 499nm)
4	32.4	3.3	0.7	3.4	14.8
6	29.5	3.5	3.7	3.0	14.6
9	15.1	2.9	1.7	3.4	9.9
13	6.8	2.0	3.8	2.8	15.2
19	5.2	0.2	3.3	3.5	5.6
29	1.8	0.6	0.9	0.8	10.4
42	0.8	0.7	2.1	2.6	5.7
62	0.7	0.4	3.7	3.6	9.9
92	1.5	2.3	5.7	7.1	20.9
113	5.2	2.9	5.9	6.2	40.5
137	5.4	3.1	9.2	7.6	45.6
167	6.9	3.8	11.0	12.5	31.4
203	8.7	5.3	9.3	11.7	30.4
247	6.2	5.2	7.9	12.7	23.5
300	6.3	4.3	7.2	16.6	24.7

Temperature sensing is an important application for industries like petrochemical, automotive, aerospace and defense, consumer electronics, and so on. Ratiometric methods are based on the use of a ratio between two fluorescence intensities. Temperature sensors in principal depend on the changes in the luminescence intensity that usually diminished with increase in temperature. In micro devices, it's very difficult to control the changes occur in the sensor local environment and as a result we have inaccurate temperature measurements. To overcome such problems we can use ratiometric detection schemes.

3.7: Conclusion

In dual-emitting sensors, we have resolvable luminescence from two different excited states. When temperature varies one or both of these PL intensities, its effect is measurable from relative instead of absolute PL intensities, reducing the impact of extrinsic factors like fluctuations in excitation rate, detection efficiency, probe concentration, optical occlusion, or other local inhomogeneities that alter absolute intensities. Here, we propose to use the dual emission from CdSe/CdS NPL for optical thermometry. These NPL can be used a temperature-sensitive materials because their photo emission intensities are temperature dependent. Furthermore, we observed that the PL decay of CdSe/CdS is strongly temperature dependent while the PL decay of CdSe/CdS/CdTe is almost temperature-independent.

3.8: References

1. *C.R. Kagan,* C.B. Murray, M. Nirmal and M.G. Bawendi, Phys. Rev. Lett. 76, 1517 (1996).
2. C.R. Kagan, C.B. Murray and M.G. Bawendi, Phys. Rev. B-Condensed Matter 54, 8633 (1996).
3. D.M. Willard, L.L. Carillo, J. Jung and A. Van Orden, Nano Lett. 1, 469 (2001).
4. S.P. Wang, N. Mamedova, N.A. Kotov, W. Chen and J. Studer, Nano Lett. 2, 817 (2002).
5. S. Ithurria and B. Dubertret, J. Am. Chem. Soc., 2008, 130, 16504.
6. B. Guzelturk, Y. Kelestemur, M. Olutas, S. Delikanli and H. V. Demir, ACS Nano, 2014, 8, 6599.
7. Z. Chen, B. Nadal, B. Mahler, H. Aubin and B. Dubertret, Adv. Funct. Mater., 2014, 24, 295–302.
8. S. Ithurria, M. D. Tessier, B. Mahler, R. P. Lobo, B. Dubertret and A. L. Efros, Nat. Mater., 2011, 10, 936.
9. Tessier, Mickaël D., Piernicola Spinicelli, Dorian Dupont, Gilles Patriarche, Sandrine Ithurria, and Benoit Dubertret., 2013 Nano letters 14, 207-213.
10. Pedetti, S., Ithurria, S., Heuclin, H., Patriarche, G., & Dubertret, B. J. Am. Chem. Soc., . (2014) 136(46), 16430-16438.
11. Achtstein, Alexander W., Anatol V. Prudnikau, Maxim V. Ermolenko, Leonid I. Gurinovich, Sergey V. Gaponenko, Ulrike Woggon, Alexander V. Baranov et al. ACS nano 8, no. 8 (2014): 7678-7686.
12. Achtstein, Alexander W., Andrei Schliwa, Anatol Prudnikau, Marya Hardzei, Mikhail V. Artemyev, Christian Thomsen, and Ulrike Woggon. Nano letters 12, no. 6 (2012): 3151-3157.
13. Bose, Sumanta, Sushant Shendre, Zhigang Song, Vijay Kumar Sharma, Dao Hua Zhang, Cuong Dang, Weijun Fan, and Hilmi Volkan Demir. Nanoscale9, no. 19 (2017): 6595-6605.
14. *X. Wen, A. Sitt, P. Yu, Y. R. Toha and J. Tang, Phys. Chem. Chem. Phys., 2012, 14, 3505.*
15. Logothetidis, S.; Cardona, M.; Lautenschlager, P.; Garriga, M. Phys. Rev. B 1986, 34,2458.
16. Lautenschlager, P.; Garriga, M.; Logothetidis, S.; Cardona, M. Phys. Rev. B 1987, 35,9174.
17. ÓDonnell, K. P.; Chen, X. Appl. Phys. Lett. 1991, 58, 2924.
18. Chia, C. H.; Yuan, C. T.; Ku, J. T.; Yang, S. L.; Chou, W. C.; Juang, J. Y.; Hsieh, S. Y.; Chiu, K. C.; Hsu, J. S.; Jeng, S. Y. J. Lumin. 2008, 128, 123.
19. Logothetidis, S.; Cardona, M.; Lautenschlager, P.; Garriga, M. Phys. Rev. B 1986, 34, 2458

20. D. Valerini, A. Cretí, M. Lomascolo, L. Manna, R. Cingolani and M. Anni, Phys. Rev. B, 2005, 71, 235409
21. S. Rudin, T. L. Reinecke and B. Segall, Phys. Rev. B, 1990, 42, 11218–11231
22. G. Perna, V. Capozzi and M. Ambrico, J. Appl. Phys., 1998, 83, 3337–3344.
23. Mayer, E. J., N. T. Pelekanos, J. Kuhl, N. Magnea, and H. Mariette. Physical Review B 51, no. 23 (1995): 17263.
24. Al Salman, A., A. Tortschanoff, M. B. Mohamed, D. Tonti, F. Van Mourik, and M. Chergui. Applied Physics Letters 90, no. 9 (2007): 093104.
25. Jing, Pengtao, Jinju Zheng, Micho Ikezawa, Xueyan Liu, Shaozhe Lv, Xianggui Kong, Jialong Zhao, and Yasuaki Masumoto, The Journal of Physical Chemistry C 113, no. 31 (2009): 13545-13550.
26. Ghosh, P., D. Kushavah, P. K. Mohapatra, P. Vasa, K. C. Rustagi, and B. P. Singh. arXiv preprint arXiv:1606. 06711 (2016).
27. Rainò, Gabriele, Thilo Stöferle, Iwan Moreels, Raquel Gomes, John S. Kamal, Zeger Hens, and Rainer F. Mahrt. ACS nano 5, no. 5 (2011): 4031-4036.
28. Morello, G., M. De Giorgi, S. Kudera, L. Manna, R. Cingolani, and M. Anni. The Journal of Physical Chemistry C 111, no. 16 (2007): 5846-5849.
29. Jagtap, Amardeep M., Jayakrishna Khatei, and KSR Koteswara Rao. Physical Chemistry Chemical Physics 17, no. 41 (2015): 27579-27587.
30. Murphy, Graham P., Xia Zhang, and A. Louise Bradley. The Journal of Physical Chemistry C 120, no. 46 (2016): 26490-26497.
31. Leroux, M.; Grandjaean, M.; Beumont, B.; Nataf, G.; Semond, F.; Massies, J.; Gibart, P. J. Appl. Phys. 1999, 86, 3721.
32. F. M. G. Campos and M. Califano, Nano Lett., 2012, 12, 4508.
33. M. Kapitonov, A. P. Stupak, S. V. Gaponenko, E. P. Petrov, A. L. Rogach and A. Eychmu¨ller, J. Phys. Chem. B, 1999, 103, 10109.
34. T. Takagahara, Phys. Rev. Lett., 1993, 71, 3577–3580
35. Kim, D., T. Mishima, K. Tomihira, and M. Nakayama. The Journal of Physical Chemistry C 112, no. 29 (2008): 10668-10673.
36. Scott, Riccardo, Sebastian Kickhöfel, Oliver Schoeps, Artsiom Antanovich, Anatol Prudnikau, Andrey Chuvilin, Ulrike Woggon, Mikhail Artemyev, and Alexander W. Achtstein. Physical Chemistry Chemical Physics 18, no. 4 (2016): 3197-3203.

Chapter 4. Composition and Surface Functionalization dependent Optical Properties of Lead Halide Perovskite Nanocrystals

ABSTRACT: The optical properties of lead halide perovskite nanocrystals (LHP NCs) depend strongly on their composition and surface passivation. Here we present a detailed study on the temperature dependent photoluminescence (PL) and PL decay dynamics of LHP NCs varying the type of A site cation, the surface ligands, and the NC size. Throughout, for all A cation types and different surface functionalization's and different NC sizes we observe a single emission peak in the range from cryogenic to ambient temperature if the colloidal dispersion shows good monodispersity. Therefore, the possible occurrence of multiple peaks in emission spectra, as reported in literature, can be attributed to the presence of different NC populations in the sample under investigation. The PL decay dynamics are dominated by the surface passivation, and a post synthesis ligand exchange from mixed ligands (oleylamine and oleic acid) to quaternary amines results in a more stable passivation over a more extended temperature range. Concerning the PL peak position at low temperatures, the redshift with decreasing temperature that is commonly observed for these materials (that is related to bulk properties) becomes size-dependent. As a result, smaller NCs show a significantly reduced PL shift with temperature. Our findings are corroborated by temperature dependent XRD experiments that confirm the orthorhombic phase of the $CsPbBr_3$ NCs throughout the full temperature range and rule out the possibility of any phase related secondary emission.

The results discuss in this chapter have been reported in "Ijaz, P. et al. Composition, Size, and Surface Functionalization Dependent Optical Properties of Lead Bromide Perovskite Nanocrystals. *J. Phys. Chem. Lett.* 2020, 11, XXX, 2079-2085.

4.1. Introduction

Optical properties of colloidal semiconductor nanocrystals (NCs) have been widely investigated for the last three decades. It has been well established that the composition as well as nature of the nanocrystal surface strongly influence their optical properties.[1-3] Recently, lead halide perovskite NCs (LHP-NCs), with composition $APbX_3$ (with A being a monovalent cation and X being either Cl, Br, or I), have emerged as a promising material due to their ease of preparation, broadly tunable band gap, high photoluminescence quantum yield (PLQY) and excellent color purity.[4-6] This remarkable set of properties makes them ideal candidates for light emission technologies, such as light emitting diodes, lasers and single photon emitters.[7-9] Significant progress has been made on the synthesis of LHP-NCs, especially with regard to size, shape, composition control, and by tailoring the surface passivation through direct synthesis or post-synthesis ligand exchange.[4] The advancements on synthesis of LHP not only paved the way to investigate shape and composition dependent optical properties, but also offered a great opportunity to investigate their surface functionalization-dependent optical properties. In particular, photoluminescence (PL) spectroscopy at cryogenic temperatures has been widely used to investigate the temperature-dependent excitonic properties of traditional semiconductors and recently of LHP-NCs.[10-13] In particular, there has been some dissense in the literature reports on whether lead halide nanocrystals undergo temperature-induced phase transitions (from room temperature towards cryogenic temperatures), and whether the emission at cryogenic temperatures consists of single or multiple peaks.[12,14,15] For instance, Li et al. studied temperature dependent optical properties of $CsPbBr_3$ NCs with different sizes.[12] and found that $CsPbBr_3$ NCs with intermediate size manifest a blue shifted dual emission around 80K while further smaller or bigger NCs show a single blue shifted emission peak at this temperature. Contrary to this, Lee et al. reported dual emission for 11nm size $CsPbBr_3$ NCs for the same range of temperature.[14] Later on Shinde et al. carried out temperature dependent optical spectroscopy of 3 different sizes (5.5, 7.3 and 10.1 nm) of $CsPbBr_3$ NCs.[15] They observed size dependent emission peaks (smaller the size of the NCs leads to larger number of emissions) at 10 K and this was attributed to the degree of quantum confinement in $CsPbBr_3$ NCs. Similarly Laru et. al. reported that the distortion in the orthorhombic phase of $CsPbBr_3$ NCs at low temperature leads to distinct carrier-phonon coupling which

consequently results in multiple emissions.[16] Recently, Drioll et al. investigated the low temperature absorption, PL and lifetimes dynamics of 15nm size $CsPbBr_3$ NCs and observed single narrow red shifted emission at 3K.[17]

From a surface chemistry point of view, the first generation of LHP NCs were typically prepared by using primary alkyl amines and alkyl carboxylates as a surfactants, and it has been well established that both ligands are present on the surface of the NCs, bound as alkyl carboxylate/alky ammonium ligand pairs (henceforth referred to as "mixed ligands capped NCs").[16-19] Substantial advances in colloidal syntheses over past few years have provided the opportunity to prepare LHPs NCs with diverse surface coatings, leading to tailored properties, such as improved colloidal stability and near-unity PLQY.[20,21] However, investigations based on optical spectroscopy were mainly limited to the first generation of NCs with the mixed ligands surface passivation. Considering the recent developments in surface functionalization, a temperature dependent optical spectroscopy study of trap free, near unity PLQY NCs is therefore appealing to understand their excitonic properties.

In this project, we study the photoluminescence properties of $APbBr_3$ (A=Cs, MA, FA) perovskite nanocrystals with respect to temperature, nanocrystal size, and surface passivating ligands. Throughout, all samples manifest a single narrow emission peak at room and cryogenic temperature. Here the PL intensity is strongest in an intermediate temperature regime that spans from around 50 K to 250 K, while the PL life time decreases with decreasing temperature in the range from RT to around 50 K. $CsPbBr_3$ nanocrystals with different size manifest quantum confinement effects, but we do not observe any significant impact of their size on the spectral shape of the emission and on their life time dynamics. On the contrary, the surface passivation affects the temperature dependence of the PL and the PL lifetime. Here, exchanging the ligands from oleylamine and oleic acid, or Cs-oleate, by a post-synthesis ligand exchange to quaternary amines such as didodecyldimethlammonium bromide (QAB) results in higher PL intensity over an extended temperature range from 20 K to 280 K. At the same time, the PL decay dynamics are notably different for QAB ligands, showing a monoexponential decay over a large temperature range, while oleylammonium oleate and Cs-oleate capped LHPNCs manifest multiexponential decays, where the fast component becomes more dominant with decreasing temperature.

4.2 Synthesis of lead halide perovskite NCs

Synthesis of lead halide perovskite have been described in detail in materials and methods section of chapter 2. Briefly, first generation of $APbBr_3$ NCs were prepared using typical ligands such as oleic acid and oleylamine following a previously reported procedure.[1] Briefly, 76 mg of lead (II) acetate trihydrate, 16 mg of cesium carbonate, 0.3 mL of oleic acid, 1.0 mL of oleylamine and 10 ml of ODE were combined in a 25 ml 3-neck flask equipped with a thermocouple and a magnetic stirrer. The reaction mixture was degassed for 5 minutes at room temperature and then for one hour at 120 °C. Next, the temperature was increased to 175 ^{o}C and a solution of benzoyl bromide (70 µL) in ODE (500 µL, which had previously been degassed for an hour at 120 °C and stored in glove box) was swiftly injected. The reaction mixture was immediately cooled down using an ice-water bath. Thereafter, 5 mL of toluene was added to the crude solution, then it was centrifuged at 5000 rpm for 10 minutes. The supernatant was discarded, and the precipitate was redispersed in 5 mL of toluene. Cs-oleate capped $CsPbBr_3$ NCs were synthesized following our previously reported procedure using standard Schlenk line techniques.[2] Briefly, lead (II) acetate trihydrate (76 mg) caesium carbonate (16 mg) and octadecene (10 ml) were combined in a 25 ml 3-neck flask equipped with a thermocouple and a magnetic stirrer. The reaction mixture was degassed for 5 minutes at room temperature and then for one hour at 115 °C. Then, a ligand mixture containing oleic acid (1.5 mL, previously degassed for an hour at 120 °C and stored in glove box), didodecylamine (1.25 mmol, 443 mg) dissolved in 1 mL of anhydrous toluene was rapidly injected under nitrogen. After the complete dissolution of the metal precursors, the temperature was decreased to 70 °C and a solution of benzoyl bromide (50 µL) in anyhydrous toluene (500 µL) was swiftly injected. After 60 seconds, the reaction mixture was cooled down by using a water bath. Then 20 mL of an ethyl acetae and toluene mixture (with a ratio of 6:1) was added into the crude solution to destabilize the colloids followed by centrifugation at 6000 rpm for 10 min. Finally, the supernatant was discarded, and the precipitate was redispersed in toluene. QAB capped $CsPbBr_3$ NCs were prepared following a previously reported ligand exchange strategy.[3] Briefly, Cs-oleate capped NCs were prepared following above mentioned procedure[2] and the crude reaction mixture containing the $CsPbBr_3$ NCs (3 mL) were treated with an anhydrous toluene solution containing the ammonium bromide salt (2 mL, 0.025M) and the mixture was vigorously stirred for 1 minute. Thereafter, the NCs were

washed by addition of 15 mL of ethyl acetate followed by centrifugation at 6000 rpm for 10 minutes and re-dispersion in toluene.

4.3 Results and Discussion

Transmission electron microscope (TEM) images of $CsPbBr_3$, $MAPbBr_3$ and $FAPbBr_3$ are reported in Figure 4.1 a-c, demonstrating that the NCs are nearly monodisperse with cubic shape in all cases. Typical UV-Vis optical absorption and PL spectra, measured in toluene dispersions, are reported in Figure 4.1 d, manifesting a single emission peak that is red-shifted from the absorption edge. For the temperature-dependent spectroscopy, we fabricated NC films on sapphire substrates by drop-casting the colloidal dispersions.

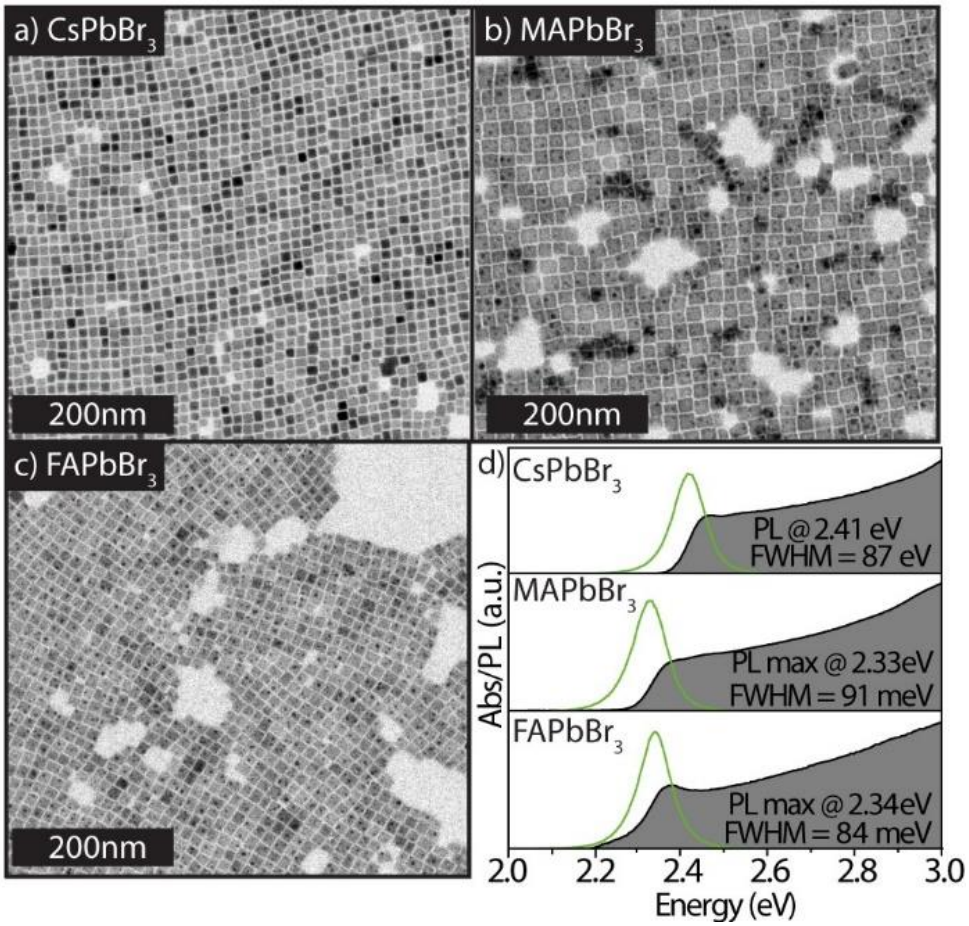

Figure 4. 1. $APbBr_3$ NCs prepared by using oleylamine and oleic acid as surfactants, hence having a mixed ligands passivation of oleylammonium oleate (A=Cs, MA, FA). TEM images of $CsPbBr_3$ (a), $MAPbBr_3$ (b), and $FAPbBr_3$ NCs (c). The mean values of the edge lengths of the NCs in (a), (b) and (c) are $9.2 \pm \mathbf{0.8}$, $17.3 \pm \mathbf{1.6}$, $12.9 \pm \mathbf{1.4}$ nm, respectively. Absorbance and PL spectra of the corresponding NC samples in toluene dispersions (d).

4.3.1. Temperature dependent optical properties of APbBr3 NCs

The NC films were cooled to 4 K and then the temperature was stepwise increased from 4 K to 300 K to acquire the PL and PL lifetime spectra. PL spectra of $APbBr_3$ NCs with different A site cations such as cesium (Cs), methylammonium (MA) and formamidinium (FA) passivated by oleylammonium oleate ligands were recorded from 4 K to 300 K are reported in Figure 4.2. Representative PL spectra measured at 4 K and 300 K are reported in figure 4.3 (a). At low temperature the PL peak energy is red- shifted by 70, 110 and 80 meV for Cs-, MA- and FA-based perovskite NCs with respect to RT, respectively. Such red-shift with decreasing temperature is commonly observed in lead halide perovskites, and is attributed to a thermal expansion of the crystal lattice that reduces the overlap between antibonding orbitals of Pb-6s and Br-4p, which leads to an increase of the band gap. [13,23,24] The $MAPbBr_3$ NCs manifest the strongest temperature related shift in PL peak energy, which can be ascribed to the larger NC size. The temperature-dependent PL spectra, the PL peak energy and linewidth, and the average PL decay times are reported in Figures 4.4 a-f for all three perovskite NC structures.

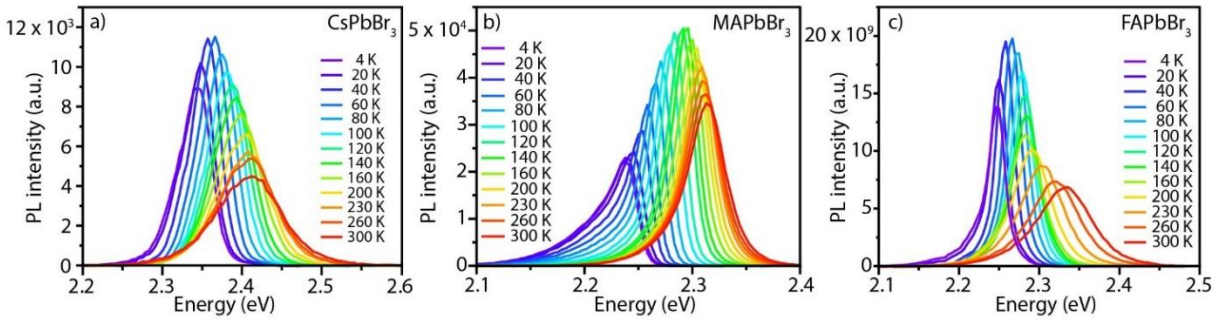

Figure 4. 2. PL spectra measured from 4 K to 300 K for drop casted films of mixed ligands capped $CsPbBr_3$ NCs (a), $MAPbBr_3$ NCs (b) and $FAPbBr_3$ NCs (c).

The PL intensity versus temperature is plotted in Fig. 4.3 b. For all cations, the PL intensity is highest at intermediate temperature from around 70-250 K and decreases towards 4K and room temperature. The $CsPbBr_3$ NCs manifest two plateaus in PL intensity, one from 30-170K, and then from 200-260 K. Instead, the perovskite nanocrystal with organic cation (MA, FA) show a single high-PL-intensity range from around 70-220K. The PL decay traces recorded at different temperatures are reported in Fig. 4.3 c. At room temperature the PL decay is almost monoexponential, and then develops with decreasing temperature into a multiexponential trace with fast and a slow components. Here the dominant slow life time component remains in the range of the life time at room temperature, while the fast component decreases

continuously with decreasing temperature. Relating this behavior to the temperature dependence of the PL intensity, it points to competing processes that enhance both the radiative and non-radiative rates for the initial decrease in temperature from RT to the intermediate range. For temperatures below 70K the drop in PL intensity indicates that the non-radiative rates dominate. Here we can assume that the ammonium and Cs-oleate molecules are immobilized at such low temperatures, which severely hinders the dynamic passivation of the surface states by these mixed ligands.

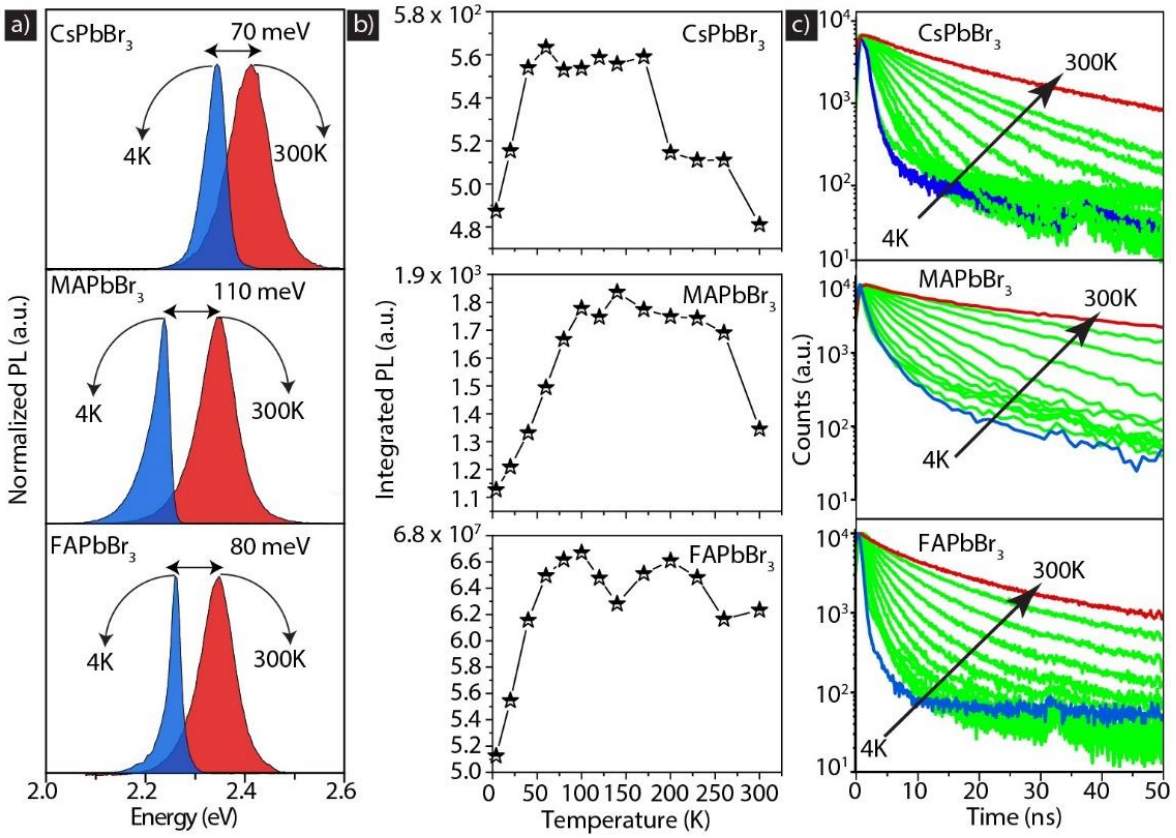

Figure 4. 3. (a) Representative PL spectra recorded from mixed ligand capped $CsPbBr_3$, $MAPbBr_3$ and $FAPbBr_3$ NC films at 4 K and 300 K. (b) Integrated PL intensity as function of temperature for $CsPbBr_3$ $MAPbBr_3$ and $FAPbBr_3$ NCs versus temperature. (c) PL decay traces for different recorded at temperatures for $CsPbBr_3$, $MAPbBr_3$, and $FAPbBr_3$ NCs.

4.3.2. Size and surface dependent optical properties of $CsPbBr_3$ NCs

The emission properties of a film of perovskite nanocrystals can be expected to depend on the size dispersion of the sample, on the surface chemistry, and on the presence of possible side products in the film that stem from the synthesis protocol. To investigate the dependence of the PL on the nanocrystal size we have fabricated two $CsPbBr_3$ samples with markedly different edge length of 9.5 nm and 6.4 nm by our previously reported secondary

amine based synthesis procedure (see experimental section chapter 2 for more details).[22] Remarkably, secondary amines in the form of protonated ammonium ions are not able to bind to the surface of $CsPbBr_3$ NCs nearly as effectively as oleylamine (or as effectively as a primary amine in general). Hence, they do not compete effectively with oleate molecules for binding to the surface of the NCs, and this inhibits the growth of NPLs under any of the conditions tested: different temperatures, ligand concentrations and lengths of the amines' aliphatic chains. In our NCs, the surface coverage (6-8%) by secondary ammonium ions is much lower than that of oleate molecules (92-94%), as is supported by nuclear magnetic resonance (NMR) measurements and X-ray photoelectron spectroscopy (XPS). Density Functional Theory (DFT) calculations further confirm that dialkylammonium molecules cannot stabilize lamellar 2D perovskites, therefore they do not promote an anisotropic growth of NPLs. Furthermore, the NC surface is solely passivated with Cs-oleate. TEM images of the Cs-oleate capped $CsPbBr_3$ NCs are shown in Figure 4.5 a, b.

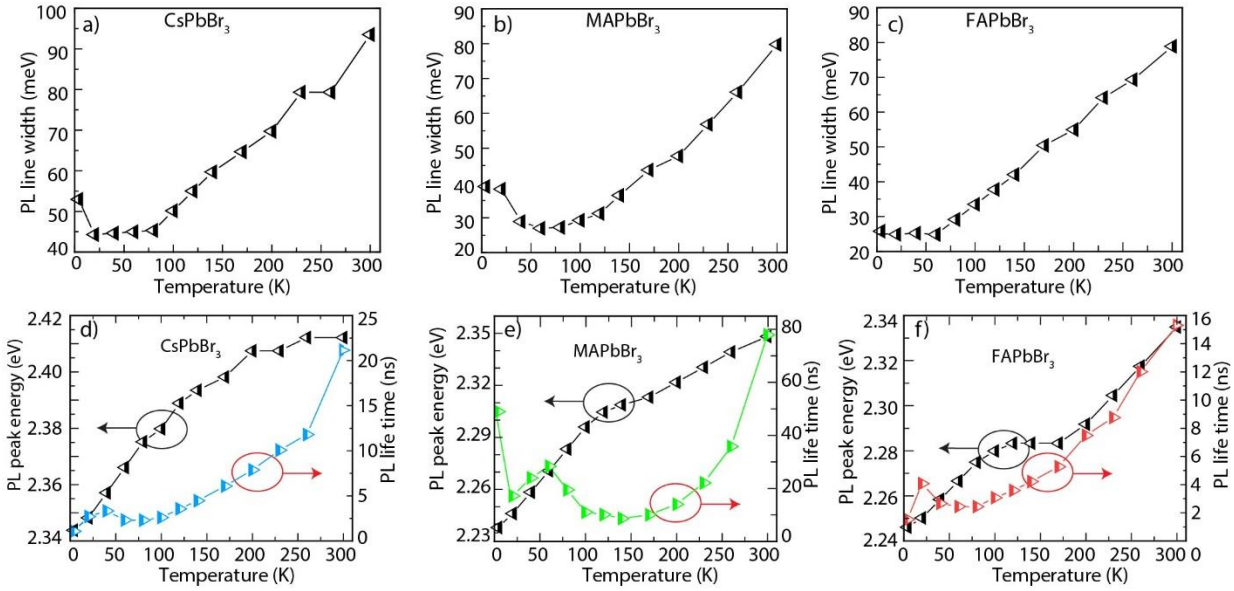

Figure 4. 4. Evolution of PL line width as a function of temperature for mixed ligand capped (a) $CsPbBr_3$, (b) $MAPbBr_3$ and (c) $FAPbBr_3$ NC films. PL peak energy and PL lifetimes at elevated temperatures for mixed ligand capped (d) $CsPbBr_3$, (e) $MAPbBr_3$ and (f) $FAPbBr_3$ NC films.

Table 4.1. Tabular data from figure 4.4: Average PL lifetims (ns)

Temperature (k)	$CsPbBr_3$	$MAPbBr_3$	$FAPbBr_3$
4	1.077	48.97	1.524
20	2.709	17.16	4.072
40	3.333	23.96	2.665
60	2.309	28.33	2.437
80	2.299	19.47	2.433
100	2.597	11.04	3.065
120	3.564	10.09	3.584
140	4.459	8.65	4.214
170	6.079	10.05	5.271
200	7.872	14.02	7.492
230	10.066	22.07	8.764
250	11.799	35.78	12.016
300	21.153	77.9	15.313

Table 4.2. Tabular data from figure 4.4: Emission energy (eV)

Temperature (K)	$CsPbBr_3$	$MAPbBr_3$	$FAPbBr_3$
4	52.973	38.974	25.789
20	44.309	38.224	24.897
40	44.646	28.933	25.233
60	44.987	26.98	24.863
80	45.332	27.244	29.1672
100	50.154	29.29	33.519
120	55.03	31.244	37.778
140	59.732	36.446	42.054
170	64.702	43.72	50.467
200	69.729	47.743	54.977
230	79.338	56.851	64.147
260	79.338	66.096	69.323
300	93.529	79.773	78.876

Table 4.3: Tabular data from figure 2: Integrated PL intensity as a function of temperaturue.

Temperature (K)	$CsPbBr_3$	$MAPbBr_3$	$FAPbBr_3$
4	4.87E+03	1.13E+03	5.12E+07
20	5.15E+03	1.21E+03	5.55E+07
40	5.54E+03	1.33E+03	6.16E+07
60	5.63E+03	1.49E+03	6.49E+07
80	5.53E+03	1.67E+03	6.62E+07
100	5.54E+03	1.78E+03	6.67E+07
120	5.59E+03	1.75E+03	6.48E+07
140	5.56E+03	1.84E+03	6.28E+07
170	5.59E+03	1.77E+03	6.51E+07
200	5.15E+03	1.75E+03	6.61E+07
230	5.11E+03	1.74E+03	6.48E+07
260	5.11E+03	1.69E+03	6.16E+07
300	4.81E+03	1.35E+03	6.23E+07

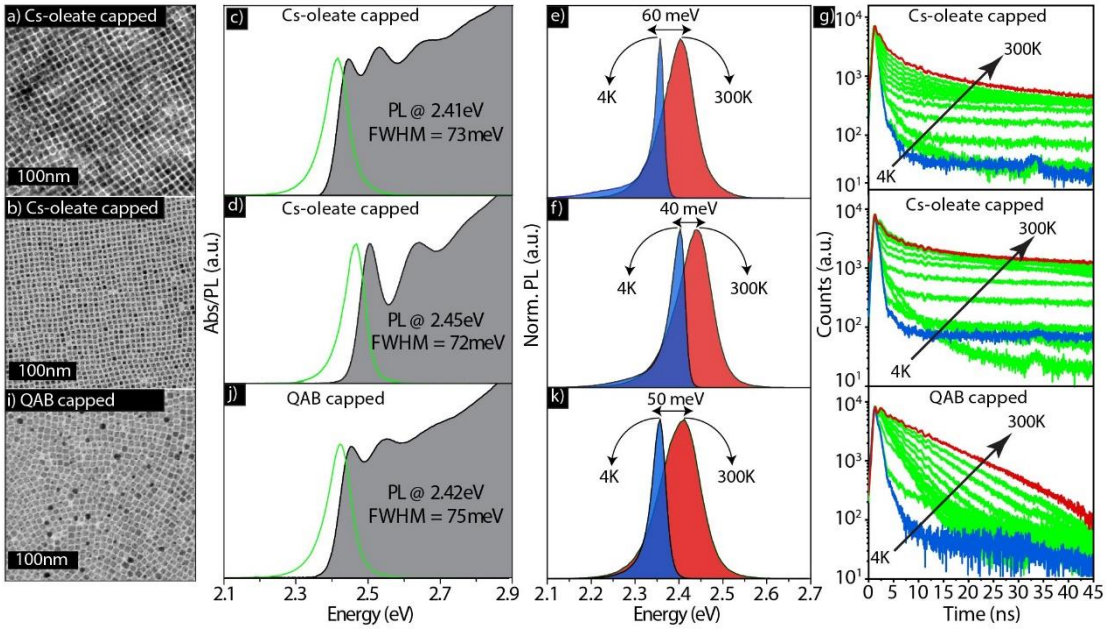

Figure 4. 5. $CsPbBr_3$ NCs of different sizes and surface coatings: TEM images of 9.5 nm (a) and 6.4 nm (b) Cs-oleate capped $CsPbBr_3$ NCs. Absorbance and PL spectra of corresponding samples (c), (d) and comparison of their PL spectra recorded from film of NCs at 4 K and 300 K (e, f). Normalized PL decay traces collected for different temperatures from 4 to 300 K for 9.5 nm and 6.4 nm NCs (g, h) respectively. TEM image of the $CsPbBr_3$ NCs after ligand exchange reaction with QAB (i), Absorbance and PL spectra of the QAB capped NCs in toluene dispersion (j), representative PL spectra of NCs films recorded at 4 K and 300 K (k) and normalized PL lifetimes collected from 4 to 300 K of corresponding sample (k).

UV-Vis absorption and PL spectra measured from the colloidal dispersion of the corresponding samples are reported in Figure 4.5 c, d. The size uniformity in both samples is corroborated by the appearance of distinctive excitonic features in their optical absorption spectra (grey shaded spectra). Both samples manifest a single emission peak with narrow PL linewidth in the range of 72-73 meV. The PL peak position depends on quantum confinement with a blue shifted emission for the smaller NC sample (PL at 2.45 eV) with respect to the larger one (PL at 2.41 eV). PL spectra recorded at RT and 4K manifest narrower and red-shifted PL at low temperature, where the red-shift is significantly smaller for the more quantum-confined sample. Ergo increased quantum confinement reduces the red shift observed for bulk $CsPbBr_3$, related to the temperature-dependent Pb 4d and Br 6s orbital overlap. The PL decay traces are depicted in Figure 4.5 g, h and show no NC size related difference. For both samples, a fast decay component develops and gains in weight with decreasing temperature, while the slower component deceases in weight in the cryogenic range.

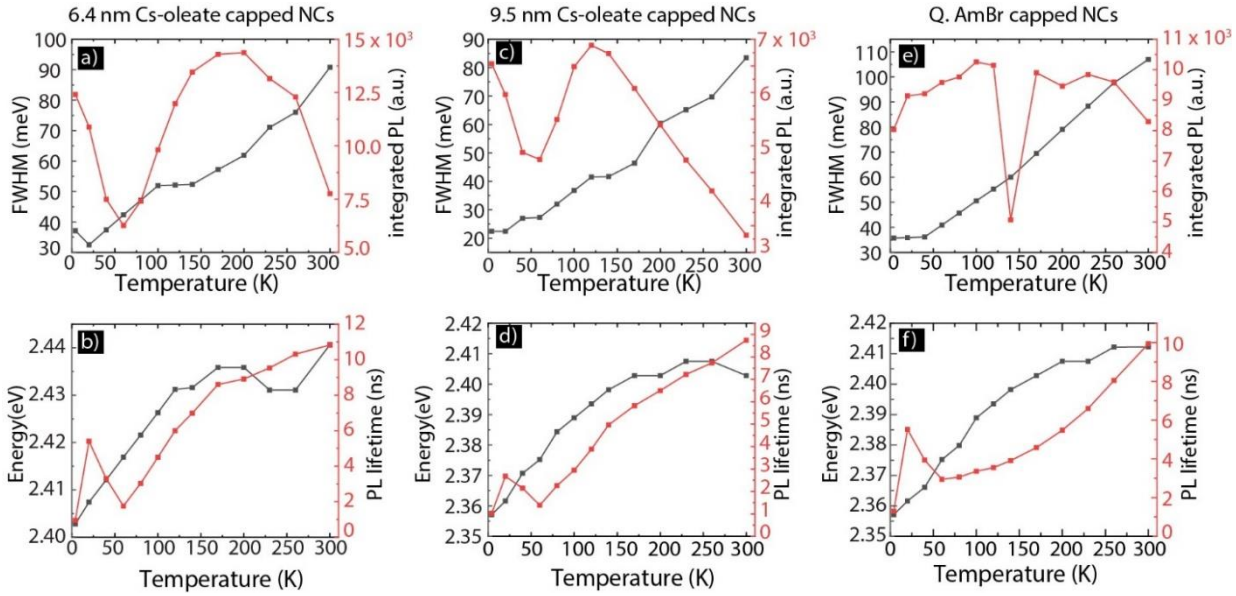

Figure 4. 6. Trends of integrated PL versus PL line width and peak energy versus PL lifetimes as function of temperature for 6.4 nm Cs-oleate capped $CsPbBr_3$ (a, b), 9.5 nm Cs-oleate capped $CsPbBr_3$ (c, d) and QAB capped $CsPbBr_3$ (e, f) respectively.

To gain deeper insight into the role of the ligands on the photophysics of the $CsPbBr_3$ nanocrystals we have performed a ligand exchange on the sample with smaller NC size fabricated by the synthesis described above, replacing the native Cs-oleate ligands with QAB.[25]

Table 4.5: Average PL decays (ns) for various surface coatings

Temperature (k)	6.4 nm Cs-oleate capped $CsPbBr_3$ NCs	9.5 nm Cs-oleate capped $CsPbBr_3$ NCs	8.7 nm QAB capped $CsPbBr_3$ NCs
4	0.953839	1.02015	1.30433
20	5.40789	2.67521	5.51761
40	3.30035	2.14701	3.93724
60	1.75659	1.38652	2.94028
80	3.03275	2.25995	3.05718
100	4.49604	2.94845	3.35461
120	5.99868	3.88457	3.54988
140	6.98913	4.96758	3.91353
170	8.60559	5.82402	4.58507
200	8.91125	6.49799	5.48095
230	9.53231	7.21614	6.59683
250	10.3136	7.73055	8.04693
300	10.8233	8.74142	9.94083

Table 4.6: Influence of surface chemistery on emission energy (eV) of $CsPbBr_3$ NCs.

Temperature (K)	Mixed ligands capped	Cs-oleate capped	QAB capped
4	2.3438	2.3571	2.3571
20	2.3482	2.3616	2.3616
40	2.3571	2.3707	2.3661
60	2.3661	2.37519	2.3752
80	2.3752	2.38433	2.3798
100	2.3798	2.38892	2.3889
120	2.3889	2.3935	2.3935
140	2.3935	2.39816	2.3982
170	2.3982	2.40281	2.4028
200	2.4075	2.4028	2.4075
230	2.4075	2.40747	2.40747
260	2.4122	2.40748	2.41216
300	2.4122	2.40281	2.4122

QAB ligands are proton-free and therefore much more stable with respect to RNH_3Br, resulting in NCs with near-unity PLQY without affecting the overall morphology and structural properties of the NCs, as demonstrated by the TEM image and photoluminescence and absorbance spectra in Figure 3i,j,k that are similar to those obtained from the Cs-oleate

counterparts. Interestingly, the PL decay traces are markedly different for the QAB passivated NCs, with an almost monoexponential decay that persists also for lower temperatures down to 170 K. These measurements give a strong indication that the PL decay dynamics (and therefore the PLQY) strongly depend on the surface passivation of the NC, while PL energy and line width are defined by the NC size and choice of the cation.

Table 4.7. PL line width (meV) as a funtion of temperature for various surface coatings

Temperature (K)	Mixed ligands capped	Cs-oleate capped	QAB capped
4	52.973	22.4	35.72
20	44.309	22.4	35.852
40	44.646	27	36.126
60	44.987	27.3	40.876
80	45.332	32	45.681
100	50.154	36.8	50.54
120	55.03	41.5	55.24
140	59.732	41.67	59.963
170	64.702	46.39	69.459
200	69.729	60.4	79.031
230	79.338	65.2	88.334
260	79.338	69.728	97.639
300	93.529	83.52	106.95

Figure 4.7 schematically illustrates the three different surface coatings that we employed in this work: mixed oleylamine and oleic acid ligands (primary amines) that attach at the Br atoms and Cs sites of the perovskite lattice, Cs-oleate ligands (secondary amines) that attach at the Br atoms and leave a CS rich surface, and QAB ligands (quaternary amines) that replace Cs at the surface. Cs-oleate capped NCs are characterized by halide deficiencies that are detrimental for the PLQY (<80%), whereas both mixed ligands and QAB capped NCs have PLQY that is higher than 90%.[22,25]

Table 4.8: PL lifetime as a funtion of temperature for various surface coatings (ns)

Temperature (K)	Mixed ligands capped	Cs-oleate capped	QAB capped
4	1.077	1.02015	1.30433
20	2.70899	2.67521	5.51761
40	3.33253	2.14701	3.93724
60	2.30931	1.38652	2.94028
80	2.29891	2.25995	3.05718
100	2.59723	2.94845	3.35461
120	3.56396	3.88457	3.54988
140	4.45977	4.96758	3.91353
170	6.07894	5.82402	4.58507
200	7.87174	6.49799	5.48095
230	10.0662	7.21614	6.59683
260	11.7987	7.73055	8.04693
300	21.1531	8.74142	9.94083

Table 4.9: Integrated PL intensity as a funtion of temperature for various surface coatings

Temperature (K)	Mixed ligands capped	Cs-oleate capped	QAB capped
4	4874.1	6541.6	8033.2
20	5154.1	5961.7	9139.4
40	5540.0	4875.6	9211.9
60	5634.6	4744.9	9583.5
80	5529.9	5494.8	9765.7
100	5537.2	6487.5	10256.0
120	5587.6	6886.4	10143.0
140	5557.6	6730.9	5064.2
170	5590.9	6078.3	9898.7
200	5145.4	5391.4	9461.2
230	5109.8	4732.4	9845.2
260	5110.8	4153.4	9597.2
300	4810.7	3323.9	8293.5

The PL spectra of the NCs, for different temperatures and with the different surface coatings are shown in Figure 4.7 b-d. For both mixed ligands and QAB the PL intensity first continuously increases and then, for temperature below 70 K, decreases with decreasing temperature, while the PL line width continuously becomes narrower. For the Cs oleate capped NCs there

is a notable dip in PL intensity at temperatures around 60K, and eventually the PL line width becomes very sharp at 4K with a very high PL intensity, manifesting a stretched exponential tail at its low energy shoulder.

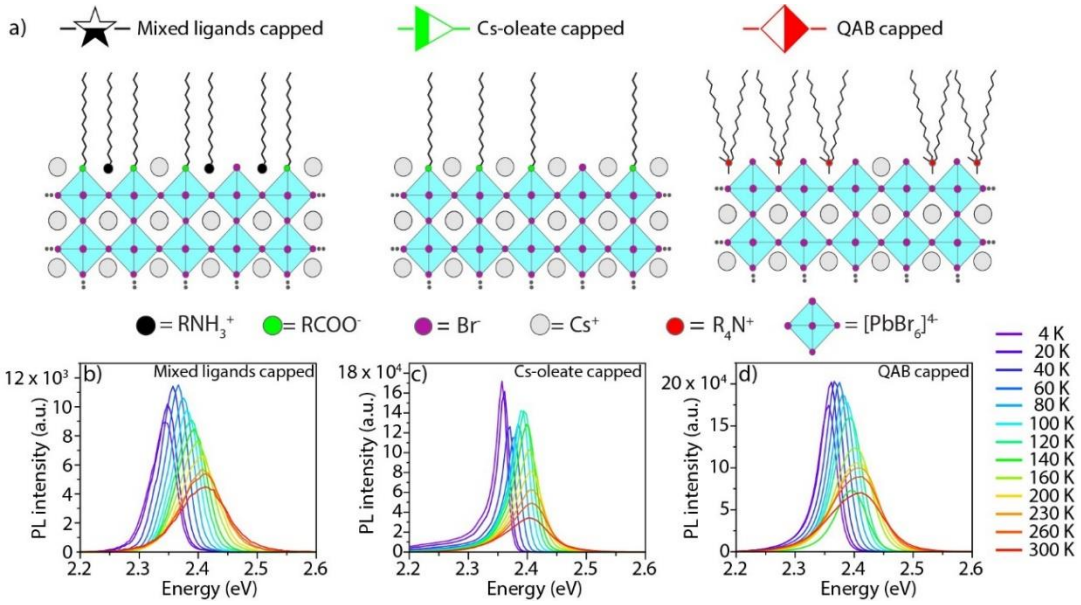

Figure 4. 7. (a) Schematic illustration of $CsPbBr_3$ NCs with different surface passivation. (b-d) PL spectra for different temperatures of the NCs films with the three different surface coatings.

From the decay dynamics of the samples with different ligands we draw the following picture: The monoexponential decay at room temperature for mixed ligands and QAB passivation points to a single radiative decay channel and negligible non-radiative decay, which is corroborated by the high PL intensity. With decreasing temperature PL intensity increases and the PL decay slope becomes steeper, indicating an increase of the radiative rate of that decay channel. With further decreasing temperature a faster decay component emerges and the PL decay becomes biexponential. This can be rationalized by slowing down the dynamic ligand binding on the NC surface which leads to less efficient passivation. This effect is balanced across an intermediate temperature range by the increasing rate of the radiative channel. At temperatures below 50K the non-radiative decay takes over and the PL intensity drops significantly. For Cs-oleate passivated NCs the PL decay is already biexponential at room temperature, which can be related to Br deficiencies that induce non-radiative decay. This correlates well with less efficient surface passivation of Cs-oleate leading to lower PLQY.

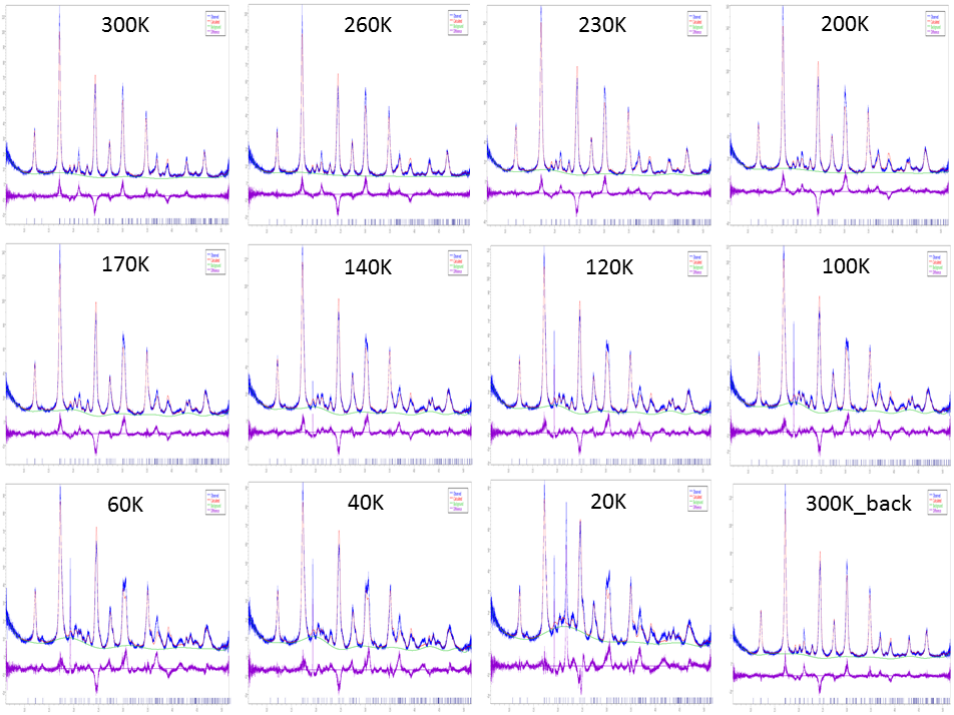

Figure 4. 8. XRD patterns collected at different temperature from 300 K to 20 K on and heating up the sample back to 300 K on drop casted film of $CsPbBr_3$ nanocrystals. The observed thermally induced expansion in the unit cell of $CsPbBr_3$ NCs was found to be reversible when the sample was heated back to 300 K.

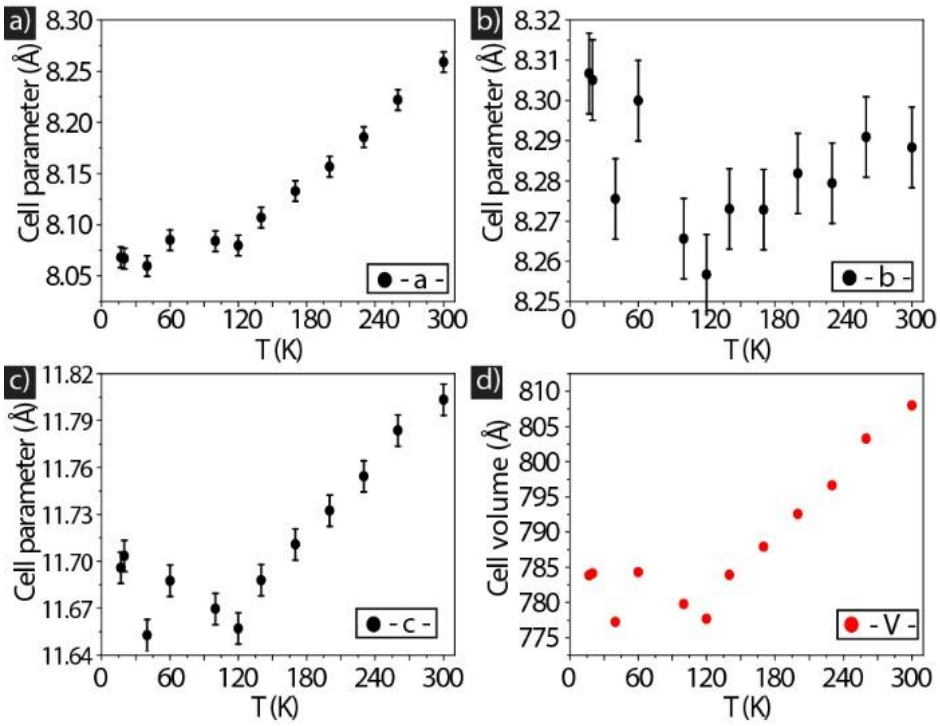

Figure 4. 9. Cell parameters (a,b,c) obtained from the temperature dependent XRD measurements of $CsPbBr_3$ nanocrystals. The data yields a thermally induced expansion of $CsPbBr_3$ NCs in the orthorhombic phase.

Table 4.10: Thermally induced variation in the cell parameters of mixed ligands capped $CsPbBr_3$ NCs

T (K)	a	b	c	Cell Volume
300	8.25906	8.28831	11.80331	807.98
260	8.22196	8.29093	11.78364	803.26
230	8.1856	8.27942	11.75434	796.62
200	8.1567	8.28185	11.73239	792.55
170	8.13283	8.28185	11.71081	787.92
140	8.10704	8.27305	11.68789	783.91
120	8.07976	8.2567	11.65699	777.66
100	8.08407	8.26566	11.66956	779.76
60	8.08502	8.29994	11.68757	784.3
40	8.05959	8.27552	11.65278	777.21
20	8.067	8.30508	11.70342	784.1
17	8.06812	8.3067	11.69584	783.85
300	8.25849	8.28184	11.80030	807.09

The electronic structure, and therefore also the optical properties, are strongly related to the structure of the nanocrystal lattice, and temperature dependent phase transitions from cubic to tetragonal to orthorhombic have been reported for lead halide perovskite films.[26-29]Wright, 2016 #28} In order to gain insight in the structural evolution with temperature, and in particular to test if temperature-induced phase transitions occur in our nanocrystal samples, we carried out temperature dependent X-ray diffraction (XRD) measurements of mixed ligands shell and Cs-oleate capped $CsPbBr_3$ NCs. The XRD data was collected at the XPD beamline of the Brazilian Synchrotron Light Laboratory (LNLS), in the temperature range from 300 K down to 20 K using a He closed cycle cryostat. Measurements were performed at 10 keV energy (λ=1.23984 Å) in the Bragg-Brentano geometry using a 1D Mythen detector. The instrumental function has been determined from a NIST Al_2O_3 standard. Figure 4.8 shows the experimental patterns and relative Rietveld fits in the entire temperature range. The acquired data was indexed according to the diffraction pattern of the $CsPbBr_3$ orthorhombic phase (ICSD code #97851), projected along the a, b and c axis (Figure 4.8 and 4.9). No phase transformation was registered in the entire temperature range, in agreement with reports on $CsPbX_3$ and $MaPbI_3$ NCs.[13,15] Upon cooling down the NCs films, Rietveld data analysis revealed a decrease of the a and c parameters, and of the unit cell, while the cell parameter "b" was less influenced by temperature independent of the type of surface passivation. Note that a and b have almost the same value for this crystal structure, therefore our analysis attributes

most of the variation to one of the two parameters, in this case a. The relevant information resides in the volume of the unit cell that decreases with temperature. These changes in the unit cell were reversible when NCs film was heated back to 300 K. We also observed the appearance of additional sharp peaks from 140K down to 20K, which disappeared when the NCs film is heated back to 300K (See Figure 4.8). We attribute these peaks to the formation of a thin ice layer at the sample surface after few hours of measurements at a pressure of at 10^{-6} mbar, or to the frozen organics. Since no phase transition has been observed, only a smooth decrease in cell parameters and volume cell, the widely reported size dependent multiple peak emission spectra at low temperature [12,14,15,30] are most likely due to the size in homogeneities of the starting NCs samples.

4.4 Conclusion

In conclusion, our study on the photophysics of lead bromide perovskite nanocrystal films demonstrated that their low temperature emission is defined by a single photoluminescence peak, and that no temperature-induced phase transitions occur in these materials in the investigated temperature range. Therefore, the possible observation of multiple emission peaks at low temperature[18, 21, 31-33] should originate from different NC populations within the same sample. The PL peak energy, and its temperature induced shift is strongly related to the NC size, while the PL intensity and the recombination dynamics of the photoexcited carriers depend mostly on the surface functionalization. QAB ligands lead to improved PL stability and monoexponential PL decay over a larger temperature range among the three investigated surface passivations. The drop in PL intensity from 250K towards room temperature shows that surface passivation of lead bromide perovskite nanocrystals needs still to be improved towards a more stable ligand binding in the range exceeding room temperature. This is particularly important for the application of such materials in optoelectronic devices.

4.5. References

1 Boles, M. A., Ling, D., Hyeon, T. & Talapin, D. V. The surface science of nanocrystals. *Nature materials* **15**, 141 (2016).

2 Chen, O. *et al.* Surface-functionalization-dependent optical properties of II–VI semiconductor nanocrystals. *Journal of the American Chemical Society* **133**, 17504-17512 (2011).

3 Talapin, D. V., Lee, J.-S., Kovalenko, M. V. & Shevchenko, E. V. Prospects of colloidal nanocrystals for electronic and optoelectronic applications. *Chemical reviews* **110**, 389-458 (2009).

4 Shamsi, J., Urban, A. S., Imran, M., De Trizio, L. & Manna, L. Metal Halide Perovskite Nanocrystals: Synthesis, Post-Synthesis Modifications, and Their Optical Properties. *Chemical reviews* **119**, 3296-3348 (2019).

5 Protesescu, L. *et al.* Nanocrystals of cesium lead halide perovskites (CsPbX3, X= Cl, Br, and I): novel optoelectronic materials showing bright emission with wide color gamut. *Nano letters* **15**, 3692-3696 (2015).

6 Schmidt, L. C. *et al.* Nontemplate synthesis of CH3NH3PbBr3 perovskite nanoparticles. *Journal of the American Chemical Society* **136**, 850-853 (2014).

7 Sutherland, B. R. & Sargent, E. H. Perovskite photonic sources. *Nature Photonics* **10**, 295 (2016).

8 Kovalenko, M. V., Protesescu, L. & Bodnarchuk, M. I. Properties and potential optoelectronic applications of lead halide perovskite nanocrystals. *Science* **358**, 745-750 (2017).

9 Quan, L. N. *et al.* Perovskites for Next-Generation Optical Sources. *Chemical reviews* **119**, 7444-7477 (2019).

10 Jing, P. *et al.* Temperature-dependent photoluminescence of CdSe-core CdS/CdZnS/ZnS-multishell quantum dots. *The Journal of Physical Chemistry C* **113**, 13545-13550 (2009).

11 Zhao, Y. *et al.* High-temperature luminescence quenching of colloidal quantum dots. *ACS nano* **6**, 9058-9067 (2012).

12 Li, J. *et al.* Temperature-dependent photoluminescence of inorganic perovskite nanocrystal films. *Rsc Advances* **6**, 78311-78316 (2016).

13 Diroll, B. T., Nedelcu, G., Kovalenko, M. V. & Schaller, R. D. High-Temperature Photoluminescence of CsPbX3 (X= Cl, Br, I) Nanocrystals. *Advanced Functional Materials* **27**, 1606750 (2017).

14 Ramade, J. *et al.* Fine structure of excitons and electron–hole exchange energy in polymorphic CsPbBr3 single nanocrystals. *Nanoscale* **10**, 6393-6401, doi:10.1039/C7NR09334A (2018).

15 Diroll, B. T., Guo, P. & Schaller, R. D. Unique Optical Properties of Methylammonium Lead Iodide Nanocrystals Below the Bulk Tetragonal-Orthorhombic Phase Transition. *Nano Letters* **18**, 846-852, doi:10.1021/acs.nanolett.7b04099 (2018).

16 De Roo, J. *et al.* Highly dynamic ligand binding and light absorption coefficient of cesium lead bromide perovskite nanocrystals. *ACS nano* **10**, 2071-2081 (2016).

17 Smock, S. R., Williams, T. J. & Brutchey, R. L. Quantifying the Thermodynamics of Ligand Binding to CsPbBr3 Quantum Dots. *Angewandte Chemie* **130**, 11885-11889 (2018).

18 Ravi, V. K. *et al.* Origin of the substitution mechanism for the binding of organic ligands on the surface of CsPbBr3 perovskite nanocubes. *The journal of physical chemistry letters* **8**, 4988-4994 (2017).

19 Pan, A. *et al.* Insight into the ligand-mediated synthesis of colloidal CsPbBr3 perovskite nanocrystals: the role of organic acid, base, and cesium precursors. *ACS nano* **10**, 7943-7954 (2016).

20 Koscher, B. A., Swabeck, J. K., Bronstein, N. D. & Alivisatos, A. P. Essentially trap-free CsPbBr3 colloidal nanocrystals by postsynthetic thiocyanate surface treatment. *Journal of the American Chemical Society* **139**, 6566-6569 (2017).

21 Wheeler, L. M. *et al.* Targeted Ligand-Exchange Chemistry on Cesium Lead Halide Perovskite Quantum Dots for High-Efficiency Photovoltaics. *Journal of the American Chemical Society* **140**, 10504-10513 (2018).

22 Imran, M. *et al.* Benzoyl halides as alternative precursors for the colloidal synthesis of lead-based halide perovskite nanocrystals. *Journal of the American Chemical Society* **140**, 2656-2664 (2018).

23 Zhang, F. *et al.* Brightly luminescent and color-tunable colloidal CH3NH3PbX3 (X= Br, I, Cl) quantum dots: potential alternatives for display technology. *ACS nano* **9**, 4533-4542 (2015).

24 Li, X. *et al.* CsPbX3 quantum dots for lighting and displays: room-temperature synthesis, photoluminescence superiorities, underlying origins and white light-emitting diodes. *Advanced Functional Materials* **26**, 2435-2445 (2016).

25 Imran, M. *et al.* Simultaneous Cationic and Anionic Ligand Exchange For Colloidally Stable CsPbBr3 Nanocrystals. *ACS Energy Letters* **4**, 819-824 (2019).

26 Guo, Y. *et al.* Interplay between organic cations and inorganic framework and incommensurability in hybrid lead-halide perovskite ${\mathrm{CH}}_{3}{\mathrm{NH}}_{3}{\mathrm{PbBr}}_{3}$. *Physical Review Materials* **1**, 042401, doi:10.1103/PhysRevMaterials.1.042401 (2017).

27 Chen, T. *et al.* Origin of long lifetime of band-edge charge carriers in organic–inorganic lead iodide perovskites. *Proceedings of the National Academy of Sciences* **114**, 7519, doi:10.1073/pnas.1704421114 (2017).

28 Wu, K. *et al.* Temperature-dependent excitonic photoluminescence of hybrid organometal halide perovskite films. *Physical Chemistry Chemical Physics* **16**, 22476-22481, doi:10.1039/C4CP03573A (2014).

29 Fang, H.-H. *et al.* Photoexcitation dynamics in solution-processed formamidinium lead iodide perovskite thin films for solar cell applications. *Light: Science & Applications* **5**, e16056-e16056, doi:10.1038/lsa.2016.56 (2016).

30 Lee, S. M. *et al.* Temperature-Dependent Photoluminescence of Cesium Lead Halide Perovskite Quantum Dots: Splitting of the Photoluminescence Peaks of CsPbBr3 and CsPb(Br/I)3 Quantum Dots at Low Temperature. *The Journal of Physical Chemistry C* **121**, 26054-26062, doi:10.1021/acs.jpcc.7b06301 (2017).

Chapter 5.

5.1. Conclusions

This dissertation encompasses two main projects, each of them achieving the proposed target.

The specific scientific findings of all these projects can be summarized as follows:

- CdSe NPLs are the center of many studies owing to the control of their synthesis, relationship between shape and exciton dynamics as well as the narrow and homogeneously broadened emission linewidth. These properties can be further tuned by coating them with another semiconductor such as core/shell, or extended ternary heretostructure for instance CdSe/CdS/CdTe nanoplatelets. Due to the staggered band offset between CdSe and CdTe, we observed emission from an indirect transition around 650 nm. As CdS forms a barrier for hole relaxation between crown and core regions, the CdSe/CdS/CdTe yielded an additional emission peak from the CdSe core, in contrast with CdSe/CdTe core/crown nanoplatelets without a barrier. The resulting dual emission was investigated as a function of temperature. The different nature of both emission peaks (direct in CdSe vs. indirect across the CdSe/CdTe interface) yielded a spectrally and temporally stable indirect transition as a function of temperature, while the emission rate of the CdSe emission increased at lower temperatures, and the spectral position shifted to shorter wavelengths. We further observed that CdSe/CdS/CdTe ternary NPLs exhibit nearly temperature-independent PL decays contrary to the CdSe/CdS NPLs.
- The second generation of material studied here i.e “lead halide perovskite” NCs is one of the most investigated semiconductor material in the last years due to their ease of preparation, broadly tunable band gap, near unity fluorescence quantum efficiency and excellent color purity. We carried out a comprehensive study of size, composition and surface functionalization dependent optical properties of lead halide perovskite NCs. Contrary to most of the previous findings, we observe a single, narrow emission peak at low temperature for NCs with various sizes, compositions and surface coatings. Temperature-dependent photoluminescence (PL) and PL-lifetime data for different compositions ($APbBr_3$, A=Cs, MA, FA) reveal that MA-based NCs were the

most sensitive to temperature variations with least preservation of PL, featuring the highest thermal broadening of PL and longest lifetimes, whereas FA based NCs were the most resilient. Furthermore, a comparison of the photophysical properties of NCs having different surface coatings shows that their optical properties are strongly influenced by surface chemistry, with quaternary bromide capped NCs being the most stable samples at elevated temperature, as they retained the highest PL intensity. Considering all these results together, we provide unequivocal evidence that lead halide perovskite NCs exhibit no inhomogeneity in their PL and additionally their optical properties are strongly surface functionalization dependent. our study on the photophysics of $APbBr_3$ nanocrystal films demonstrated that their low temperature emission is defined by a single photoluminescence peak, and that no temperature-induced phase transitions occur in these materials in the investigated temperature range. Therefore, the possible observation of multiple emission peaks at low temperature extensively reported for LHP should originate from different NC populations within the same sample. The PL peak energy, and its temperature induced shift is strongly related to the NC size, while the PL intensity and the recombination dynamics of the photoexcited carriers depend mostly on the surface functionalization. Here QAB ligands lead to improved PL stability over a larger temperature range. Our study that combines a temperature-dependent optical study of $APBr_3$ NCs with different surface functionalization with a structural investigation by XRD demonstrates that there is no intrinsic multipeak emission of NC films with homogeneous size distribution at low temperature. Fundamental insight on band-edge recombination, important for development of perovskite nanocrystal materials as light sources.

5.2. List of publication

Most recent first,

- **Ijaz. P.** et al. Ultrafast laser spectroscopy of CdSe/CdS/CdTe core/crown nanoplatelets (in preparation).
- **Ijaz, P**. Imran M, Soares MM, Tolentino HC, Martín-García B, Giannini C, Moreels I, Manna L, Krahne R. Composition, Size, and Surface Functionalization Dependent Optical Properties of Lead Bromide Perovskite Nanocrystals**. *J. Phys. Chem. Lett.* 2020**, 11, XXX, 2079-2085.
- Imran M, **Ijaz P**, Goldoni L, Maggioni D, Petralanda U, Prato M, Almeida G, Infante I, Manna L. Simultaneous Cationic and Anionic Ligand Exchange For Colloidally Stable CsPbBr3 Nanocrystals. **ACS Energy Letters**. **2019**, 4; 4(4):819-24.
- Imran M, **Ijaz P**, Baranov D, Goldoni L, Petralanda U, Akkerman Q, Abdelhady AL, Prato M, Bianchini P, Infante I, Manna L. Shape-Pure, Nearly Monodispersed CsPbBr3 Nanocubes Prepared Using Secondary Aliphatic Amines. **Nano letters**. **2018**, 1; 18(12):7822-31.
- Shamsi J, Dang Z, **Ijaz P**, Abdelhady AL, Bertoni G, Moreels I, Manna L. Colloidal CsX (X= Cl, Br, I) nanocrystals and their transformation to CsPbX3 nanocrystals by cation exchange. **Chemistry of Materials**. **2017**, 19; 30(1):79-83.

5.4. Abbreviations

Full name	Abbreviation
Core Barrier	CB
Core Crown	CC
Core Barrier Crown	CBC
Two dimensional	2D
Conduction band	CB
Quantum Well	QW
Boltzmann constant	K_B
Density functional theory	DFT
Dihexylamine	DHAm
Dioctylamine	DOAm
Didecylamine	DDAm
Didodecylamine	DDDAm
Dioctadecylamine	DODAm
Dimethylsulfoxide	DMSO

Energy-disperse X-Ray spectroscopy	EDX
Electron energy loss spectroscopy	EELS
Full width at half maximum	FWHM
High-angle annular dark -field	HAADF
Transmission electron microscopy	TEM
Lead halide perovskite	LHP
Nanocubes	NCs
Nanoplatelets	NPLs
Oleic acid	OA
Octadecene	ODE
Oleylamine	OLAm
Photoluminescence	PL
Photoluminescence quantum yield	PLQY
Quantum dots	QDs
Transmission electron microscopy	TEM
X-ray diffraction	XRD

X-ray Photoelectron Spectroscopy	XPS
heteronanocrystal(s)	hNC(s)
Quantum dot(s)	QD(s)
Conduction band	CB
density of states	DOS
Magnitude of the electron charge	e
Bulk semiconductor band gap	E_g
Exciton energy	Eexc
Full width Half Maximum	FWHM
Time-Correlated Single Photon Counting	TCSPC